Postgraduate Studies Programme in Physics

Department of Physics

School of Sciences

University of Ioannina

Master's Thesis (M.T):

Tomographic reconstruction of three-dimensional photoelectron momentum distributions from their two-dimensional projections on a position sensitive detector

Konstantinos Filippou
817

Supervisor: Samuel Cohen

Ioannina
2024

Acknowledgments

I would like to thank my advisor, Samuel Cohen, for his years of continued support, guidance and patience. His mentorship has brought this work to fruition and introduced me to the significance and process of scientific research. Looking back, I cannot imagine a more suitable person to have worked with.

I would like to further thank the other members of the committee, Emmanuel Benis and Sotirios Danakas, for their valuable time and input into this work. Without their participation this work could never reach the final polished form. I would, particularly, like to thank Sotirios Danakas for his collaboration and assistance in developing the tomography algorithm used in this work.

I am forever grateful to my friends and family whose unwavering support and encouragement have brought me to where I am today.

Contents

page

Abstract

Tomographic reconstruction of three-dimensional (3D) objects via their rotation with respect to a given axis and their subsequent projection on a given two-dimensional (2D) surface is nowadays employed in a quite broad spectrum of applications, including medicine and science. It is presently more and more frequently implicated in the study of atomic and molecular photoionization and in conjunction with velocity map imaging (VMI) spectrometers. The latter provides projections of the 3D momentum distribution of the produced photoelectrons (or other charged particles) on a 2D position sensitive detector whose surface is perpendicular to the spectrometer axis. The recovery of the full 3D distribution is achieved via the rotation of this object with respect to an axis parallel to the detector surface, and the recording of the resulting projections. The only other alternative technique involves the, so-called, inverse Abel transform of a single projection, when the polarization of the ionizing radiation is linear and perpendicular to the spectrometer axis. Thus, inverse Abel transform cannot be employed with any other geometry and/or light polarization, a fact which is, of course, quite restrictive.

Therefore, Tomography becomes a necessity when complex light-atom or -molecule interactions come into play and such experiments are frequently performed in our Atomic & Molecular Physics laboratory. In the present work a computational environment is developed, where the user provides the object projections (each at a different angle of rotation) and the developed code delivers the tomographic reconstruction of this object. The code benefits as much as possible from build-in tomographic capabilities incorporated in the programming language. At this stage of testing, the theoretical photoelectron angular distribution corresponding to two-photon ionization of hydrogen atom is employed as the object and an auxiliary program computes its projections to the detector. For linear light polarization, tomographic reconstruction is compared with inverse Abel transform and it is found to be much more accurate. It is also verified that tomographic reconstruction works equally well when circular or elliptical light polarization is employed. Finally, for any polarization, Tomography is proved to be highly robust, even when noise up to 5% of the maximum signal level is added to the projections before reconstruction.

Περίληψη

Η τομογραφική ανακατασκευή τρισδιάστατων (3D) αντικειμένων μέσω της περιστροφής τους γύρω από έναν δοσμένο άξονα και η επακόλουθη προβολή τους πάνω σε μία δοσμένη δισδιάστατη (2D) επιφάνεια, αξιοποιείται στις μέρες σε ένα αρκετά ευρύ φάσμα εφαρμογών, συμπεριλαμβανομένου της Ιατρικής και της Φυσικής. Επί του παρόντος, χρησιμοποιείται όλο και πιο συχνά στην μελέτη του φωτοϊονισμού ατόμων και μορίων, σε συνδυασμό με τα φασματόμετρα απεικόνισης ταχυτήτων (VMI). Τα φασματόμετρα αυτά παρέχουν προβολές των τρισδιάστατων κατανομών ορμής των παραγόμενων φωτοηλεκτρονίων (ή άλλων φορτισμένων σωματιδίων) πάνω σε ένα δισδιάστατο (2D) ανιχνευτή θέσεων, του οποίου η επιφάνεια είναι κάθετη στον άξονα του φασματόμετρου. Η ανάκτηση της πλήρους τρισδιάστατης κατανομής επιτυγχάνεται μέσω της περιστροφής του αντικειμένου γύρω από έναν άξονα παράλληλο στην επιφάνεια του ανιχνευτή και της καταγραφής των προβολών που προκύπτουν. Η μόνη εναλλακτική τεχνική περιλαμβάνει τον λεγόμενο αντίστροφο μετασχηματισμό Abel μιας μεμονωμένης προβολής, με τη προϋπόθεση ότι η πόλωση της ιονίζουσας ακτινοβολίας είναι γραμμική και κάθετη στον άξονα του φασματόμετρου. Επομένως, ο αντίστροφος μετασχηματισμός Abel δεν μπορεί να χρησιμοποιηθεί σε οποιαδήποτε άλλη γεωμετρία ή/και πόλωση φωτός, γεγονός που τον καθιστά, εύλογα, αρκετά περιοριστικό.

Συνεπώς, η Τομογραφία καθίσταται αναγκαία όταν εμπλέκονται περίπλοκες αλληλεπιδράσεις φωτός-ατόμου ή φωτός-μορίου. Τέτοια πειράματα ,συχνά, πραγματοποιούνται στο εργαστήριο μας της Ατομικής και Μοριακής Φυσικής. Στην παρούσα εργασία αναπτύσσεται ένα υπολογιστικό περιβάλλον, όπου ο χρήστης παρέχει τις προβολές του αντικειμένου (που η καθεμία αντιστοιχεί σε διαφορετική γωνία περιστροφής) και ο κώδικας που συντάχθηκε δημιουργεί την τομογραφική ανακατασκευή του αντικειμένου. Ο κώδικας αξιοποιεί στο έπακρο τις ενσωματωμένες τομογραφικές δυνατότητες που περιλαμβάνονται στη γλώσσα προγραμματισμού. Σε αυτό το στάδιο της ανάπτυξης, η θεωρητική γωνιακή κατανομή φωτοηλεκτρονίων, που αντιστοιχεί σε διφωτονικό ιονισμό του ατόμου Υδρογόνου, χρησιμοποιείται ως το αντικείμενο και ένα βοηθητικό πρόγραμμα υπολογίζει τις προβολές του στον ανιχνευτή. Για τη γραμμική πόλωση φωτός, η τομογραφική ανακατασκευή συγκρίνεται με τον αντίστροφο μετασχηματισμό Abel και προκύπτει ότι είναι ακριβέστερη αυτού. Επιβεβαιώνεται, επίσης, ότι η τομογραφική ανακατασκευή λειτουργεί εξίσου καλά όταν χρησιμοποιείται κυκλική ή ελλειπτική πόλωση φωτός. Τέλος, για όλα τα είδη πολώσεων, η Τομογραφία αποδεικνύεται αρκετά αποτελεσματική, ακόμα και όταν θόρυβος μέχρι και 5% της μέγιστης τιμής σήματος προστίθεται στις προβολές πριν από την ανακατασκευή.

1.Introduction

Tomography is a method that allows for the reconstruction of an object through a series of projections resulting in the study of its structure. The theoretical foundation of tomography dates back to Radon, a mathematician who derived a method in 1917 to project a 2D object along parallel rays [1]. This method now is referred to as the Radon Transform [2] and will be discussed thoroughly in the next Section.

Tomography is a technique that has found wide applicability in various fields of medical and natural sciences. In medical science it is preferred for its non-invasive approach aiding in diagnosis and treatment. For example, it is applied to medical X-ray imaging [3], namely Computed Tomography scan (CT scan) and Magnetic Resonance Imaging (MRI) and was recognized with the Nobel Prize in Medicine in 1979.

The versatility of tomography is demonstrated by its use not only to the macrocosm of human bodies but also to the microcosm of matter consisting of atoms and molecules.

A direct approach to investigate matter is to access its electronic structure by interacting with light, with a process called photoionization [4]. In photoionization, matter absorbs a photon, thereby creating a free electron, photoelectron, and a charged ion. The determination of both momentum and angular distribution of electrons emitted in photoionization processes [5,6] is called photoelectron imaging and constitutes an important part of experimental Atomic and Molecular and Optical Physics (AMO). The basic idea behind the imaging method relies on projecting the produced charged particles onto a planar detector using an external electric field [7]. When the laser light is linearly polarized it produces a cylindrically symmetric distribution around the polarization axis. If, on the other hand, the light has circular polarization a distribution with cylindrical symmetry appears around the laser propagation axis. In both scenarios, a position-sensitive detector placed parallel to the previous axes can capture an image of the charged particle impacts. A widely employed detection scheme of the three-dimensional electron momentum distribution is the Velocity Map Imaging (VMI), which uses electrostatic fields to guide the electrons to the detector [8 9]. A 4π collection angle is obtained by an electrostatic lens with fields of several kV in strength, mapping the initial photoelectron momentum distribution (PMD) onto the detector. However, in a VMI the information perpendicular to the detector is lost [9].

Previous approaches in VMI experiments to derive the 3D (cylindrically symmetric) momentum distribution used inverse Abel transforms [10,11,12,13]. This allows to transform the 2D projection image on the detector into the 3D electron momentum distribution. This technique, however, suffers from major limitations. By construction, the Inverse Abel transform is limited to

distributions with cylindrical symmetry produced by linearly polarized light with the polarization axis parallel to the detector plane. In a more general case where this requirement is not met or more complex polarization is used, such as elliptically polarized light, Abel inversion does not apply. This requires a more elaborate analysis, the Tomographic method [14,15,16,17].

Tomography requires the rotation of the 3D distribution by the propagation axis with a 2D projection taken on each angle. These 2D projections can then be converted into images called sinograms. A sinogram contains all the information sufficient to reconstruct the initial image. Parallel ray tomography [2] which is used in our work is applied separately on each cross section of the 3D distribution. This means that 2D projections are taken along parallel lines dividing the 3D distribution into separate slices each representing a cross section of the 3D structure. From these projections, sinograms for each slice are obtained, and from them, the corresponding cross sections of the distribution can be reconstructed by applying the Backprojection method. The stacking of the reconstructed cross sections produces the tomographically reconstructed 3D distribution.

The columns of a sinogram correspond to different 2D projection angles with values representing the projected 2D slice after rotation. The values in each column correspond to a set of parallel lines crossing through the 2D slice at an angle matching the column's rotation angle. Extending the value distribution of a column along these lines backwards onto a blank image at the respective angle fills the image with the column's values. Repeating this process for all columns in the sinogram creates an image of cross sections composed of parallel lines at different angles. The result is the recreation of the initial 2D slice of the 3D object [18]. However, this method often yields blurry images. The blurriness occurs because Backprojection assumes that every point in a projection contributes equally to all points along the backprojection path. Due to the overlapping of projection lines especially at the center leads to an accumulation of intensity and as a result the fine details and edges of the object are blurred. To overcome these issues an improved method is utilized the Filtered Backprojection method [2]. In this method, each column is backprojected after being multiplied with a weight function which essentially amplifies the high frequency components of the image, which contain fine details and sharp edges, and reduce the contribution of lower frequency components, broad, smooth features of the image. The weight function is called filter, and some examples are the Ram-Lak (ramp) filter, Hann and Hamming filter which will be shown in the next Section.

First, Wollenhaupt et al [16] employed tomography in conjunction with a VMI spectrometer to recreate, using Fourier transforms, the three-dimensional photoelectron angular distribution (PAD) [16,56] produced through resonantly enhanced multiphoton photoionization of potassium. Then Smeenk et al [9] used tomography with Filtered Backprojection to obtain the distribution of photoelectrons produced through tunnel ionization of argon. Their work allowed the study of strong field phenomena with non-linearly polarized light [5,19, 20, 21].

In this work, the objective was to develop an algorithm in the Mathematica environment that employed the tomographic method and compare it with the existing program that utilizes the Abel inversion method: Polar Onion Peeling (POP) [22,58]. Specifically, the 3D PAD that was tested was produced by the theoretical calculation of a two-photon ionization of a hydrogen atom. Two scenarios were considered, the generation of a symmetric and a non-symmetric distribution. In the first scenario, a general symmetric PAD is produced from photoelectrons at only one energy group of $\omega \approx 9eV$ where an anti-resonance in the s-wave leaves only the d-wave to contribute. PADs were generated for both linear and elliptical polarization, with the linear case specifically used to compare the tomography program to the POP program. In the second scenario, only elliptical polarization was used on a PAD where both the s-wave and the d-wave contributed, with the addition of an extra state corresponding to electric quadrupole transition. This distribution does not represent a realistic physical process and was included to test the tomography program on a non-symmetric distribution. In both scenarios the program was tested with and without background noise added to the data.

The thesis is organized into three chapters. Chapter 1 provides the theoretical framework of Tomography, the Radon transform, and the reconstruction process through the Filtered Back projection method. Chapter 2 presents the results and discusses the assessment of tomographic and POP (where applicable) methods in reconstructing 3D PADs generated by linear and elliptical polarization for symmetric distributions, as well as elliptical polarization for non-symmetric distributions. For all the distributions two cases were considered: with and without the presence of background noise. Lastly, Chapter 3 presents the conclusions of this work and suggests possible directions for future improvements.

2. Theoretical Background

This section provides a thorough exposition of the principles of tomographic image reconstruction. Tomography is one of the available methods in creating a 2D representation of an object's cross section and it is widely used in different disciplines of Science and Technology such as Physics Medicine Engineering and Archaeology. The purpose of this section is to first demonstrate how a 2D object can be reconstructed using projections at different angles. Specifically, we will explore the mathematical basis of tomography focusing on function transforms and an essential theorem, the Fourier Slice theorem. A method of assessing the reconstructed image will be provided along with a way to optimize the result. The theory will then be extended to 3D objects and their reconstruction, forming the foundation for the analysis in the following sections where the tomographic reconstruction of 3D objects is required.

2.1. Radon Transform

The normal form of a 2D straight line in Cartesian coordinates is given by the equation [18]:

$$\rho = x\cos(\theta) + y\sin(\theta) \tag{2.1}$$

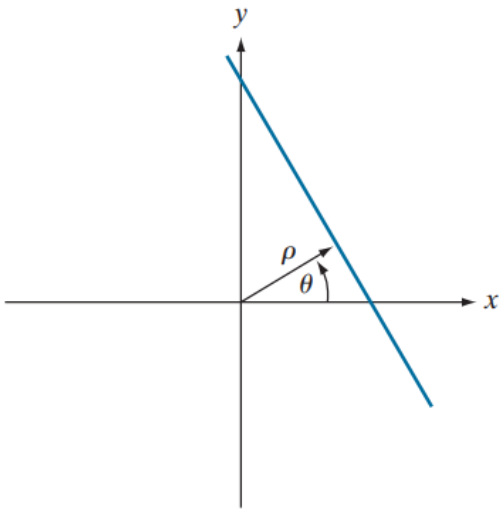

Figure 2.1. Normal form of a 2D straight line, taken from [18].

In Figure 2.1, θ is the angle subtended between the horizontal axis and the vertical line perpendicular to the blue line and ρ is the length of the vertical line. The above expression is central to the line integrals involved in what is known as the Radon transform [2,23,24]. In the coordinate system shown

in Figure 2.2, we have a 2D object defined by the function $f(x,y)$ and a set of parallel lines intersecting it.

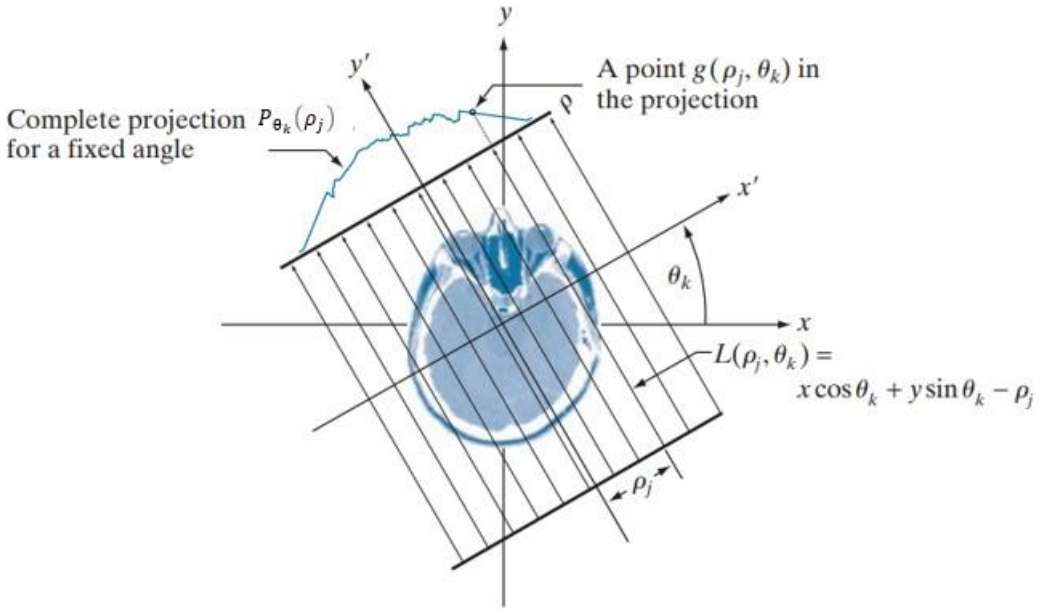

Figure 2.2. Line integrals along parallel lines, taken from [18] and modified.

These equidistant lines have the same inclination angle θ_k and different normal distances from the origin ρ_j. Then the Equation 2.1 of a line set to these parameters will be $L(\rho_j, \theta_k) = x\cos\theta_k + y\sin\theta_k - \rho_j$. Along each line-path described by that equation we calculate the integral P_{θ_k}, [18]

$$P_{\theta_k}(\rho_j) = \int_{(\theta_k, \rho_j)} f(x,y)ds \tag{2.2}$$

, where *s* is a variable along the line over which the integral is calculated. By using a delta function the previous line integral expression becomes,

$$P_{\theta_k}(\rho_j) = \int_{-\infty}^{+\infty} \int_{-\infty}^{+\infty} f(x,y)\delta(x\cos\theta_k + y\sin\theta_k - \rho_j)dxdy \tag{2.3}$$

As mentioned before, from the definition of delta function [2525] the line integral (Equation 2.3) is calculated only along the line $L(\rho_j, \theta_k)$,since the right side of the Equation 2.3 is set to zero unless the argument of the delta function is zero. If we consider all values of ρ_j for an arbitrary angle θ, the preceding equation generalizes to

$$P_\theta(\rho) = \int_{-\infty}^{+\infty} \int_{-\infty}^{+\infty} f(x,y)\delta(x\cos\theta + y\sin\theta - \rho)dxdy \tag{2.4}$$

The line integral $P_\theta(\rho)$ is known as Radon transform, [2,18 ,26], of the function $f(x,y)$. An example of the Radon transform of a circle for an angle θ is shown in Figure 2.3.

A projection is formed by combining a set of line integrals, in our case parallel to each other, as is given by $P_{\theta_k}(\rho_j)$, Equation 2.3, for a constant θ_k. This is known as parallel projection [2,18,27]. In Figure 2.2, parallel projection is demonstrated by the parallel lines going through the object resulting in a new function, the blue line, which is the projection of the object. Each individual

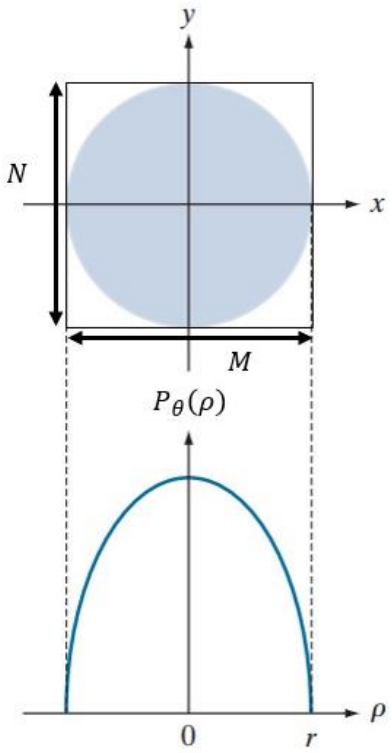

Figure 2.3. A circle (top) and its Radon transform (bottom). The circle is circumscribed by a square with a side *M* parallel to the projection line ρ and a side *N* vertical to the projection line, which in this case are equal. The image is and taken from [18] and modified.

line integral, $P_{\theta_k}(\rho_j)$, corresponds to a single point in the projection distribution, $P_{\theta_k}(\rho)$, for a fixed angle of rotation θ_k. Any real 2D object does not possess an analytic expression for the Radon transform so we must consider the discrete case of the Radon transform, where the projection of the two-dimensional object $f(x,y)$ is a discretized function. Then equation (2.4) becomes,

$$P_\theta(\rho) = \sum_{x=0}^{M-1} \sum_{y=0}^{N-1} f(x,y)\delta(x\cos\theta + y\sin\theta - \rho) \qquad (2.5)$$

where x, y are now discrete variables and M, and N, are the dimensions of a rectangular area over which the transform is applied. In the example of Figure 2.3, the 2D object is circumscribed by a rectangle, where the length of the side parallel to ρ is the extension M and the perpendicular one is the extension of N. In this case due to the symmetry of the circle the *M* and *N* sides are equal, making the rectangle a square. We see Equation 2.5 sums the values of $f(x,y)$ on the discrete (x,y) coordinates along the line defined by the parameters (ρ,θ), where setting θ=constant and

incrementing through all values of ρ required to span the $M \times N$ area yields one projection. Changing θ and repeating this procedure yields another projection, Figure 2.4.

Obviously, the same procedure applies to the continuous case as well where instead the object function $f(x, y)$ and projections $P_\theta(\rho)$ are continuous.

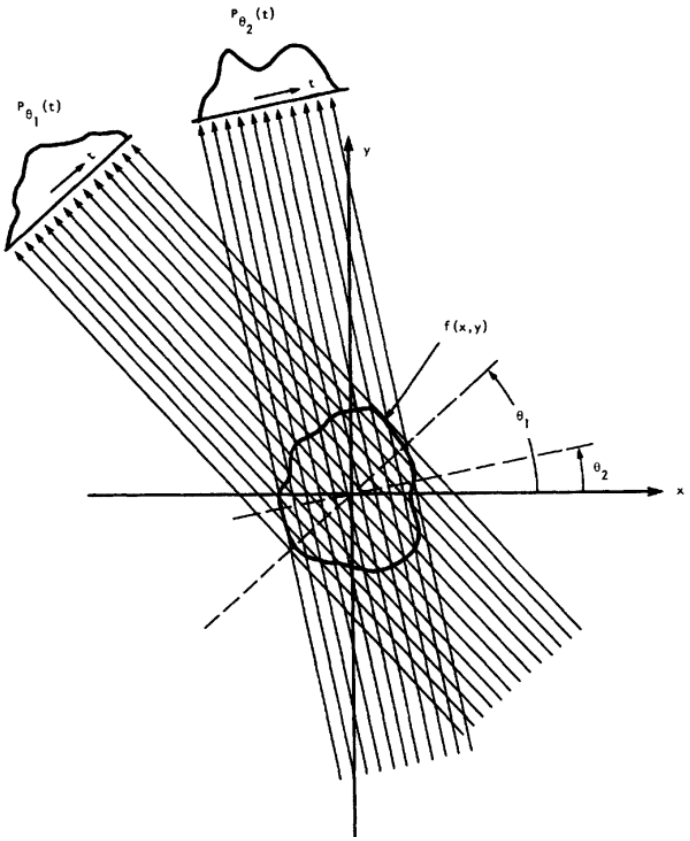

Figure 2.4. Changing θ and running through all values of ρ yields another projection, taken from [2].

Fixing the angle θ and for each value of ρ taking the line integral yields a projection, incrementing the angle and repeating the procedure yields another projection, Figure 2.4. Repeating this for each angle, i.e. taking the Radon transform of the object for each angle, produces an image, called a sinogram. The sinogram has coordinates the parameters (θ, ρ) and contains all the data necessary to reconstruct the object. Figure 2.5 shows the image of a rectangle (2D object) and its accompanying sinogram. In the image depicting the sinogram, each row corresponds to the distance ρ, while each column corresponds to the angle θ (or vice versa).

It is important to note that the value of the angle varies within a π range, due to line integral symmetry (see Equation 2.4). So, if we start at 0 angle the range would be $[0, \pi]$.Suppose, we take the projection of the object at the angles 0 and π. calculating these two projections yield identical data, as they are the same except for the direction of integration. Thus, every projection at an angle $\theta + \pi$ yields the same result as the projection at an angle θ, thus just a π interval suffices.

Turning our attention back to Figure 2.5, there are some observations we can make to the sinogram and deduce the characteristics of the object. For example, the bottom row is the projection of the rectangle in the horizontal direction, $\theta = 0°$ which means the lines of the line integrals are parallel to the longest side of the rectangle. The middle row of the sinogram corresponds to a 90° angle thus, the integral lines are vertical to the longest side. Comparing these two rows of the sinogram we see the non-zero portion of the bottom row is smaller than the non-zero portion of the middle row. This tells us that the object is narrower in the vertical direction. The fact that the sinogram is symmetric about the horizontal and vertical lines that goes through the middle of the image shows the initial object is symmetric and parallel to the x and y axes. These observations are only possible due to the simplicity of the rectangle. For a more complex object such observations are not possible as we will see in the following sections.

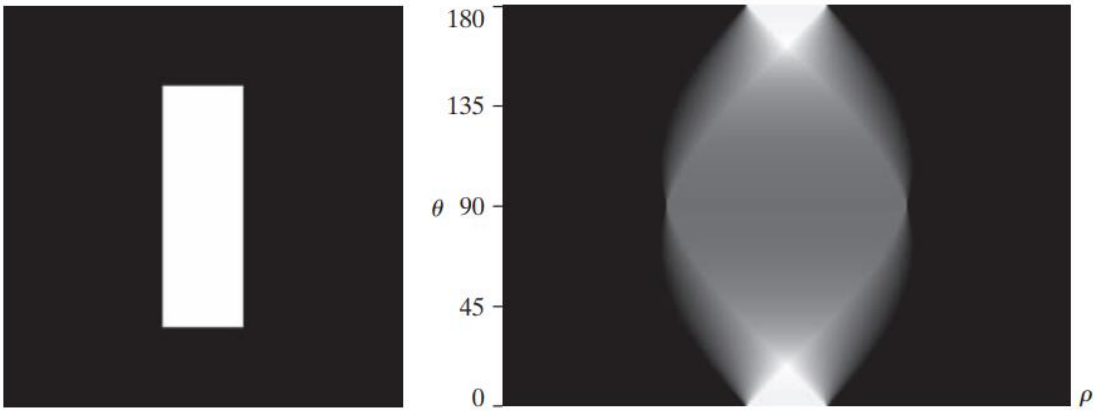

Figure 2.5. An image of a rectangle (left). Sinogram of the rectangle (right), taken from [18].

In the remainder of this section, we will present the key ideas behind reconstructing the function of the object $f(x, y)$ from the sinogram, using the method of backprojection, [18]. Suppose we are at a fixed angle θ_k and we calculate the Radon transform (Equation 2.4) on the object $f(x, y)$. The result is the function of the projection $P_{\theta_k}(\rho)$ from which we consider only one point $P_{\theta_k}(\rho_j)$, Equation 2.3. Backprojecting this single point means copying the line $L(\rho_j, \theta_k) = x\cos\theta_k + y\sin\theta_k - \rho_j$ onto the image and assigning the value of $P_{\theta_k}(\rho_j)$ on each point on the line, Figure 2.2. This way we form part of the initial image. Repeating this procedure for each ρ value while keeping fixed the value of the angle, θ_k, produces a basic reconstruction of the initial image.

In Figure 2.6, we see this procedure applied to a simple object. We have an initial object, a disk and take its projection at two angles with 90° increment. Then, for each corresponding angle we backproject the signal, i.e. the values of the projected image, at each angle and thus the sum of both backprojections is produced which is a basic reconstruction of the initial object. Using only two

projections does not provide enough information to produce a valid reconstruction of the initial object. Increasing the number of projections improves the resulting image. We can also observe the imprint of backprojection on the background of the object, which in this case appears as two perpendicular lines, each assigned values from the corresponding projections. In a later section, we will elaborate on the artifacts produced by backprojections on both the background and the object.

The previous explanation of backprojection can be expressed mathematically [2,23]. For a fixed value of θ_k the initial object function can be expressed as the backprojection of the projected object, for all values of ρ, Equation 2.3.

$$f_{\theta_k}(x,y) = P_{\theta_k}(\rho) = P_{\theta_k}(x\cos\theta_k + y\sin\theta_k) \tag{2.6}$$

where we replaced the parameter ρ with the expression of a line, Equation 2.1, at the specified angle θ_k.This equation holds for all angles, so we may generalize Equation 2.6 for an arbitrary value of angle θ_k and write the equation of an image by one backprojection at an angle θ,

$$f_{\theta}(x,y) = P_{\theta}(x\cos\theta + y\sin\theta) \tag{2.7}$$

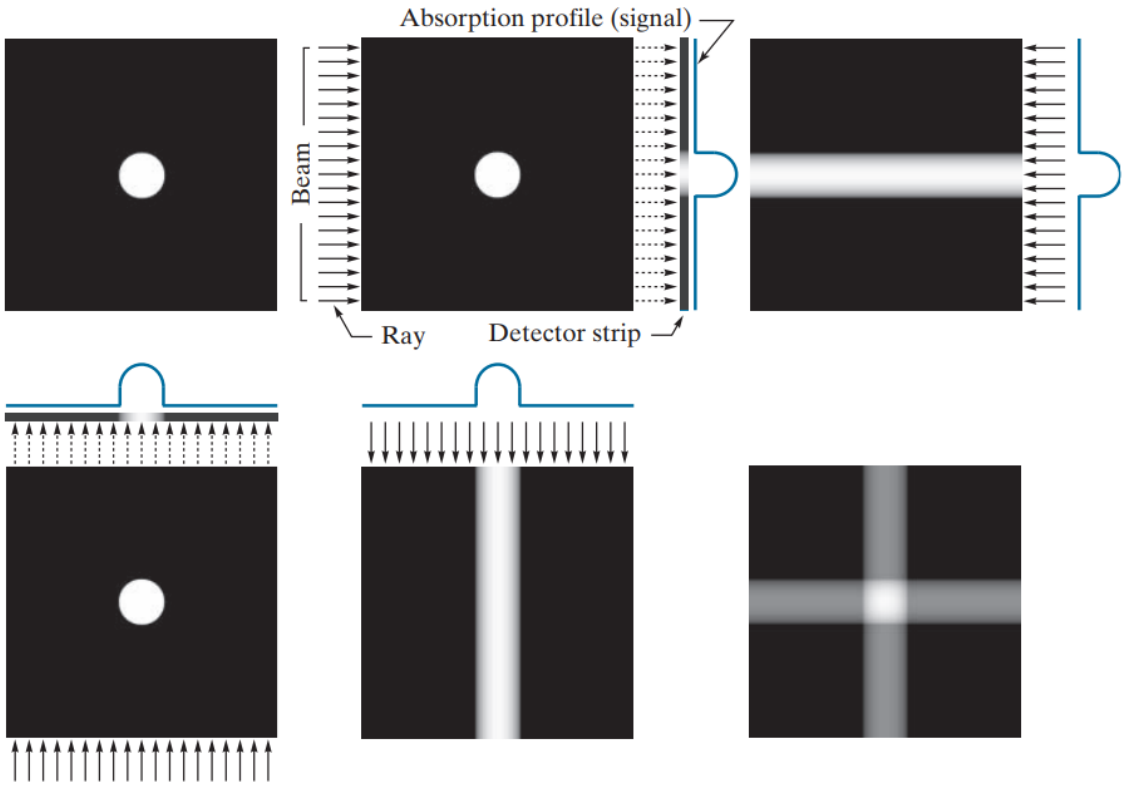

Figure 2.6. Backprojection method: A horizontal projection of an object is obtained and backprojected, then the process is repeated for a vertical angle. The contribution of both backprojections provides a basic approximation of the initial object. Image taken from [18].

The expression of the image formed by all the backprojections each at a different angle in the range

$[0, \pi]$, is obtained by integrating with respect to θ Equation 2.7,

$$f(x,y) = \int_0^{\pi} f_\theta(x,y)d\theta \tag{2.8}$$

As previously mentioned, continuous projections and backprojections of the initial object are not realistically feasible, so we must adopt the discrete case where integrals are replaced by sums.

$$f(x,y) = \sum_{\theta=0}^{\pi} f_\theta(x,y) \tag{2.9}$$

where x, y and θ are now discrete quantities. It is understood that the method of backprojection approximates the initial image from which the projections were generated. This fact is illustrated in the following example. In Figure 2.7, Equation 2.9 was used to create the backprojected

Figure 2.7. Back-projection of a rectangle shown in Figure 2.5, left image, using Equation 2.9, taken from [18].

image of the initial object, a rectangle, shown on the left side of Figure 2.5. Clearly the reconstructed image is degraded in sharpness (a halo blurring effect) which makes this recovery method not very useful. In a later section an improved method will be introduced.

2.2. Fourier slice theorem

The process described above involves taking projections of an initial 2D object using the Radon transform, either in its continuous form (Equation 2.4), or discrete form (Equation 2.5), for various angles θ in the range $[0, \pi]$. The projection data are then compiled into a sinogram, from which the initial 2D object can be reconstructed using the backprojection method (Equation 2.9). In

this section, we will present a mathematical theorem that forms the foundation of the tomographic method, specifically the filtered backprojection method, which will be discussed later.

We will derive a mathematical equation that establishes the relationship between the 1-D Fourier transform of a projection and the 2-D Fourier transform of the slice of the initial object from which the projection was taken [2,18,24].

Suppose we have an object described by the function $f(x,y)$. Its 2-D Fourier transform [2,28] is given by,

$$F(u,v) = \int_{-\infty}^{+\infty}\int_{-\infty}^{+\infty} f(x,y)e^{-i2\pi(ux+vy)}dxdy \tag{2.10}$$

where u and v are spatial frequencies in the frequency domain of the Fourier transform. Next, we take a projection, $P_\theta(\rho)$, of the object at a fixed angle value, θ, and define its 1-D Fourier transform,

$$S_\theta(w) = \int_{-\infty}^{+\infty} P_\theta(\rho)e^{-i2\pi w\rho}d\rho \tag{2.11}$$

Now, consider the Fourier transform of the object function $f(x,y)$, Equation 2.10, along the line $v = 0$ in the frequency domain. The 2-D Fourier transform simplifies to

$$F(u,0) = \int_{-\infty}^{+\infty}\int_{-\infty}^{+\infty} f(x,y)e^{-i2\pi ux}dxdy \tag{2.22}$$

In this case, the phase factor is independent of the *y* variable, so the integral can be separated into two parts,

$$F(u,0) = \int_{-\infty}^{+\infty} e^{-i2\pi ux}dx\left[\int_{-\infty}^{+\infty} f(x,y)\,dy\right] \tag{2.13}$$

We can recognize the term in brackets as the projection, Equation 2.4, of the object function $f(x,y)$ at an angle $\theta = 0$, along lines of constant $x = \rho$, as shown in Figure 2.8,

$$P_{\theta=0}(x) = \int_{-\infty}^{+\infty} f(x,y)dy \tag{3.14}$$

Substituting Equation 2.13 into Equation 2.12 yields,

$$F(u,0) = \int_{-\infty}^{+\infty} P_{\theta=0}(x)e^{-i2\pi ux}dx \tag{2.15}$$

The right-hand side of Equation 2.15 represents the 1-D Fourier transform of the projection $P_{\theta=0}$ at an angle $\theta = 0$. This illustrates the Fourier Slice Theorem [2,18,30] for the simplest case, where a projection is taken at an angle $\theta = 0$. The theorem establishes the relationship between the 2-D Fourier transform of the object function $f(x,y)$ along the line $v = 0$, denoted as $F(u,0)$, and the 1-D Fourier transform of the projection at angle $\theta = 0$, denoted as $S_{\theta=0}(u)$,

$$F(u,0) = S_{\theta=0}(u) \tag{2.16}$$

A visual representation of this equation is shown in Figure 2.8. Figure 2.8(a) displays the Shepp and Logan “head-phantom”, [29], which is a superposition of 10 ellipses. In this figure we observe a red line at an angle of $\theta = 0$ with respect to the horizontal axis. This line is perpendicular to the straight lines along which the projection of the “head phantom” is taken. At the top of the image the projection is shown as a plot with the variable ρ on the horizontal axis. Figure 2.8(b) presents the 2-D Fourier transform of the “head phantom in the frequency domain as a set of complex numbers. The horizontal axis represents the u parameter and the vertical axis represents the v parameter. The data along the red line correspond to the 1-D Fourier transform of the projection at an angle $\theta = 0$ as dictated by the Fourier Slice Theorem.

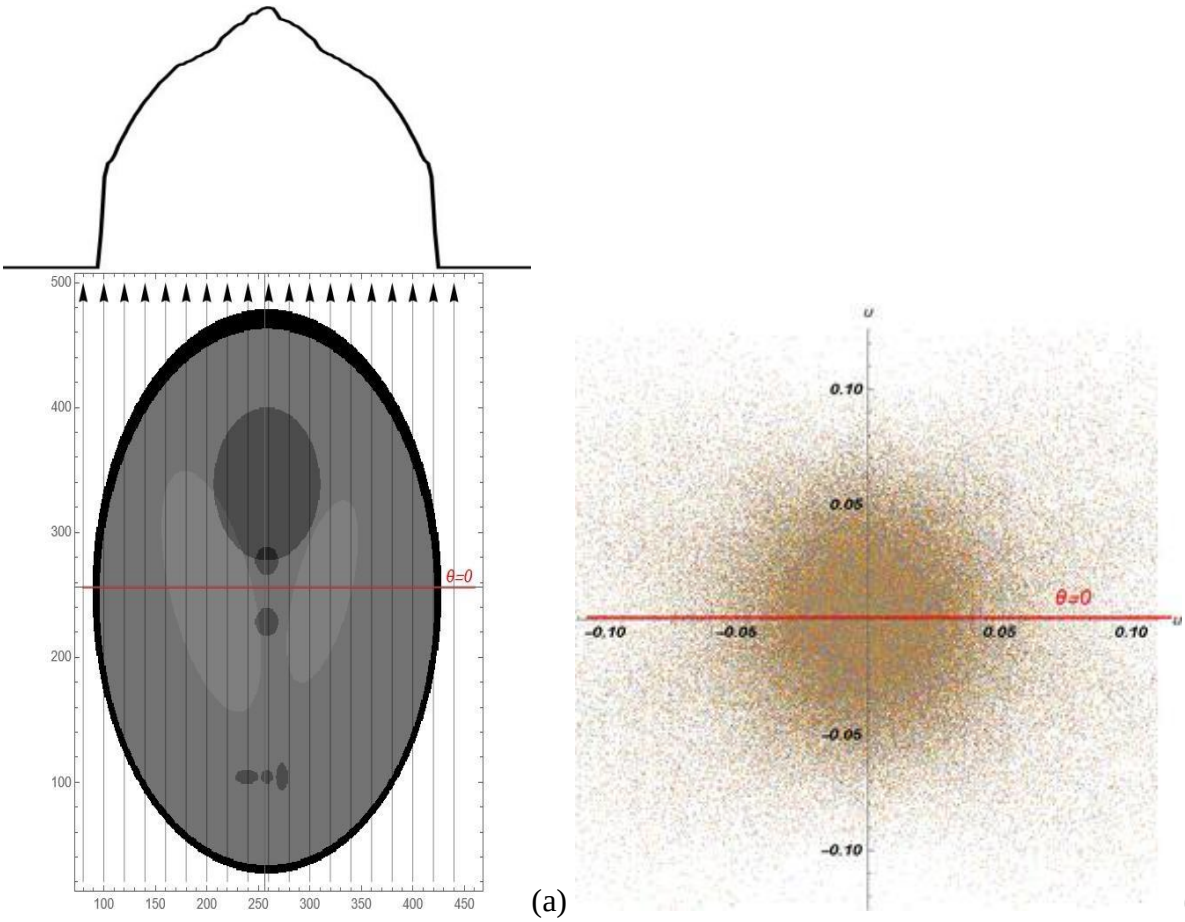

Figure 2.8.(a)The projection of the Shepp and Logan "head-phantom" at an angle $\theta = 0$.(b)The 2-D Fourier transform of the “head phantom” and the red line where the Theorem applies.

As mentioned, Equation 2.15 represents the simplest form of the Fourier Slice Theorem. This theorem also extents to projections taken at an arbitrary angle θ. By rotating the coordinate system (ρ, s), which is the coordinate system of the projected object, by an angle θ, the Fourier transform of the projection, as defined in Equation 2.11, is equivalent to the 2-D Fourier transform of the object along a line rotated by θ, illustrated in Figure 2.9. This means that the Fourier transform of a

projection at an angle θ can provide the values of the 2-D Fourier transform of the original object along a line at an angle θ matching the angle used to generate the projection. Thus, the Fourier Slice Theorem, [30,31] for an arbitrary angle θ can be stated as follows:

The 1-D Fourier Transform of a projection $S_\theta(u)$ of an object with function $f(x,y)$ taken at an angle θ is a slice of the 2-D Fourier transform $F(u,v)$ of the object function along a line oriented at the same angle as the angle used in the projection.

In the following paragraphs, we will provide a more rigorous mathematical definition for the Fourier Slice Theorem [2,18].

Let us begin by considering the (ρ, s) coordinate system of the projection as a rotated version of the original (x, y) system:

$$\begin{bmatrix}\rho\\ s\end{bmatrix} = \begin{bmatrix}\cos\theta & \sin\theta\\ -\sin\theta & \cos\theta\end{bmatrix}\begin{bmatrix}x\\ y\end{bmatrix} \tag{2.17}$$

In the (ρ, s) coordinate system, a projection along lines of constant ρ is given by,

$$P_\theta(\rho) = \int_{-\infty}^{+\infty} f(\rho, s)ds \tag{2.18}$$

And from Equation 2.11, its Fourier transform is defined as,

$$S_\theta(w) = \int_{-\infty}^{+\infty} P_\theta(\rho)e^{-i2\pi w\rho}d\rho \tag{2.19}$$

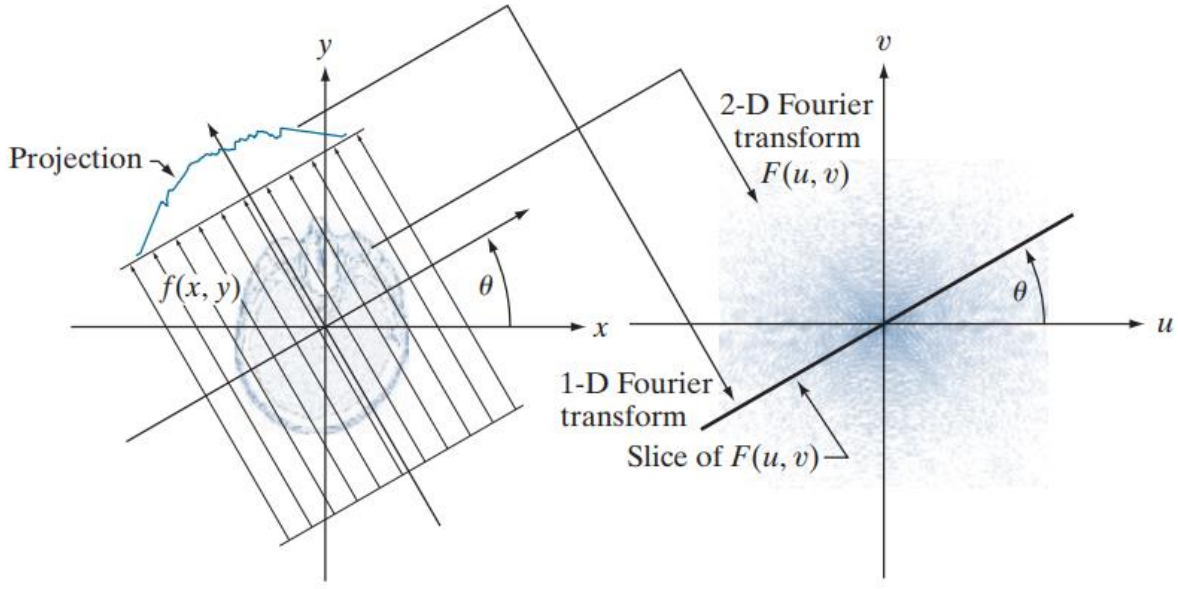

Figure 2.9.The Fourier Slice Theorem is independent of the of orientation between the object and the coordinate system (ρ, s).The Fourier transform of a projection is equal to the Fourier transform of the object along a radial line of angle θ, taken from [18].

Substituting the definition of the projection in the (ρ, s) coordinate system, given by Equation 2.18, into Equation 2.19 yields,

$$S_\theta(w) = \int_{-\infty}^{+\infty} \left[\int_{-\infty}^{+\infty} f(\rho, s) ds \right] e^{-i2\pi w\rho} d\rho \tag{2.20}$$

This equation can be transformed into the (x, y) coordinate system using Equation 2.17. The Jacobian of this matrix is 1 and so Equation 2.20 transforms to,

$$S_\theta(w) = \int_{-\infty}^{+\infty} \int_{-\infty}^{+\infty} f(x, y) e^{-i2\pi w(x\cos\theta + y\sin\theta)} dx dy \tag{2.21}$$

The right-hand side represents the 2-D Fourier transform of the object function, $F(u, v)$, at a spatial frequency or wavenumber of $(u = w\cos\theta, v = w\sin\theta)$.

Therefore, Equation 2.21 can be expressed as,

$$S_\theta(w) = F(u, v) = F(w\cos\theta, w\sin\theta) \tag{2.22}$$

This equation is the general form of the Fourier Slice Theorem. It essentially indicates that by taking N projections of the initial object function at various angles $\theta_1, \theta_2, \dots, \theta_N$ and taking the 1-D Fourier transform of each of these, we can determine the values of the 2-D Fourier transform $F(u, \upsilon)$ along radial lines of corresponding angles $\theta_1, \theta_2, \dots, \theta_N$. Therefore, the determination of the full $F(u, \upsilon)$ function is possible by taking an infinite number of projections. By knowing $F(u, \upsilon)$, the initial object function can be recovered by taking its 2-D inverse Fourier transform,

$$f(x, y) = \int_{-\infty}^{+\infty} \int_{-\infty}^{+\infty} F(u, \upsilon) e^{i2\pi(ux + \upsilon y)} du d\upsilon \tag{2.24}$$

However, this approach is not ideal because it is computationally demanding and introduces error to the data through interpolation [32], which leads to image degradation.

2.3. Filtered Backprojection

In the previous section, we derived the Fourier Slice Theorem which establishes a relationship between the Fourier transform of a projection and the 2-D Fourier transform of the object along a radial line. Therefore, obtaining the Fourier transforms of projections from enough angles allows for the compilation of these projections into a complete representation of the 2-D Fourier transform of the object. An estimate of the initial object can then be obtained using a straightforward 2-D inverse Fourier transform. However, this approach is not desirable for the reasons mentioned above, thus requiring the use of a different method, filtered backprojection.

In Section 2.1 we provided a basic definition and explanation of the backprojection method, Equations 2.6-2.9. Now, we will further expand on the backprojection method, focusing specifically on the filtered backprojection method and establish its mathematical formulation. We will derive this method using the Fourier Slice theorem and the inverse Fourier transform in polar coordinates.

2.3.1 Basic idea

Before explaining the basics of filtered backprojection it is essential to address a key characteristic of the projections, their independence from each other. This independence becomes evident in the frequency domain, where performing the Fourier transform to the projection reveals, according to the Fourier Slice theorem (Equation 2.22), that a projection corresponds to a line of angle θ with the horizontal axis that goes through the origin of the plane (u, v) [31].

Performing another projection in a different angle, its Fourier transform corresponds to a different line of the same angle. These two lines are nearly independent where the only intersection is at the origin of the axes $(0,0)$,see Figure 2.10.[18]

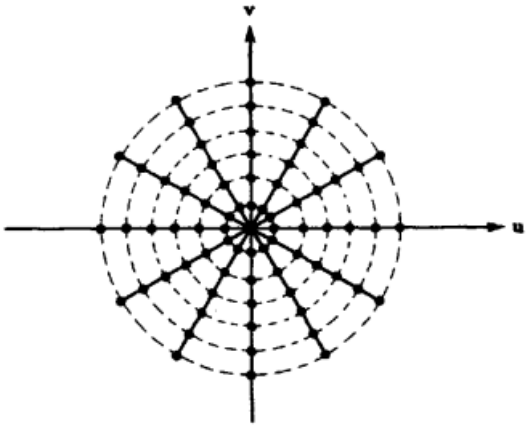

Figure 2.10. Frequency domain where the lines correspond to both the Fourier transform of a projection and a segment of the Fourier transform of the initial object, due to the Fourier Slice Theorem, taken from [18].

Thus, each projection contributes independently of each other to the reconstruction of the initial object, making the backprojection method conceptually simple.

Filtered Backprojection can be broken down into two parts: the filtering part and the back projection part. The filtering part can be visualized as the weighting of each projection in the frequency domain. Consider Figure 2.10, where concentric circles of radius (or frequency) w, represent points corresponding to projections taken at various angles. The distribution of points on the circumference of a circle is denser for lower frequencies (or radii) and sparser for higher frequencies (or radii). As a result, the contribution of lower frequencies is more significant than that from the higher frequencies. To enhance higher frequencies and reduce the impact of lower frequencies, each line in the frequency domain is multiplied by an appropriate weighting function $|w|$ [18]. This function is often multiplied by a more complex function that serves as a high pass filter [18]. The product of the weight function and the high pass filter is often called filtering function. Generally, lower frequencies are associated with broad, large-scale features of the reconstructed

object such as its shape and structure, while high frequencies correspond to fine details and image clarity. However, high frequencies are more susceptible to noise making necessary the use of a sophisticated filter to reduce noise while preserving essential details in the reconstructed images.

The second part of filtered backprojection process is backprojection. After applying the filtering function to each Fourier transformed projection,$S_\theta(w)$, we obtain the filtered Fourier transformed projection. We then apply the inverse Fourier transform to retrieve the filtered projection and subsequently backproject it. The backprojection of the filtered projections is performed in the same manner as described in Figure 2.6 of Section 2.1. In essence, each point in the filtered projection corresponds to a line along which the projection was calculated. This line traverses the image at an angle corresponding to the point from the filtered projection, thereby filling the image with that specific value along the entire line.

Repeating this procedure for each point in the filtered projection and its corresponding line assembles an estimate of the initial object. As the number of projections and thus filtered backprojections increases the reconstructed object more accurately resembles the original, as shown in Figure 2.11.

Schematically, filtered back projection can be summarized as follows.

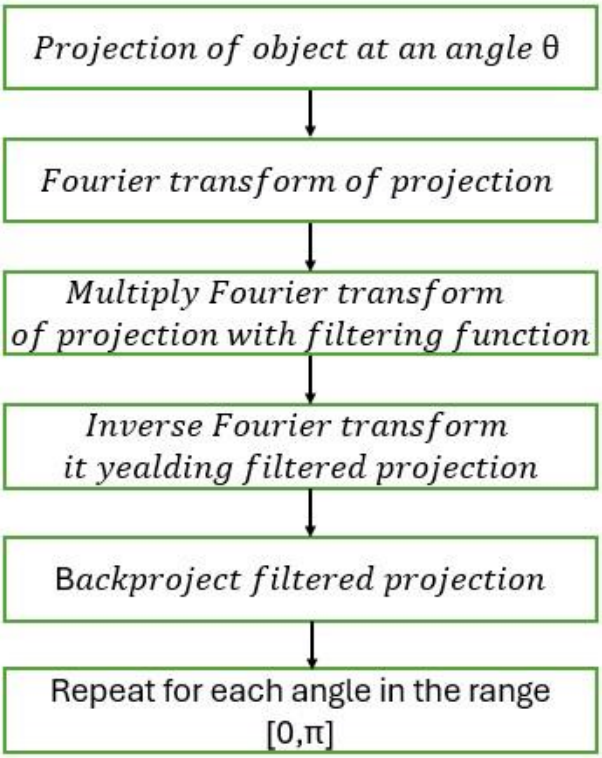

2.3.2 Mathematical Formulation

In this section we will derive the filtered backprojection using the Fourier Slice Theorem. The inverse Fourier transform of the 2-D Fourier transform of the object function $f(x,y)$, as given by Equation 2.10, can be expressed as,

$$f(x,y) = \int_{-\infty}^{+\infty} \int_{-\infty}^{+\infty} F(u,v) e^{i2\pi(ux+vy)} du dv \tag{2.25}$$

We transform the rectangular coordinate system of the frequency domain (u,v) into a polar coordinate system (w,θ) using the relations,

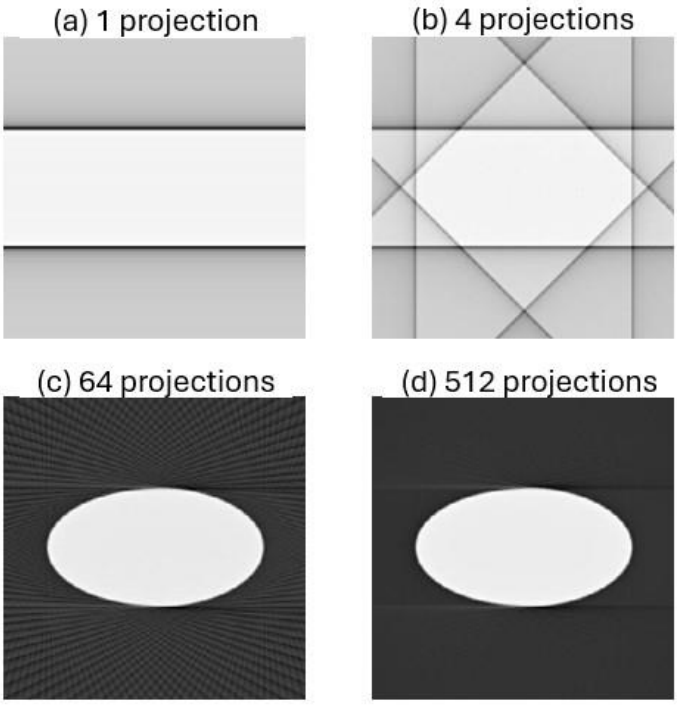

Figure 2.11. Result of filtered backprojection of an ellipse for, (a) a single angle, (b),4 angles, (c),64 angles, (d)512 angles.]

$$u = w\cos\theta \tag{2.26}$$

$$v = w\sin\theta \tag{2.27}$$

and changing the differential using the fact that the Jacobian is w,

$$dudv = wdwd\theta \tag{2.28}$$

Equation 2.24, can be written in polar coordinates using Equations 2.25-2.27 and making the appropriate changes in the integral limits,

$$f(x,y) = \int_{0}^{2\pi} \int_{0}^{\infty} F(w,\theta) e^{i2\pi w(x\cos\theta + y\sin\theta)} w dw d\theta \tag{2.29}$$

The integral can be split into two parts one for θ in the range 0 to π and the other for θ in the range π to 2π,

$$f(x,y) = \int_0^{\pi}\int_0^{\infty} F(w,\theta)e^{i2\pi w(x\cos\theta+y\sin\theta)}wdwd\theta + \int_0^{\pi}\int_0^{\infty} F(w,\theta+\pi)e^{i2\pi w\left(x\cos(\theta+\pi)+y\sin(\theta+\pi)\right)}wdwd\theta \quad (2.210)$$

Then using the property of $F(w,\theta)$,

$$F(w,\theta+\pi) = F(-w,\theta) \quad (11)$$

which is evident by considering the Fourier Slice Theorem for an arbitrary angle Equation 2.22. By applying Equation 2.30, Equation 2.29 can be written as,

$$f(x,y) = \int_0^{\pi}\left[\int_{-\infty}^{+\infty} F(w,\theta)|w|e^{i2\pi w\rho}dw\right]d\theta \quad (12)$$

where we have simplified the expression by setting,

$$\rho = x\cos\theta + y\sin\theta \quad (13)$$

Using the Fourier Slice theorem, Equation 2.22, $F(w,\theta)$ is substituted with the Fourier transform of a projection at an angle θ,$S_\theta(w)$. Therefore Equation 2.31 becomes,

$$f(x,y) = \int_0^{\pi}\left[\int_{-\infty}^{+\infty} S_\theta(w)|w|e^{i2\pi w\rho}dw\right]d\theta \quad (14)$$

Defining the following expressions,

$$Q_\theta(\rho) = \int_{-\infty}^{+\infty} S_\theta(w)|w|e^{i2\pi w\rho}dw \quad (15a)$$

$$Q'_\theta(\rho) = \int_{-\infty}^{+\infty} S_\theta(w)h(w)|w|e^{i2\pi w\rho}dw \quad (16b)$$

Equation 33, simplifies to

$$f(x,y) = \int_0^{\pi} Q'_\theta(x\cos\theta + y\sin\theta)d\theta \quad (17)$$

This equation encapsulates the essence of the Filtered Backprojection method. Given the projections at various angles ,$S_\theta(w)$, these are filtered using the weight $|w|$ and an additional function $h(w)$. The result of this process is $Q'_\theta(\rho)$,the filtered projections, Equation 2.34b. The backprojection of these filtered projections over the range of angles $[0,\pi]$, as described in Equation 2.35, assembles an approximation of the original object function.

Figure 2.13(a) shows the $|w|$ weighting function in the frequency domain. This filter is called ramp filter or Ram-Lak [33]. As mentioned, an additional function, called window function, is usually applied to the weight $|w|$, limiting it to a defined frequency interval. This process known as band-limiting ensures that the weighting function becomes zero outside this interval. A simple window function would be the box function,

$$h(w) = \begin{cases} 0, |w| > \frac{1}{2} \\ \frac{1}{2}, |w| = \frac{1}{2} \\ 1, |w| < \frac{1}{2} \end{cases} \tag{2.318}$$

On the left of Figure 2.12 we observe the graph of the box function in the frequency domain and on the right, we observe it in the spatial domain after applying the inverse Fourier transform. We can observe that the Fourier transform of the box function is highly oscillatory. Figure 13(b) displays the result of multiplying the box function with the weight $|w|$, which effectively bandlimits it. However, when the inverse Fourier transform is applied to this product the oscillatory nature of the box function becomes evident, as shown in Figure 2.13(c). This can lead to unwanted artifacts in the reconstructed image artifacts which can manifest as halos around the edges of the image [18].

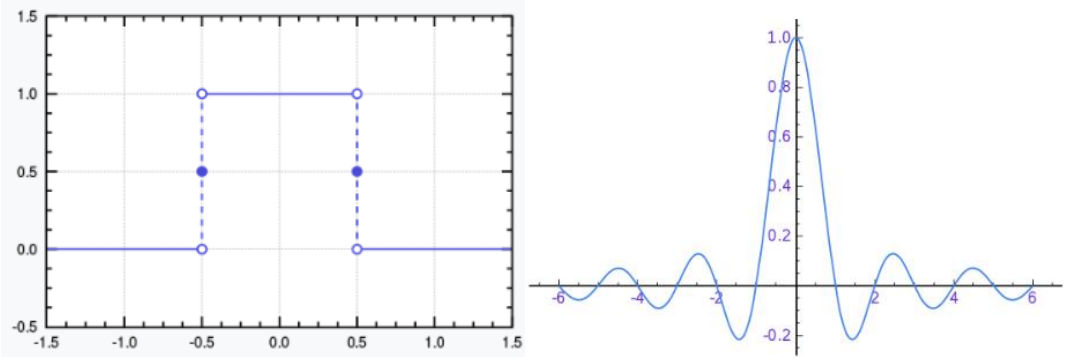

Figure 2.12.Graph of a Box function (left), Graph of the Fourier transform of a box function (right) taken from[18].

To reduce the occurrence of such artifacts, smoother window functions are applied [18], such as:

$$h(w) = \begin{cases} c + (c-1)\, cos\frac{2\pi w}{M}, & 0 \le w \le (M-1) \\ 0 & otherwise \end{cases} \tag{19}$$

Hamming window [34] is the function when $c = 0.54$,as shown in Figure 2.13(d) and Hann window [35] when $c = 0.5$ and M is the number of points.

The difference between these two filters is that the end points are zero in the Hann window, Figure 2.13(e) shows the product between the Hamming window and the $|w|$ filter in the frequency domain. Applying the inverse Fourier transform to their product, thus transferring it to the spatial domain, we observe a reduction in ringing artifacts, see Figure 2.13(f). However, the wider central lobe may result in slightly more blurring [18]. In our work the reconstruction is performed by applying the ramp filter multiplied by a Hann window, which is particularly effective for noisy data [36]

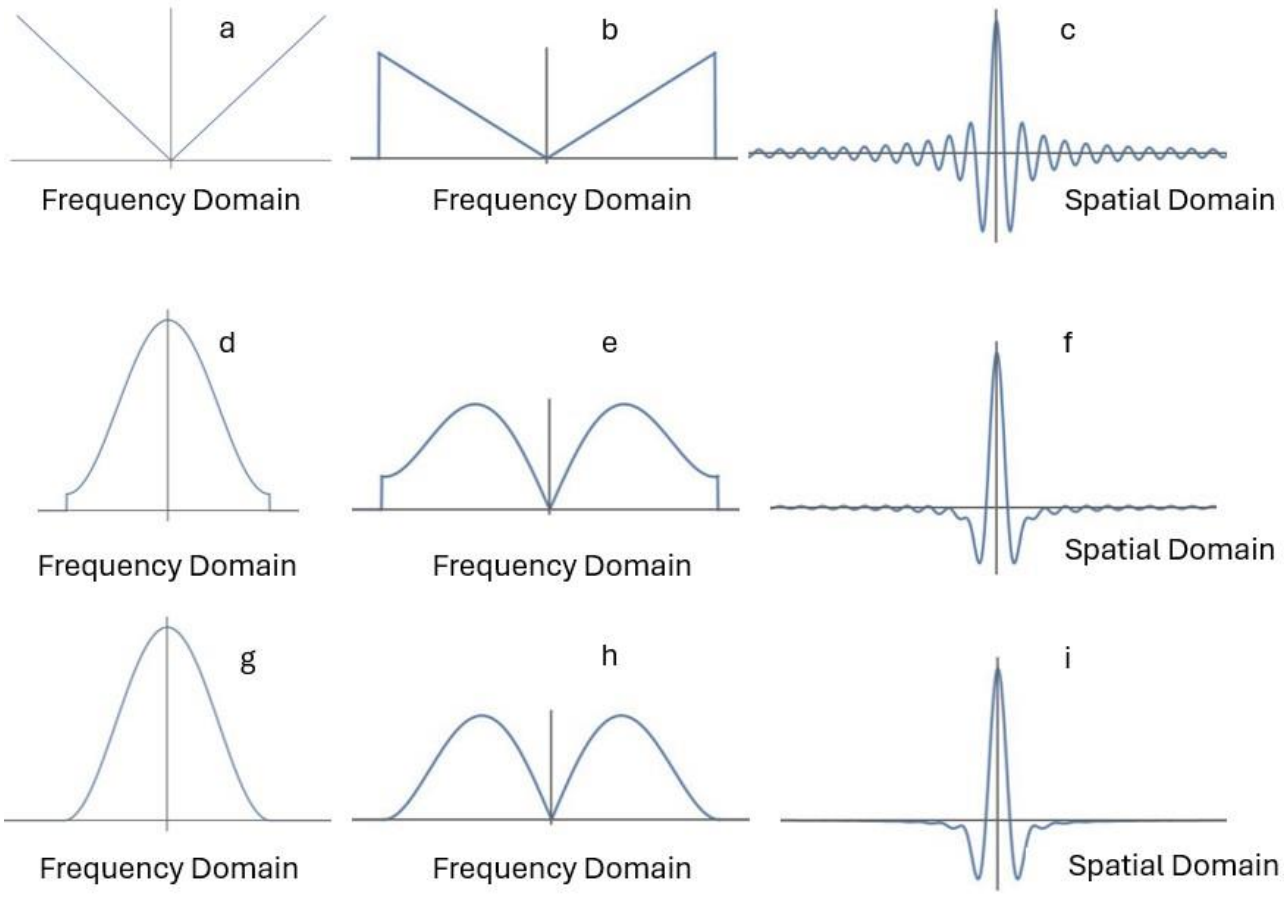

Figure 2.13.(a) Weight function $|w|$ in the frequency domain, (b) Product of weight function with box function in the frequency domain, (c) Product of weight function with box function in the spatial domain, (d) Hamming window function in the frequency domain, (e) Product of weight function with Hamming window function on the frequency domain, (f) Product of Hamming window function with weight function in the spatial domain, (g) Hann window function in the frequency domain, (h) Product of Hann window with weight function in the frequency domain, (i) Product of Hann window with weight function in the spatial domain

Two main factors should be considered to minimize unwanted artifacts in the reconstructed image. The first factor is the number of rays used in each projection, which refers to the number of samples or points considered in each projection. The second factor is the number of projections, or the number of rotation angles used in the reconstruction of the image. Undersampling a projection or using too few rotation angles (or projections) can lead to unwanted artifacts and distortions in the reconstructed image, as demonstrated in Figure 2.14.

Undersampling a projection meaning computing the line integrals at only a few points leads to aliasing artifacts [37] such as streaks. This is demonstrated in Figure 2.14, where the first row shows that for 64 samples per projection these artifacts persist, even when increasing the number of projections. On the other hand, an inadequate number of projections can lead to aliasing artifacts such as Moiré patterns [18], which are a type of interference patterns. These are shown in the first column for 64 projections and remain even with considerable sampling. Backprojection from a limited

number of projections can also introduce a star shaped pattern [38] which is relatively more visible in the last row of the first column.

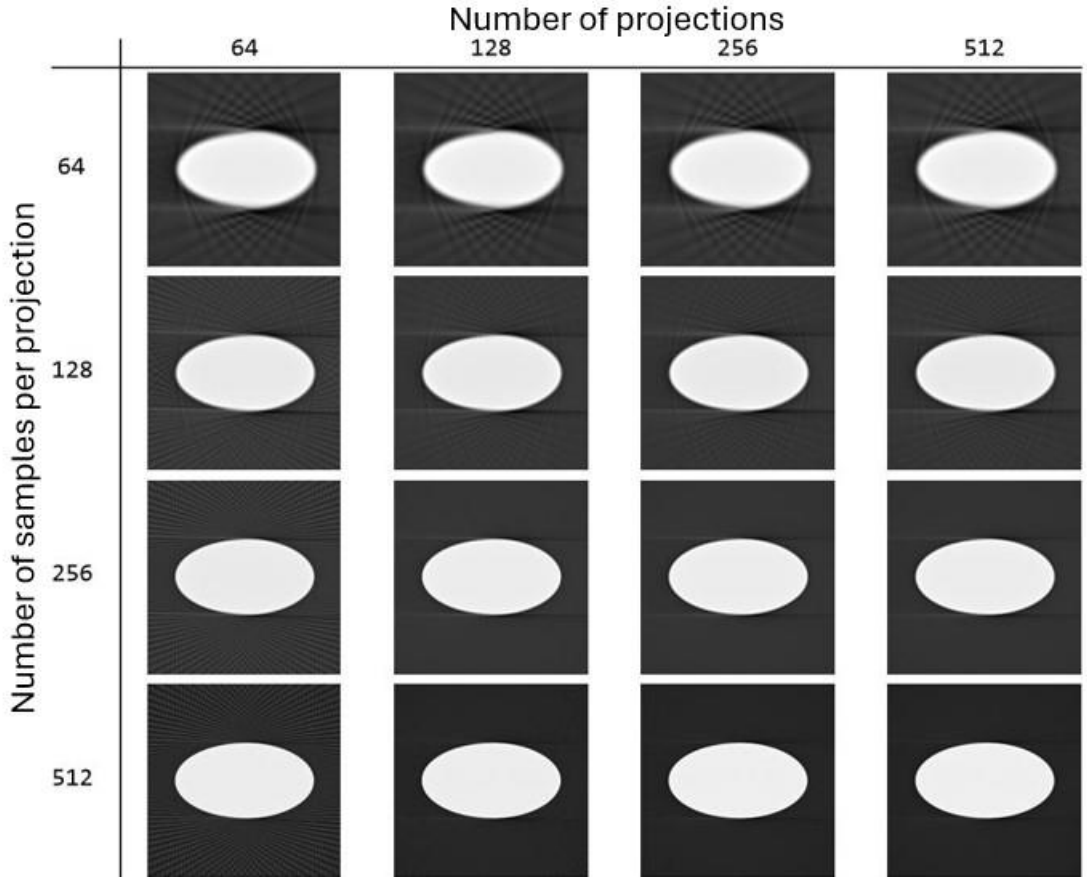

Figure 2.14.Reconstruction of an ellipse is shown for a varying number of projections (columns of image) and a varying number of samples or rays user per projection (rows of image).

The reconstructed image with seemingly no artifacts is produced using 512 projections and 512 samples per projection. A reasonable question that may arise is what the ideal number of projections and samples is, to accurately reconstruct an image without the appearance of artifacts. It is well established [18,39] that for an $N \times N$ reconstructed image, the number of samples should be approximately N, and the number of projections should also be roughly N. In practice, however, satisfactory results can be achieved with fewer projections, while maintaining the level of sampling approximately to N.

The theory introduced until now applies to 2D image. This process can also be used to reconstruct a 3D object by dividing it into 2D slices and reconstructing each slice. The stacking of these slices forms the initial 3D object.

The tomographic reconstruction of a 3D photofragment distribution is shown in Figure 2.15. By rotating the distribution in increments of a specified angle a, a 2D projection is taken at each respective angle. These projections can then be converted into a set of sinograms, each corresponding

to a slice of the distribution that is parallel to the (x, y) plane. By performing the filtered backprojection method on each sinogram, the initial slices are recovered. When these slices are combined, they reconstruct the full 3D distribution.

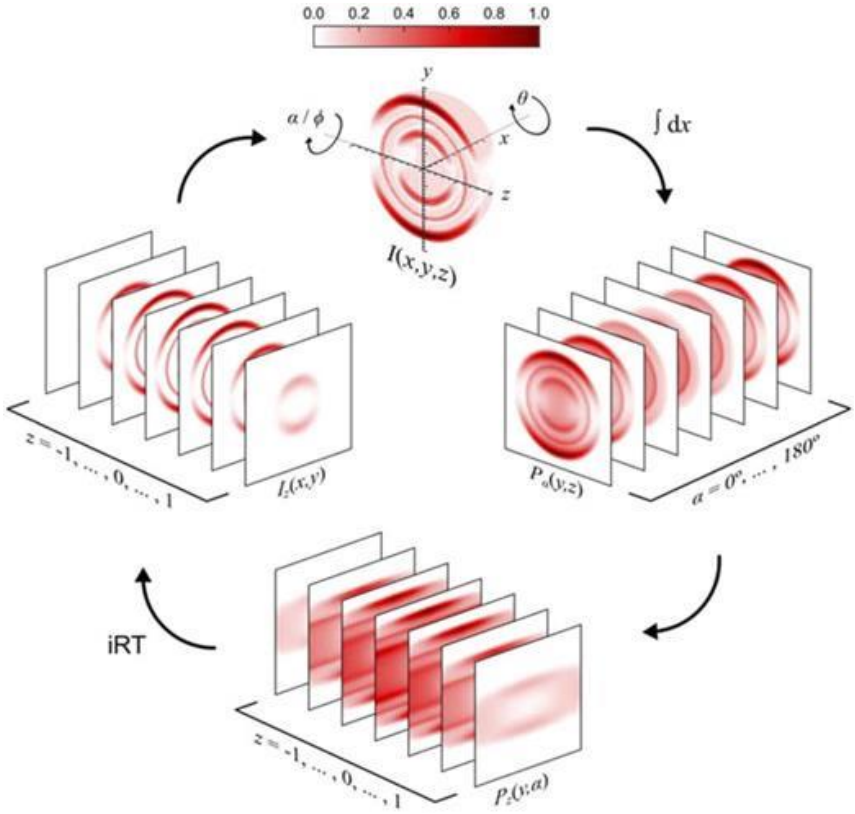

Figure 2.15. Reconstruction of a 3D distribution by dividing it into slices and applying the tomographic process to each slice individually. Image taken from [40].

This process will be used in the next section to tomographically reconstruct the 3D PADs produced by our data.

.

3. Results and Discussion

3.1. Description of "Experimental Setup"

3.1.1. Basics

The hypothetical configuration of the apparatus consists of a jet of matter interacting with an appropriately polarized beam of laser within a VMI spectrometer. The photoproducts of this light matter interaction are accelerated by the VMI and impinged onto a detector screen which is connected to a computer where the projected images are saved. The basic components of a Velocity Map Imaging experiment are shown schematically in Figure 3.1.1. A laser beam of specified polarization, in this case linear, interacts with matter which produces charged particles that are projected with the use of an inhomogeneous electric field into the 2D plane of a detector. The electric field acts as a lens which integrates the PAD parallel to the electric field.

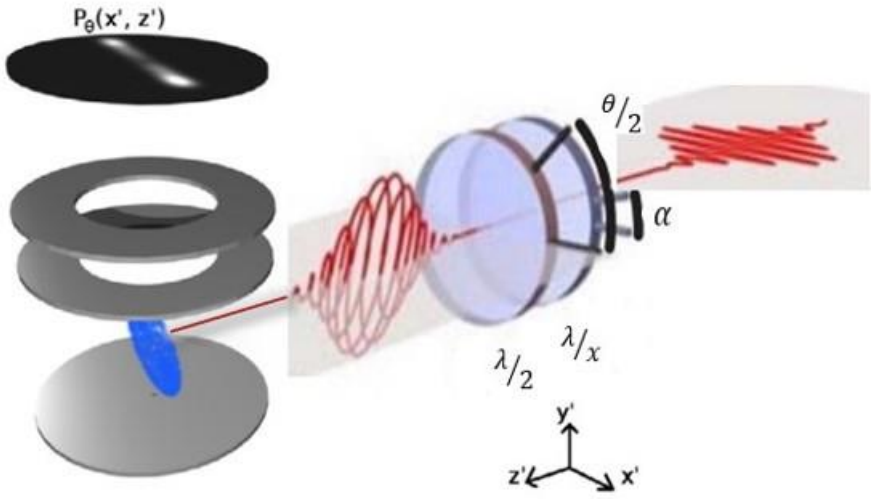

Figure 3.15.1. Experimental setup for VMI, original picture taken from [9] but modified.

We will use the VMI spectrometer [7] to reconstruct the projected images on the detector by applying tomography and the POP method where it is applicable (linear polarization). For both methods to apply the experimental arrangement should satisfy both of their requirements. Starting with the Abel inversion method it is well known [8] that the rudimentary requirement is that the laser polarization must be linear and parallel to the detector plane.

Figure 3.1.2 shows the coordinate system of the 3D distribution (x,y,z) and the 2D plane of the detector (X,Z). This configuration will be assumed for all subsequent experiments where the only variant is the polarization of light.

(1) Position the detector parallel to the (x,z) plane on a distance L from the origin.

(2) Set the light propagation vector $\hat{k}$ to be along the Oz axis.

(3) The electric field of the VMI is along the negative y-axis.

Under these conditions the Abel method can only be applied if the polarization **is along the x axis**.

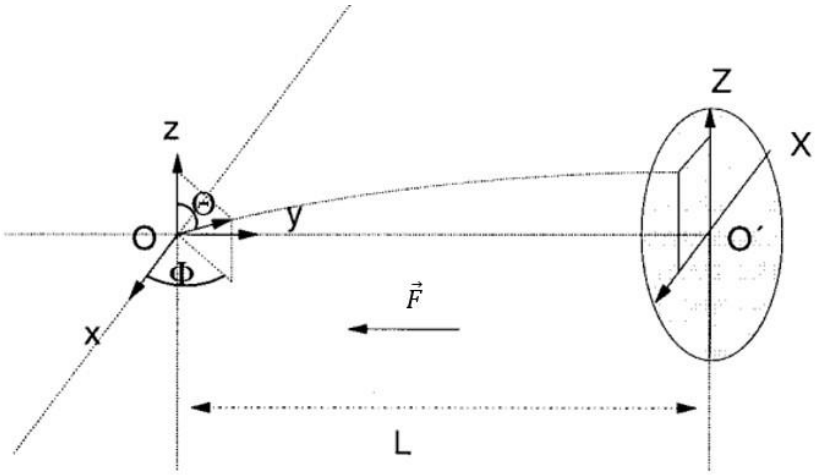

Figure 3.1.16.Coordinate system of the 3D distribution (x, y, z) and the detector plane (X, Z), original picture taken from [9], but modified.

A linear polarization of the laser field along the x-axis leads to a PAD that is cylindrically symmetric around the x-axis. Consequently, the PAD obtained on the detector is also symmetric about the X-axis. Using Abel-inversion on the projected image the y=0 slice of the initial PAD is retrieved. The y component of the distribution is not observable due to the integration along that axis. Therefore, cylindrical symmetry is required to obtain the full 4π angle distribution.

Given the three characteristics of the apparatus listed above, tomography is applicable with the addition of a half wave plate. The tomographic method involves rotating the 3D distribution around the propagation axis thereby reconstructing slices perpendicular to this axis, specifically the z-slices of the PAD. This is possible by employing a half wave plate as shown in Figure 3.1.1, which rotates the 3D distribution about the z-axis. Tomography has no limitations regarding the polarization of light and can be applied to any type: linear, elliptical, and circular polarization. Tomography is applicable to a wide range of physical processes, including both, low intensity laser fields [16] and high intensity laser fields [9]. It should be noted that an essential requirement applies to both reconstruction methods. For these methods to be feasible, the influence of the electric field of the VMI spectrometer must be completely neglected during the ionization process that produces the

PADs [41]. Consequently, the electric field should only serve as the means to project the PADs onto the detector.

The key difference between the Abel and tomography inversion methods when both apply is that the Abel method requires only one projection,i.e. one detector image. Meanwhile, for tomography to obtain the full 3D distribution information, projections of the PAD are requried from various angles (see Theory), Figure 3.1.3,demonstrates this principle of tomography.

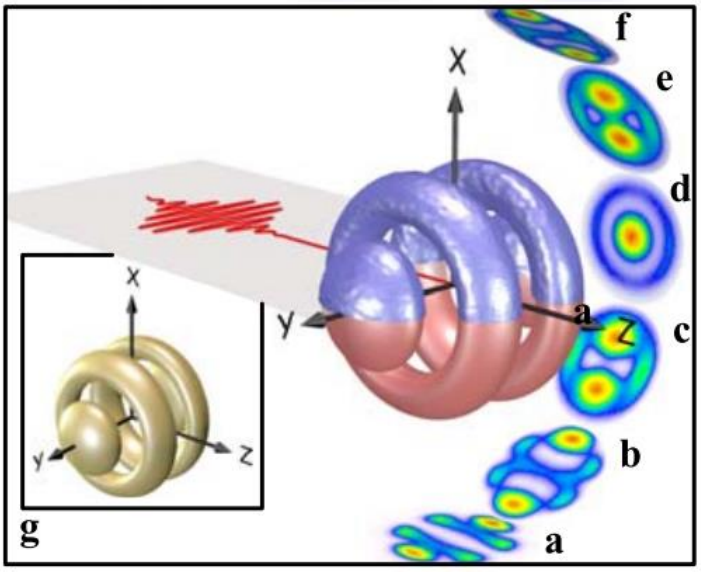

Figure 3.1.17 Detector images from 1+2 REMPI of potassium atoms with linearly polarized laser pulses at the angles $\theta = 0°(a), 15°(b), 30°(c), 45°(d), 60°(e)$ and $70°(f)$ obtained by rotation of a λ/2 waveplate by θ/2, original picture taken from [16].

For each rotation of the of the linearly polarized laser field, the produced 3D distribution rotates by the same value and is projected onto the detector. This is equivalent to keeping the polarization axis fixed, along with the 3D distribution, and projecting it from various angles. In the case of Figure 3.1.3, if the integration takes place along the y-axis then the PAD rotates around the x axis to obtain its full information in every direction.

3.1.2. CCD DETECTOR

A Charge coupled device (CCD) is used at VMI spectrometer experiments as the detector of the projected 3D PAD. The CCD consists of a grid of dots or pixels, namely flat surfaces, that act as the detecting elements. In our simulation we have simplified the function of the CCD by assuming that detection occurs at the center of the rectangular surfaces (pixels), as seen in Figure 3.1.4. According to the coordinate system defined above, see Figure 3.1.2, the CCD will be on the (x, z) plane at the coordinate $y = y_{det} = L$. The rows of the CCD are horizontal strips parallel to the x-axis

and stacking along the z-axis while the columns of the CCD are vertical strips parallel to the z-axis and stacking along the x-axis. We set the number of pixels $N_{pixels} = 201$ in each row and each column resulting in a total of 40401 pixels on the CCD. Choosing a different number of detector pixels does not inhibit the inversion method. The CCD grid should be a rectangle with dimensions at least equal to $2r_{max}$,where r_{max} is the distance of the furthest point of the distribution from the origin on the (x, z) plane. That distance varies and depends each time on the initial distribution.

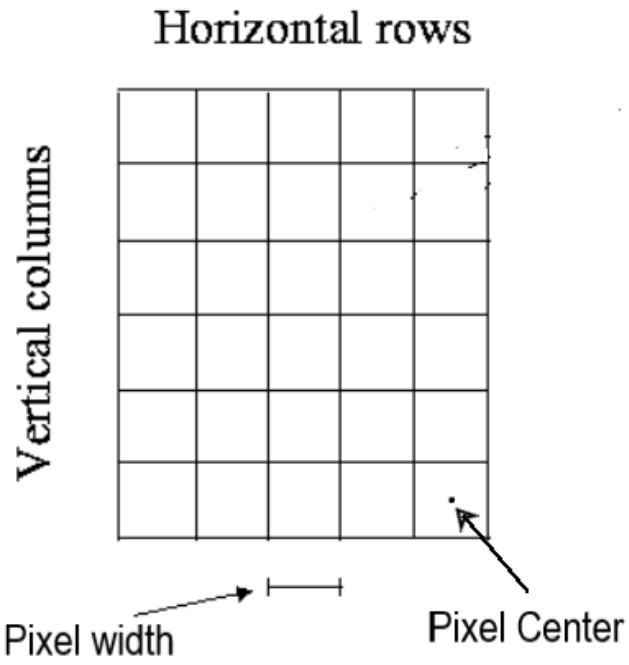

Figure 3.1.18. Grid of pixels of the CCD detector. We assume the detection occurs at the pixel center.

It is mentioned above that the projection of the PAD is performed on the pixel centers. Below, we will derive an expression to determine the pixel centers on the detector allowing us to establish the coordinate grid of these pixel centers.

First, we have to identify the maximum point of the distribution r_{max} which determines the length of the grid. The PAD is centered at the origin of the coordinate system. Suppose the cross section between the $y = 0$ plane and the PAD which lies on a plane parallel to the (x, z) plane of the detector. If r_{max} is the greatest distance that the cross section of the distribution reaches from the origin, then the square that circumscribes the 2D cross section of the distribution will have a side length of $d = 2r_{max}$ and will span the interval $[-r_{max}, r_{max}]$, as shown in Figure 3.1.5. This applies in symmetric distributions where the furthest point lies on the (x, z) plane. In a non-symmetric case, the method remains the same, but the maximum point may lie on another plane.

The pixels in a row on the CCD are 201 which have to cover the interval $[-r_{max}, r_{max}]$. If we call the distance between two consecutive pixel centers Δx then the 201 centers span a distance of 200 Δx, and we also have 0.5 Δx distance from the first pixel center to the left border and another 0.5

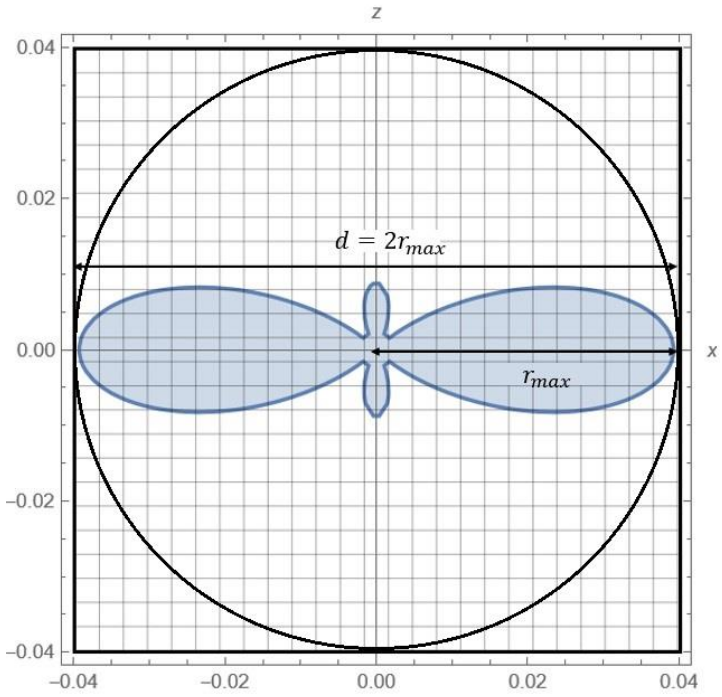

Figure 3.1.5 A z=0 cross section of the linear 3D PAD, with its maximum value r_{max} tracing a circle which is circumscribed within a square of length $d = 2r_{max}$.

Δx distance from the last pixel center to the right border. Overall, we divided the d distance to 201 equal parts and the inter-pixel spacing is

$$\Delta x = \frac{d}{N_{pixels}} = \frac{2r_{max}}{N_{pixels}} \tag{3.1}$$

Where $steps$ refer to the number of regions into which the interval d is divided. Let's expand on this idea on an arbitrary row of the 2D pixel grid of the CCD and try to calculate the pixel centers.

The position of the first pixel center according to Figure 3.1.6 is

$$1^{st} \text{ pixel: } -\frac{d}{2} + \frac{\Delta x}{2}$$

The second pixel center is the position of the first pixel center plus the inter pixel spacing Δx,

$$2^{nd} \text{ pixel: } -\frac{d}{2} + \frac{\Delta x}{2} + \Delta x = -\frac{d}{2} + \frac{3\Delta x}{2}$$

Continuing this process the center position of the nth pixel can be expressed as

$$\text{nth pixel: } -\frac{d}{2} + \frac{2n-1}{2}\Delta x \tag{3.2}$$

and by substituting Expression (3.1) into (3.2) we get:

$$\text{nth pixel: } -\frac{d}{2} + \frac{2n-1}{2\,N_{pixels}}d \tag{3.3}$$

This is an expression that yields the position of a pixel center that depends only on the width d and the number of N_{pixels}.

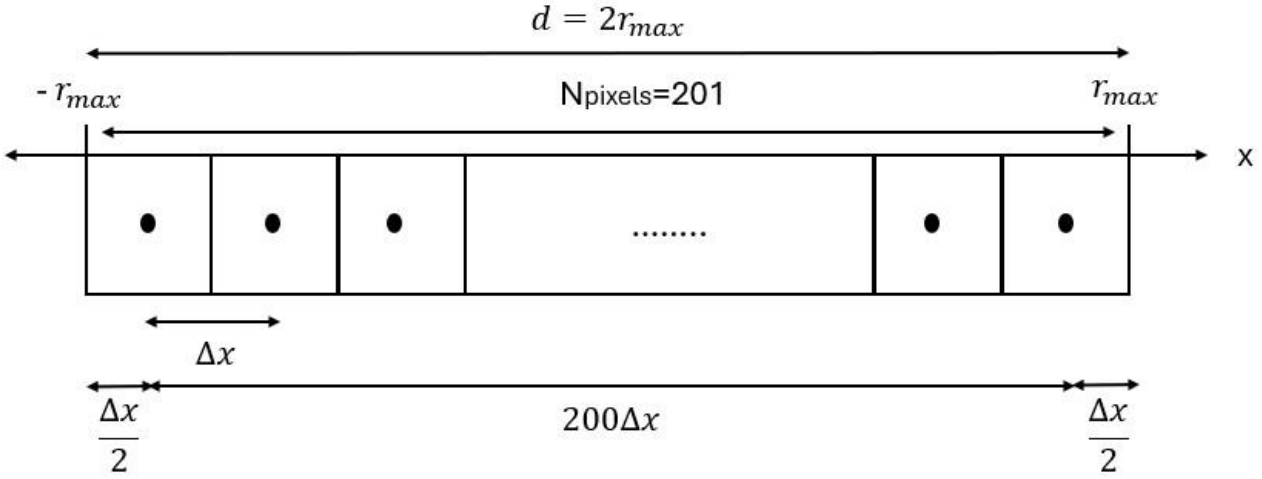

Figure 3.1.6. Positions of pixel centers in a row(x-axis) of the 2D grid of pixels of CCD.

The range of values that apply on the integer n is easily shown to be

$$1 \leq n \leq N_{pixels}$$

From this expression the x_i-positions can be written explicitly,

$$-\frac{1}{2}d + \frac{1}{2\,N_{pixels}}d, -\frac{1}{2}d + \frac{3}{2\,N_{pixels}}d, \ldots., \frac{1}{2}d - \frac{1}{2\,N_{pixels}}d$$

This method can be similarly applied to a column of the 2D grid of pixels where instead of x we have z coordinates. Thus, it is possible to identify the (x_i, z_i) positions of all pixel centers of the 2D planar grid. Expression (3.3) can also be used to discretize any plane, dividing a region into equal parts and finding the positions of the center of each interval

This grid of points allows for the evaluation of any function at these locations, resulting in its discretization, which is essential on computational analysis and is extensively used.

3.2 Projection of the PAD on the detector

In this section we are going to simulate the VMI spectrometer and the integration effect it produces on the distribution.

In our two-state system approximation, the initial PAD is defined by the general analytic function, given in Equation (A30). Our goal is to project this distribution by integrating it along the

y-axis, similar to the action of the inhomogeneous electric field in a VMI spectrometer. As seen from this equation, it is apparent that we are dealing with a linear combination of products of spherical harmonics expressed in polar coordinates.

First, we transform the distribution from polar coordinates into Cartesian coordinates, described by $A'(x, y, z)$. Then we integrate the Cartesian distribution along the y-axis where the limits of integration are the maximum y-point , y_{max}, for the POP method and the maximum distance from the origin r_{max} for tomography.

The integration is performed numerically

$$\int_{-max\ point}^{max\ point} A'(x, y, z)dy = B(x, z)$$

and the result is the function $B(x, z)$ which is the projection of the initial PAD written in terms of x and z coordinates.

The next step is the discretization of this function through the method outlined above. This involves evaluating $B(x, z)$ at the grid points on the (x, z) plane calculated by Expression (3.3)

$$B(x, z) \rightarrow B_i(x_i, z_i)$$

Where $B_i(x_i, z_i)$ is the discretized version of $B(x, z)$ with i ranging from 1 to $N_{pixels} = 201$. The next step is the normalization of $B_i(x_i, z_i)$ value to unity, enabling the valid comparison between different sets of grid points depicted as matrices or images. Figure 3.2.1 shows $B_i(x_i, z_i)$,the projected distribution discretized and normalized to unity for linear polarization. In this representation, black denotes a zero value to the pixel, while white color denotes the maximum value of 1. The maximum value can be found at the midpoint of the lobes which is expected considering the shape of the 3D distribution and the direction of integration.

3.2.1 Noise and masks

In a realistic experiment the data collected are not pure but contain an inevitable percentage of noise attached to them. To accurately assess the credibility of the inversion methods of POP and tomography, the simulated data used in our analysis should match realistic conditions.

This is achieved by adding noise to the data with the characteristic of being statistically random, which means the mean value is zero. The percentage of noise is chosen to be 1% and 5% of the maximum data value [42]. Higher levels would disproportionately represent realistic background noise in experiments.

Noise is added to the data in the form of a noise matrix resulting in the final data to be inverted, which consists of both PAD and noise data. The noise data have two characteristics. First is that the mean value has to be is zero. This means the noise values fluctuate randomly around zero, with the maximum amplitude derived from the data matrix. In the POP method, the data matrix is the projection of the PAD along the y-axis, whereas in tomography, the data matrix is produced by the projections of each rotated z-slice of the PAD. The second characteristic is that the noise matrix must have the same dimensions as the noise matrix for their addition to be possible. After these two steps, the noise matrix is multiplied by a noise factor of 0.001 or 0.005, corresponding to 1% and 5% respectively. This is then added to the data matrix and their sum is normalized to unity.

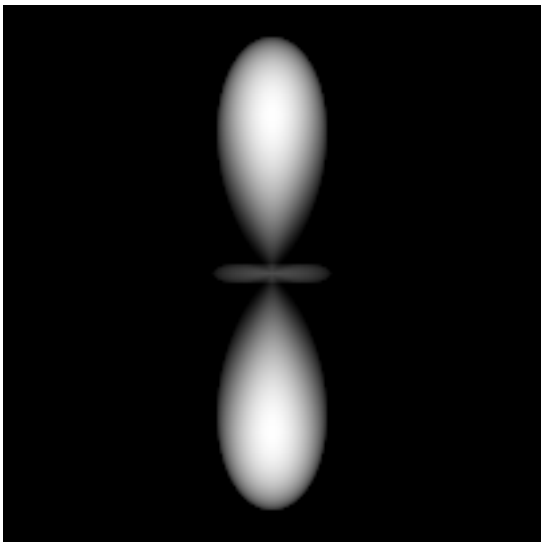

Figure 3.2.1. Projected image of the PAD for linear polarization, normalized to unity. Black corresponds to zero value and white to 1. The maximum value is found in the lobes.

In the image reconstruction process a specific type of mask is applied to enhance the comparison results with the corresponding analytical image. This mask is a disk with a radius equal to half the number of pixels, $\frac{N_{pixels}}{2}$,and is centered at the midpoint of the image. This radius was chosen to retain only the data of the reconstructed images contained within the circle of radius $r = \frac{N_{pixels}}{2}$ and thus ignoring the contribution from the background signal. This is related to the tomographic method. By rotating the PAD around the z-axis its maximum point r_{max} traces a circle on the z-plane which contains all possible rotations of its z-cross sections. The diameter of this circle corresponds to a line on the detector of length $2r_{max}$ which according to Section 3.1.2 is the total length of a detector row. Therefore, $r_{max} = \frac{N_{pixels}}{2}$. An additional advantage of applying the disk mask is that noise is added only to the projected data.

The disk mask is shown in Figure 3.2.2. for the reconstruction of the z=0 slice at 1% noise level using POP (a) and tomography (b).

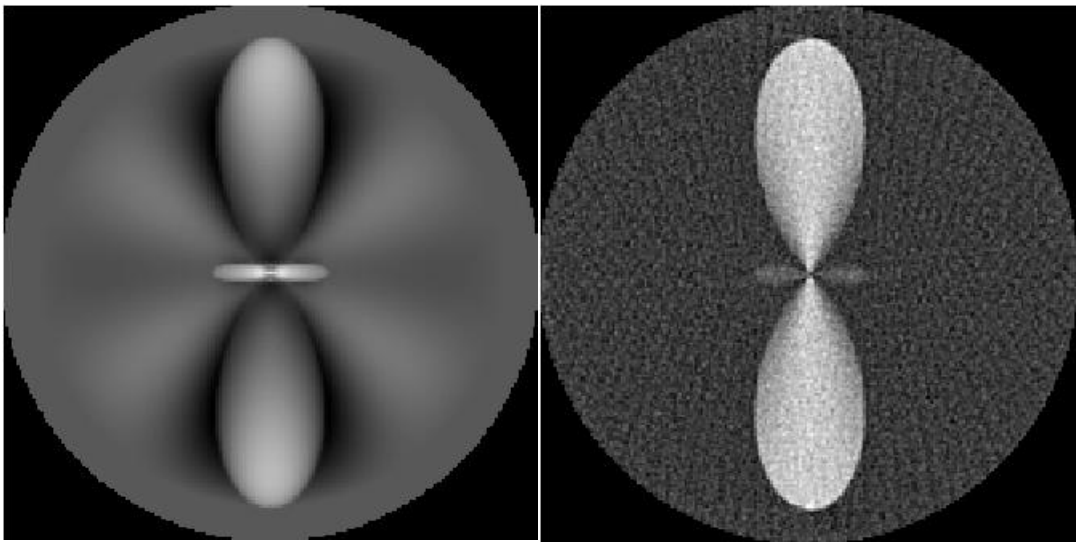

(a) (b)

Figure 3.2.2. Reconstruction of the central z=0 slice of the PAD at 1% noise using (a) the POP method, (b) the tomographic method for 70 projections.

3.3. 3D PAD reconstruction: Linear light polarization

The general 3D angular distribution where only the d-wave contributes (Equation A30) is transformed to a simpler expression when the light is linearly polarized.

$$J_r \propto \left| \frac{-\eta^2 e^{2i\delta} + f^2 + 2if\eta e^{i\delta}}{\sqrt{30}} Y_{2-2} + -\frac{\eta^2 e^{2i\delta} + f^2}{3\sqrt{5}} Y_{20} + \frac{-\eta^2 e^{2i\delta} + f^2 - 2if\eta e^{i\delta}}{\sqrt{30}} Y_{22} \right|^2$$

The polarization vector is given by the expression $\vec{\epsilon} = f\,\hat{x} + \eta\, e^{i\delta}\hat{y}$ and for linear polarization [43] along the x-axis we must set $f = 1$ and $\eta = 0$.

In Figure 3.3.1, Expression (A30) for linear polarization is graphed in polar coordinates and centered at the origin. This is the 3D distribution we are going to reconstruct using Polar Onion Peeling an Abel inversion method and tomography.

The coordinate system shown in Figure 3.3.1 is in accordance with the convention of Figure 3.1.2 and the requirement mentioned above in Section 3.1.1. Thus, the 3D object is cylindrically symmetric around the x-axis. The integration is along the y-axis and the detector will be parallel to the (x, z) plane, at a distance L from the y=0 plane.

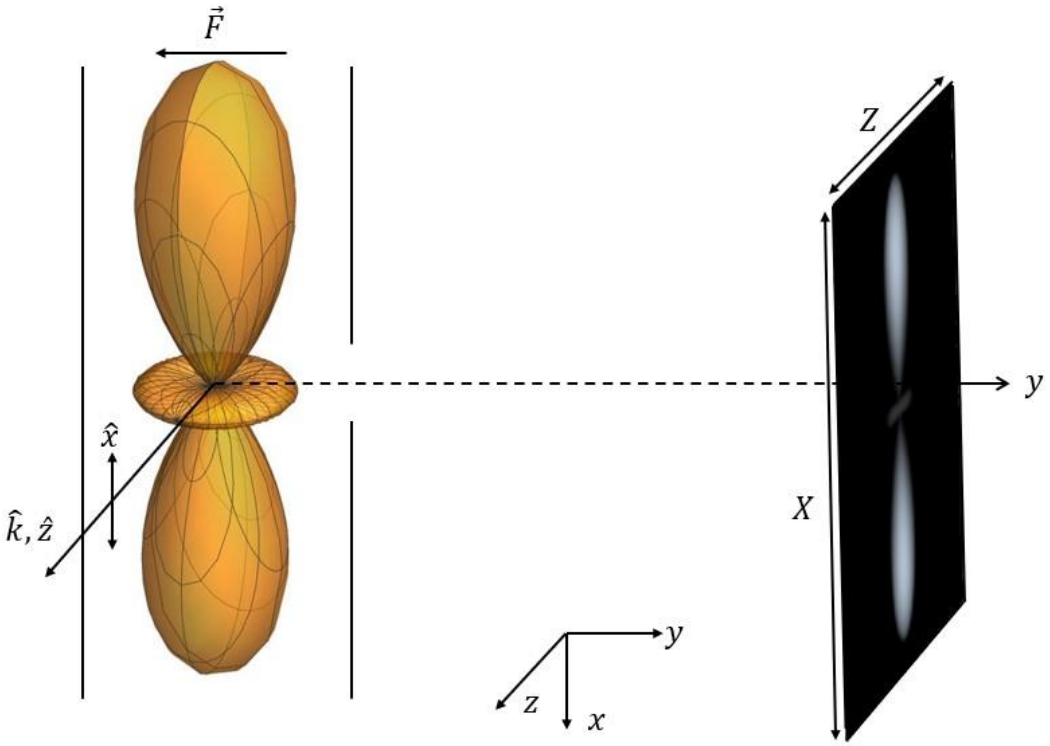

Figure 3.3.1. The PAD for linear polarization is displayed in polar coordinates. The CCD detector is shown on the left side and the propagation axis with a vector.

3.3.1 Abel Inversion (Polar Onion Peeling) of the projected image and its assessment

We are going to use the discretized projection of the PAD, $B_i(x_i, z_i)$, as an image and apply the Abel inversion method, specifically the Polar Onion Peeling method, to reconstruct the initial PAD. This is accomplished with a Mathematica program already developed by Mr. Sotiris Danakas, which is currently in use in our department. Feeding the data matrix of the function $B_i(x_i, z_i)$ as an image to this program the Abel inversed initial distribution is produced.

Only the central y=0 slice of the initial distribution is produced, which is nonetheless sufficient to reconstruct the 3D PAD by rotating this slice around the x-axis. This is possible due to the cylindrical symmetry of the distribution

Now we will evaluate the accuracy of the POP method in producing a credible reconstruction of the 3D PAD. This is achieved by comparing it to the initial theoretical distribution. As mentioned, the POP method produces the y=0 slice of the distribution. Therefore, we will calculate the y=0 slice of the initial distribution using the analytical Cartesian function $A'(x, y, z)_{linear}$. This function is $A'(x, 0, z)_{linear}$, which is then discretized, creating a 2D data matrix of dimensions 201x201. This data matrix is also normalized to unity so that comparison with other matrices will be valid.

The comparison between the y=0 of the 3D distribution obtained by the POP method and the analytical function $A'(x,0,z)_{linear}$ is achieved by introducing the error function

$$E = \sum_i (x_{1,i} - x_{2,i})^2 \tag{3.5}$$

Where, in this case, $x_{1,i}$ are the data matrix values of the function $A'(x,0,z)_{linear}$, whereas $x_{2,i}$ are the data matrix values of the y=0 slice of the PAD obtained by the POP method. The use of the error function in Expression (3.5), involves subtracting the corresponding points of the matrices from each other and squaring the result $(x_{i,j,Image1} - x_{i,j,Image2})^2$, where i is the row and j is the column. The sum of squares of the subtractions for each point of the 201x201 matrices of the images is calculated to be 5081, which is the error for the POP method.

The retrieval of the 3D PAD by reconstructing the central slice (z=0) applies to symmetric distributions, where both POP and tomography methods can be compared using the 2D error, because only a single 2D slice of the distribution is assessed, the central slice. If the full 3D symmetric distribution were reconstructed, a different error function would be required for its assessment, the 3D error function. In the case of non-symmetric distributions there is no central slice, so only the 3D error can be calculated. This scenario of 3D volume error will be addressed later in the tomographic reconstruction of multiple slices of symmetric and non-symmetric distributions.

3.3.2 Tomographic method of the projected image and its assessment

In this section, similarly to the previous one, we will reconstruct the PAD using the tomographic method described in the Theory. Generally, a 3D object can be tomographically reconstructed by considering it as a finite stack of 2D cross sections with each cross section treated separately. The cross sections should be perpendicular to the polarization axis (z-axis); therefore z-slices will be reconstructed, parallel to the (x,y) plane. Due to the cylindrical symmetry of the PAD, the POP method reconstructed the central y=0 slice. For the comparison of the two methods to be valid the same slice of the 3D object should be reconstructed by tomography. This issue is easily resolved by acknowledging that the y=0 slice obtained by POP and the z=0 slice obtained by tomography are identical due to the cylindrical symmetry around the x-axis of the 3D distribution. Thus, we will proceed with the reconstruction of the z=0 slice, which will then be compared to the y=0 slice obtained by the function $A'(x,0,z)_{linear}$ as was done with the POP method.

The z=0 slice will be reconstructed using a specific set of projection numbers (angular sampling), $N_{projections} = 10,14,15,18,19,20,23,26,30,35,40,50,55,60,65,70,80$ and 90. The purpose

of this is to determine the number of projections needed to match the accuracy of the POP method in reconstructing the 2D slice of the object.

Consider a slice of the PAD, specifically the z=0 slice, projected onto the detector. The number of points evaluated on the pixels constitutes the spatial sampling. In our analysis, the number of points is fixed at 201. The spatial sampling is shown in Figure 3.1.6.

Fixing the spatial sampling while varying the angular sampling allows us to examine the relationship between the accuracy of the number of projection angles and the accuracy of the reconstruction.

Now we will describe the tomographic method on the z=0 slice of the PAD by first expressing it in Cartesian coordinates as $A'(x,y,0)_{linear}$. For each number of projections $N_{projections}$, the z=0 slice is rotated by an increment $\theta = \frac{180^\circ}{N_{projections}}$. Furthermore, for each rotation ,the rotated function $A'(x(\theta),y(\theta),0)_{linear}$,is integrated with respect to y, with the limits of integration being $(-r_{max}, r_{max})$. This is because by rotating the slice around the z-axis its maximum point traces a circle with radius equal to that point. This circle can be seen in Figure 3.1.5, which is enclosed by a square with length equal to the circle's diameter. Every possible rotation of the slice on the (x, y) plane should fit within that square. Thus, the integration of the rotated function $A'(x(\theta),y(\theta),0)_{linear}$ at points given by Equation (3.3) is mapped to the corresponding pixel centers of the CCD. For each projection number $N_{projections}$ and for each projection angle at a given projection number, 201 data point values are collected. As a result,18 matrices are assembled each with dimensions: $(N_{projections} \times 201)$.

Appropriately modifying these matrices will result in a sinogram corresponding to a specific projection number.

The sinogram, as introduced in the Theory, is a matrix assembled such that each projection of a given projection number forms a column, arranged in ascending order of rotation angles. So, the sinogram has as many columns as the projections recorded with the detector, where each projection represents one angle of rotation.

The number of sinogram rows must equal the length of the diagonal of the square image, which has a side length of N_{pixels}. The diagonal is the maximum possible length a projection line can have in a rotation of the image. To ensure all points in an image contribute at all projection angles, the length of the projection line increases to span the diagonal of the image (the extra cyan line on each side of the CCD line), as shown in Figure 3.3.2.

Therefore, the diagonal parameter, is defined as

$$diag = N_{pixels}\sqrt{2} = 284 \tag{3.6}$$

where $N_{pixels} = 201$ is the number of pixels on the CCD screen. The dimensions of a matrix sinogram are:$(diag \times N_{projections})$.

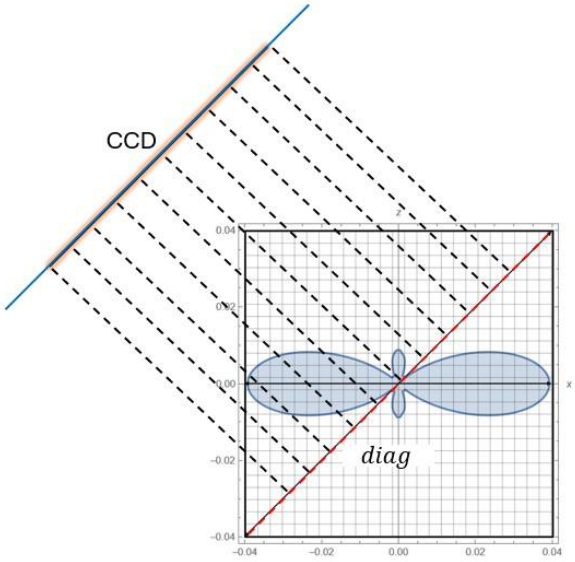

Figure 3.3.2 The length of the projection line (red blurry CCD line) is equal to the side length of the $N_{pixels} \times N_{pixels}$ square while the cyan line equals the length of the diagonal of the matrix.

The 18 data matrices produced in the previous Section have dimensions $(N_{projections}, 201)$. The rows are equal to $N_{projections}$, and the columns are 201. There are two steps to convert the 18 data matrices into 18 sinograms. The first step is to transpose the matrices by switching the rows and columns. As a result, the dimensions of the matrices will be $(201, N_{projections})$, The second step, is for the rows to be equal to the diagonal $diag = 284$. Rows padded with zero values should be added to the matrices (extra cyan lines in Figure 3.3.2). Therefore, on top and below the data matrix, an N_{rows} number of rows should be added,

$$N_{rows} = \frac{|diag - N_{pixels}|}{2} \tag{3.7}$$

With the completion of these two steps, the 18 data matrices have the appropriate dimensions: $(diag, N_{projections})$ and can be considered sinograms.

Applying this process to the 18 matrices we get 18 sinograms. Some indicative examples of the sinograms are shown in Figure 3.3.3 for number of projections $N_{projections}$=40 and 70

The sinograms are derived from the corresponding matrices, which are normalized to unity. Thus, in their depiction as images, black represents zero value and white represents one, as usual. The

dimensions of the sinograms for different projection numbers are illustrated in Figure 3.3.3 For 40 projections the dimensions are (285, 40) as seen in the narrower sinogram of Figure 3.3.3(a). In contrast, with 70 projections and sinogram dimensions of (285, 70) the sinogram shown in Figure 3.3.3(b) appears wider. Both sinograms have the same height because they share the same number of rows, 285

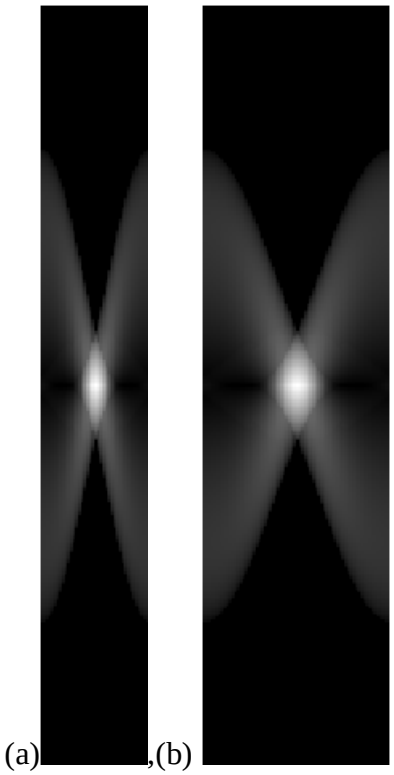

(a),(b)

Figure 3.3.3. Sinograms corresponding to number of projections, (a) $N_{projections}$=40, (b) $N_{projections}$=70

The sinograms are inverted using a built-in function in the Mathematica environment, which employs the Filtered Backprojection method.

The inversion function in Mathematica allows the selection of the number of pixels in the final image. The selectin of the number of pixels is convenient since each sinogram image has a different dimension. Thus, we select the final image to have dimensions 201x201, equal to the dimensions of the y=0 slice of the PAD, produced by the analytical function $A'(x,0,z)_{linear}$ and by the POP method. This way all of their matrixes have the same dimension, and their comparison is possible

In Figure 3.3.4, the reconstructed z=0 slices are presented for the number of projections $N_{projections}$=10 and 20. In Figure 3.3.4(a) for 10 projections there are unwanted artifacts, such as lines, and overall inaccurate results, as discussed in the Theory, due to insufficient angular sampling. Increasing the number of projections lessens the effect of these artifacts, specifically lines originating

from filtered back projection, and reconstructs the z=0 slice more clearly and accurately, as shown in Figure 3.3.4 (b) for 70 projections.

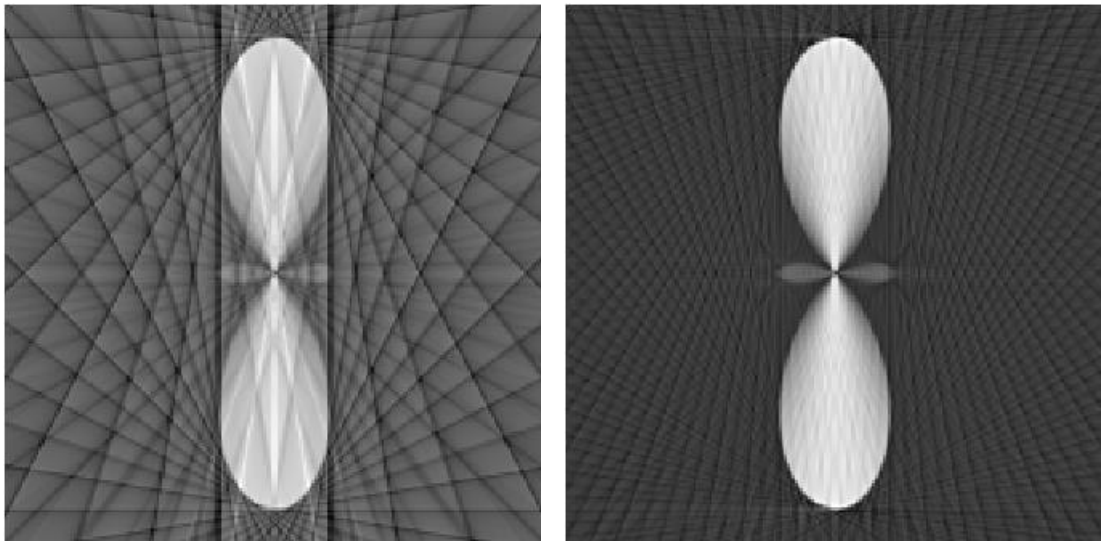

(a) (b)

Figure 3.3.4. Inverted images of the sinograms corresponding to number of projections, (a) $N_{projections}$=20, (b) $N_{projections}$=70,

To evaluate the tomographic method in reconstructing the z=0 slice of the PAD we compare the inverted images obtained by tomography to the theoretical z=0 slice obtained by the function $A'(x,0,z)_{linear}$. The comparison is carried out with the use of the error function defined in Equation (3.5), where, similar to the POP method, the two images are compared pixel by pixel. The errors,$E_{Theoretical-Tomography}$,between tomography-reconstructed slices and the theoretical initial slice for each number of projections, $N_{projections}$, are plotted with respect to the projection number, as shown in Figure 3.3.5. Generally, the error values decrease as the number of projections increases although fluctuations are observed across all projections.

Approximately, for 19 projections tomography matches the error and thus the accuracy of the POP method. There are some observations that should be noted. First, the tomography error matches the POP error for 14 projections as well. However, due to the small number of projections, or angular sampling, tomography is inaccurate, and the result cannot be trusted. Second, the error of tomography generally decreases with great increase in the number of projections, resulting in a much larger difference from the POP error. Lastly, as mentioned before, the error fluctuations remain throughout the plot even for large projection numbers.

The comparison between the POP and the tomographic method is also carried out in the presence of background noise with the method described in Section 3.2.1. The noise levels as mentioned are 1% and 5%.

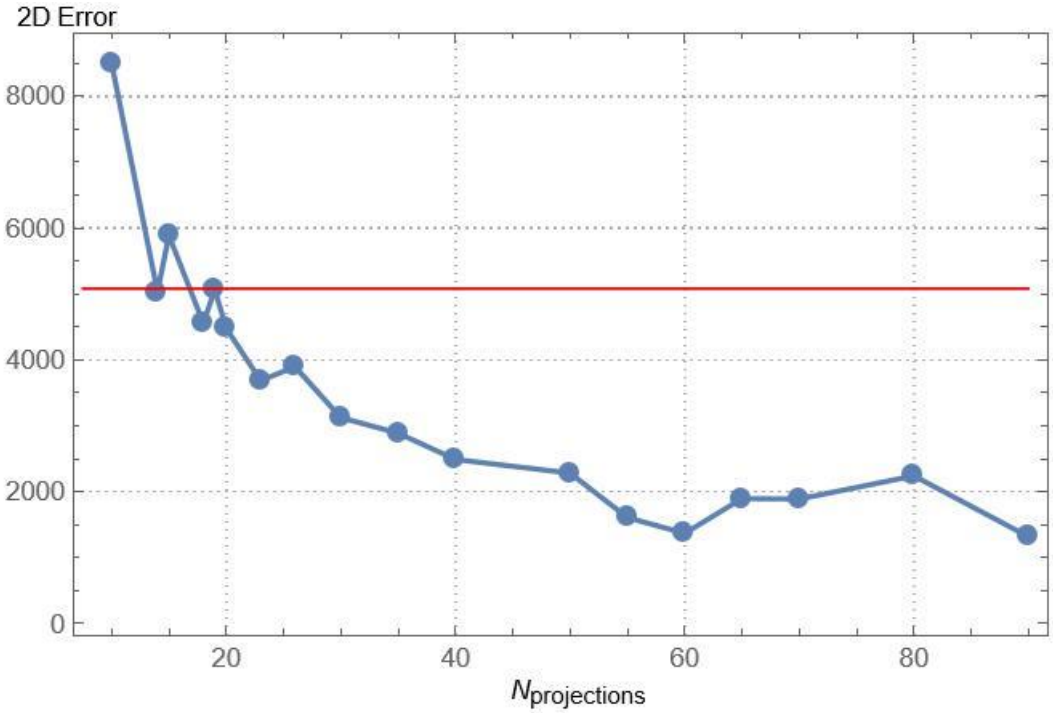

Figure 3.3.5. Graph depicting the errors between tomography and analytically obtained slice in relation to the number of projections. The red line depicts the POP error.

The methodology of reconstructing the y=0 slice of the 3D distribution with the POP method in the presence of noise remains similar to that without noise. The distinction is that the final matrix includes the noise matrix and the comparison with y=0 slice obtained by the function $A'(x,0,z)_{linear}$ is performed using an appropriate mask. The results of the comparison between the POP-reconstructed noisy y=0 slice and the noiseless analytical y=0 slice of the initial PAD is 4155 for 1% and 4305 for 5% noise level.

The first observation is that as the noise increases, the error increases, which is expected behavior. The second observation is that both errors are smaller than the error without noise, (5081.04) ,which is counter intuitive. The reason for this is that the noiseless POP error was calculated without adding the mask. Thus, the whole image contributes to the error making it larger than the errors with noise. Adding the mask to the POP-reconstructed noiseless y=0 slice of the PAD would result in an error of 4102.49, which is smaller than both POP noise errors.

The reconstructed y=0 slice of the PAD at 5% noise level using POP is shown in Figure 3.3.6(a).

Now, the tomographic method will be tested in the presence of noise and compared with the POP method. Similar to the noise-free distribution, the tomographic reconstruction of the noisy z=0

slice is performed by adding the noise matrix to the data matrix, converting them into sinograms and then inverting them to produce the reconstructed slice. The number of projections remains 10,14,15,18,19,20,23,26,30,35,40,50,55,60,65,70,80 and 90 for 1% noise level but we increase it to 10,14,15,18,19,20,23,26,30,35,40,50,55,60,65,70,80,90,100,110,120,130,140,150 and 160 for 5% noise level to match the corresponding POP error. For each data matrix, two noisy data matrices are generated corresponding to 1% and 5% noise levels, resulting in twice as many reconstructed slices. In the inverted images, a mask has been applied, which improves the comparison between the tomographically reconstructed slices and the analytically obtained z=0 slice.

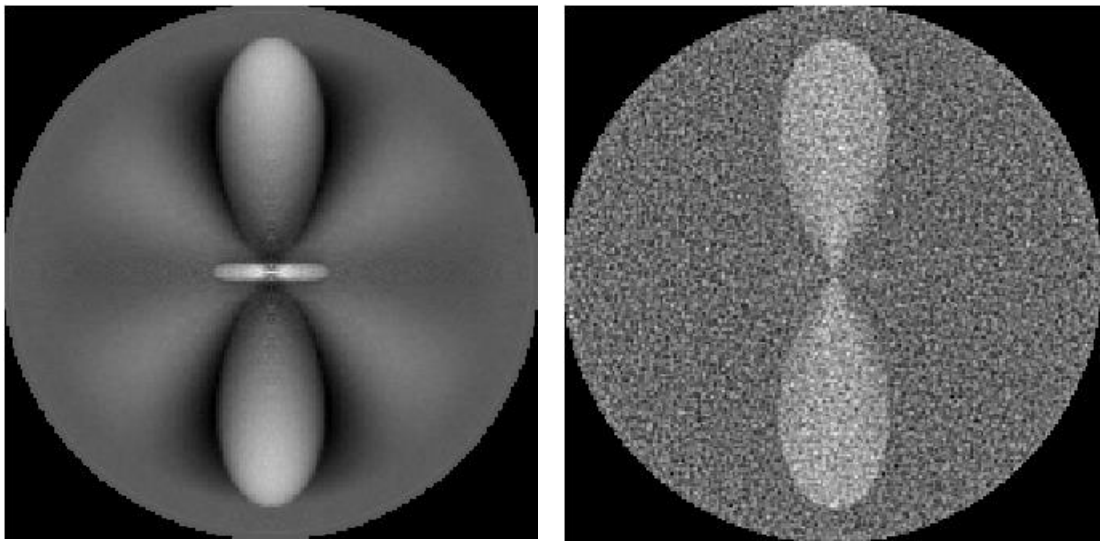

(a) (b)

Figure 3.3.6. Reconstruction of the z=0 slice at 5% noise levels using (a) the POP method and (b) tomography with 70 projections.

Figure 3.3.6(b) shows the tomographically reconstructed z=0 slice with 70 projections at a 5% noise level. This slice appears grainy making its details less clear and harder to discern.

In contrast, the Abel-inverted slice is much clearer at the same noise level. The comparison results between the tomographically reconstructed noisy z=0 slices and the noise-free analytic slice obtained from the function $A'(x,0,z)_{linear}$ are plotted against the number of projections for both noise levels, as shown in Figure 3.3.7.

For 1% noise, the number of projections needed for tomography to match the accuracy of the POP method is approximately 20-22 projections, slightly more than the noiseless case. For 5% noise, at least 140 projections are needed for tomography and POP to yield the same error.

This is a significant difference compared to the noiseless and the 1% noise cases, where only around 20 projections are needed.

This highlights the efficacy of the POP method in dealing with noisy data as well as the adaptability of tomography to match the POP method simply by increasing the number of projections.

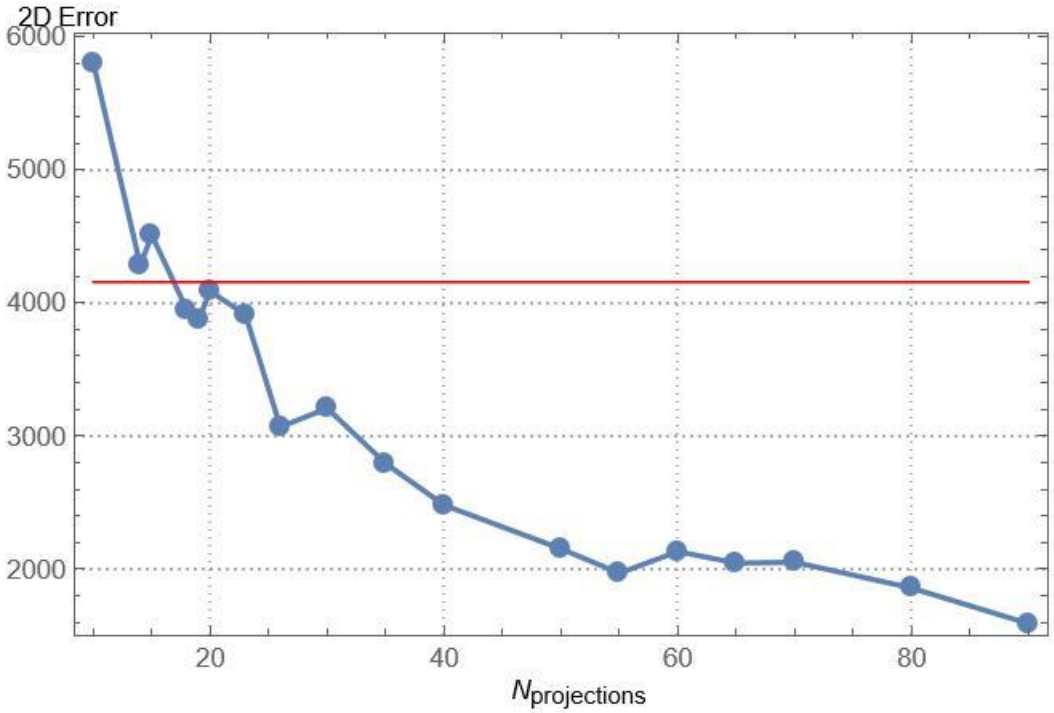

(a)

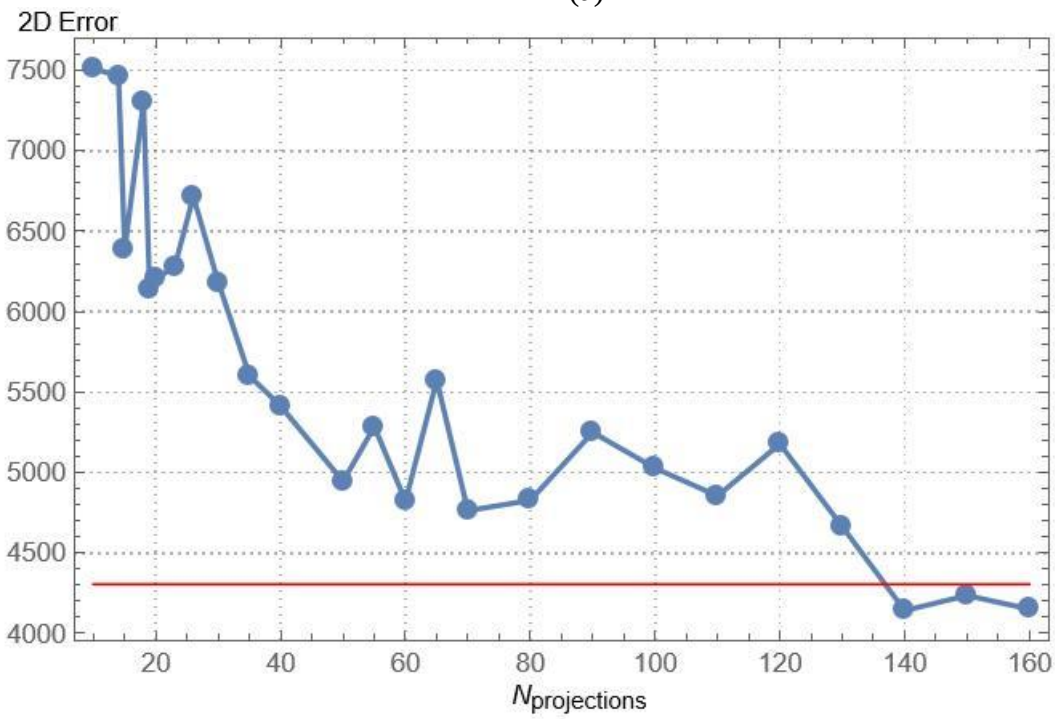

(b)

Figure 3.3.7, Graph of the errors in relation to the number of projections, comparing tomography and the theoretical z=0 slice in the presence of noise :(a) 1% noise and (b) 5% noise. The red line depicts the error between the POP method and the theoretical y=0 slice.

It should also be noted that both plots in Figure 3.3.7 exhibit fluctuations, especially the 5% noise level plot, which shows values higher than those at the 1% noise level. This indicates that tomography is less accurate at higher noise levels.

Now will be presented the full scope of the tomographic method which involves reconstructing multiple z-slices of the distribution, and then assembling these slices to recreate the original distribution. In this case, the assessment of the reconstruction will involve using the 3D error volume function, which accounts for the full distribution.

First, we will determine the z-cross sections of the PAD that will be tomographically reconstructed. The number of z-slices is not fixed in the program and thus, is selected by the user. Considering the symmetry of the distribution and the speed of the overall process five slices are deemed sufficient. This means that the z-region corresponding to the distribution will be divided into four equal segments. However, due to cylindrical symmetry, the PAD is symmetric around the z=0 plane, as shown in Figure 3.3.1, and so, only one of the z-subregions, either z>0 or z<0, needs to be divided. For our analysis the z<0 region is chosen. The slices begin from the maximum z point of the z<0 region , $-z_{max}$, which is a plane tangent to the distribution and end at the z=0 point, the midpoint of the z range $[-z_{max}\ , z_{max}]$. The cross section of the distribution with the z=0 plane as well as with other z-slices is shown in Figure 3.3.8(a). The method we will follow is the same as in the previous section for the z=0 slice, but instead of one slice now we have five slices. In Figure 3.3.8(b) the tomographically reconstructed 3D PAD is shown for 100 slices and 70 projections.

The tomographic process yields 18x5=90 matrices, where there are 18 sets of projection numbers and 5 cross sections. The dimensions of each matrix are $(N_{projections}, 201)$ and the number of projections remains the same as in the previous section for the noiseless z=0 slice. Using the data from the 90 matrices, we can construct the corresponding sinograms, which are then used to obtain the reconstructed slices.

Using the error function, Expression (3.5), the reconstructed z-slices are compared pixel by pixel with the analytical z-slices of the function $A'(x, 0, z_i)_{linear}$

For all the following plots, in both symmetric and non-symmetric distributions, a mask was applied to the reconstructed images in both the noisy and the noiseless data. In the noiseless case applying a mask, results in an almost vertical downward shift of the plot, with errors for fewer projection numbers decreasing slightly more than for larger projection numbers, while the overall shape of the plot remains unchanged. In the case of nose, using a mask is necessary to ensure that the noise affects only the projection data.

The plots of the 2D and the 3D errors are shown with respect to the number of projections in Figure 3.3.9 (a) and (b), respectively.

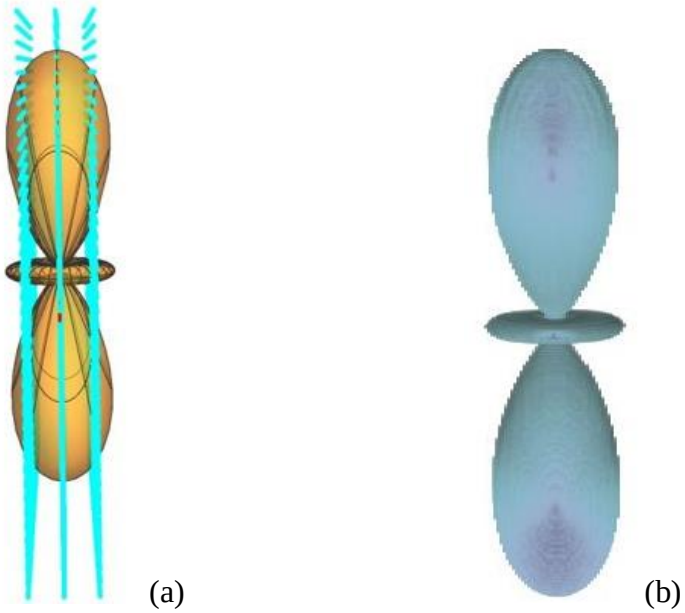

(a) (b)

Figure.3.3.8. The cross section between the z=0 slice and the initial PAD.

The plot of the 2D error is similar to the plot in Figure 3.3.5 for the z=0 slice, with the only significant difference being in the error values. In this case, less than 20 projections are needed for tomography to match the POP error, while nearly 19 projections are required without using the mask. Both the 3D and the 2D errors generally decrease with the number of projections, however the 3D error decreases in a smoother manner with seemingly less fluctuations. Both errors fluctuate across the plot for all projection numbers.

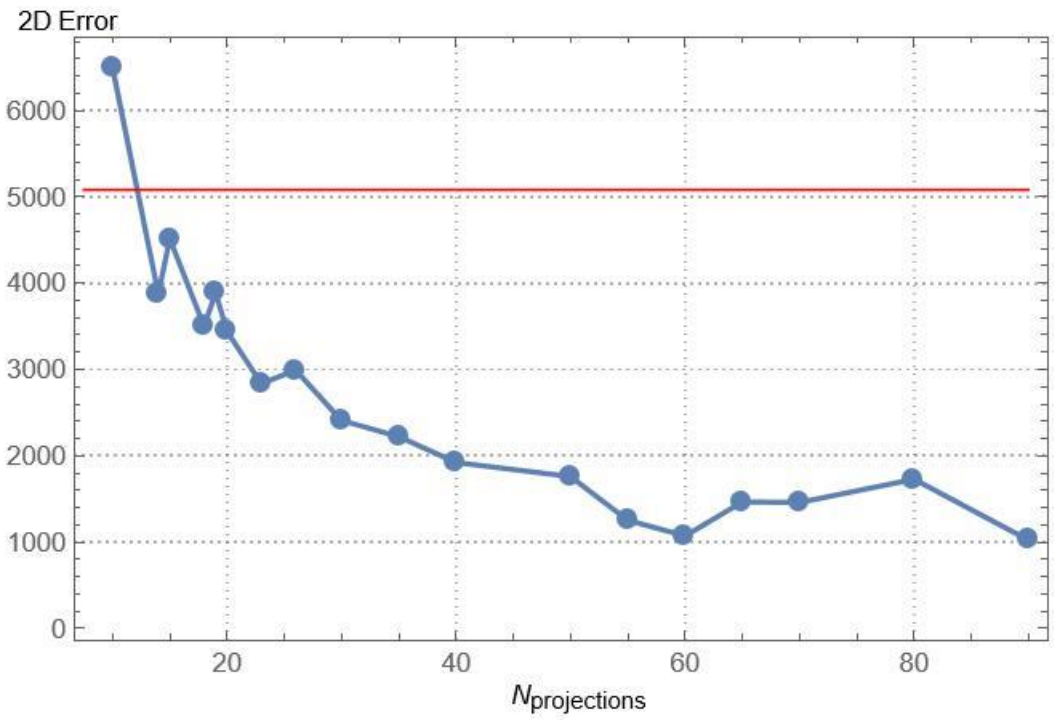

(a)

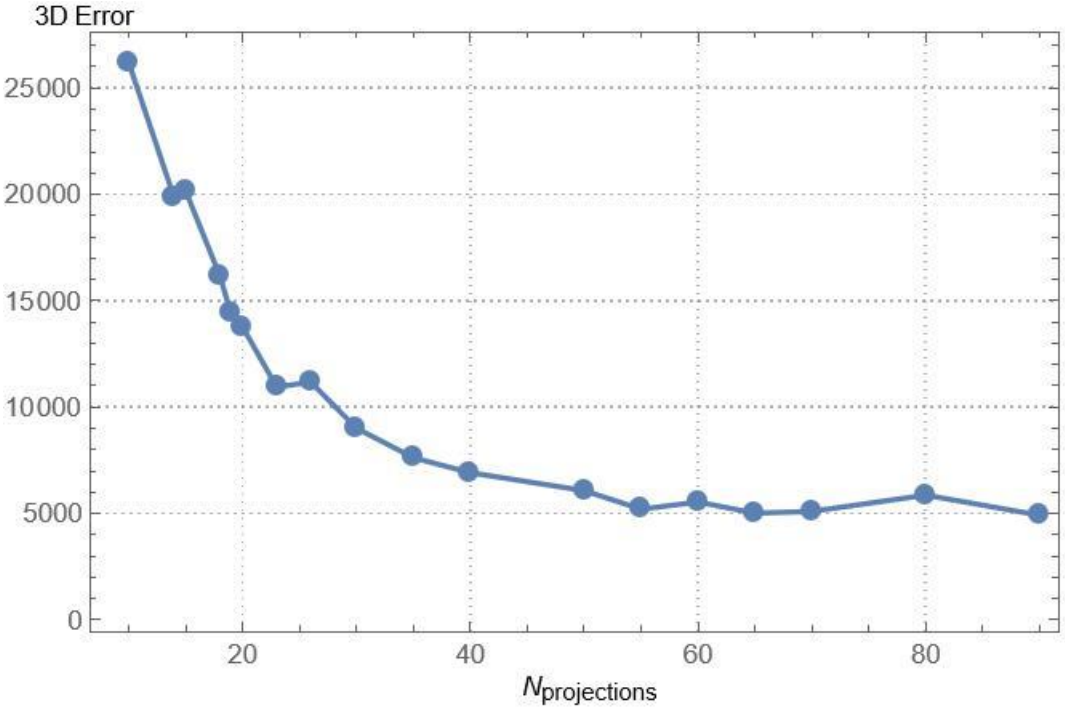

(b)

Figure 3.3.9(a)Plot of 2D Error in relation to the number of projections,(b) Plot of 3D Error in relation to the number of projections, both for noiseless data. The red line represents the POP error for the z=0 slice: 5081.

The 2D and 3D errors are also plotted against the number of projections in noisy conditions. These plots are shown in Figure 3.3.10 and 3.3.11 for 1% and 5% noise level, respectively.

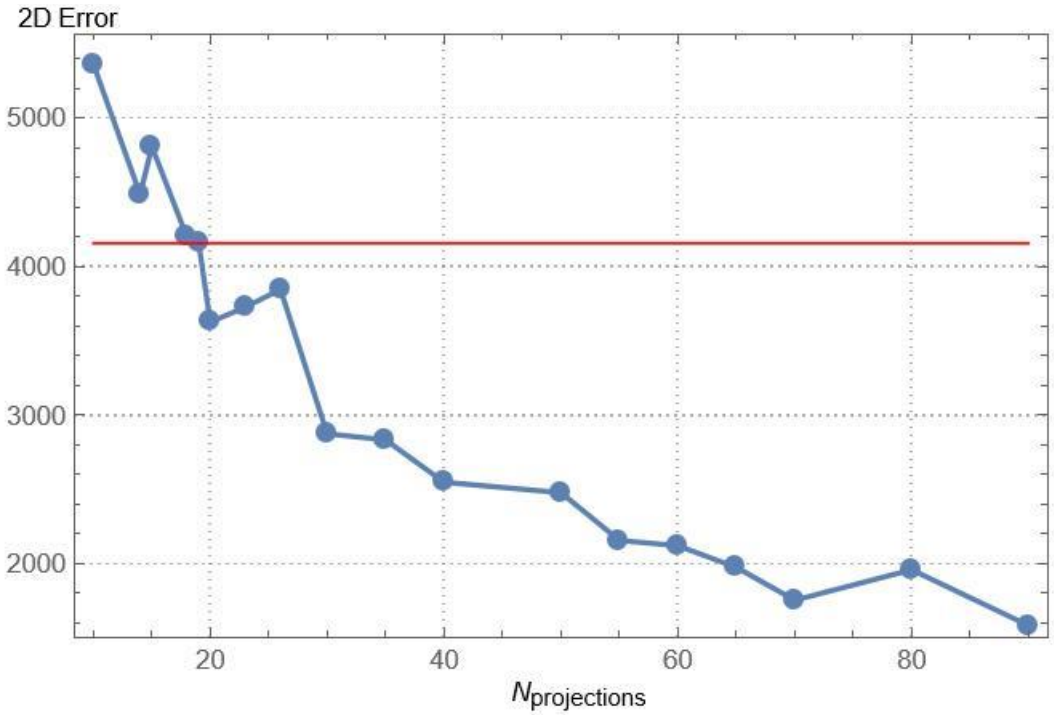

(a)

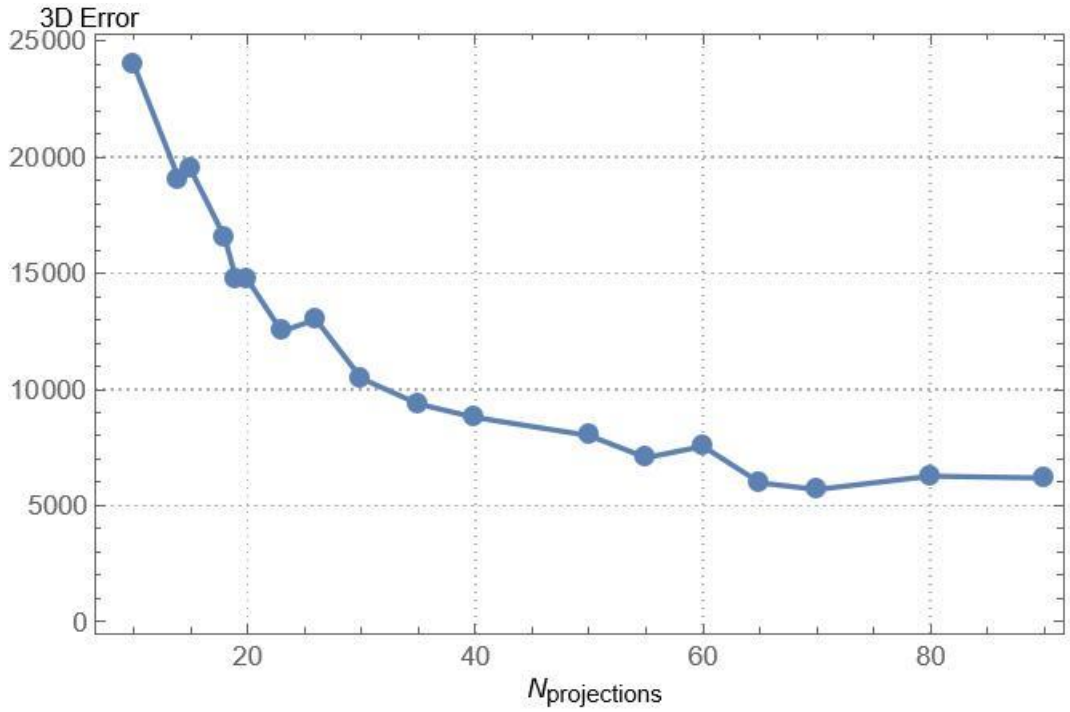

(b)

Figure 3.3.10. (a) Plot of 2D errors at 1% noise with respect to the number of projections. The red line represents the POP error for the z=0 slice: 4155 with the use of a mask. (b)Plot of 3D errors with respect to the number of projections

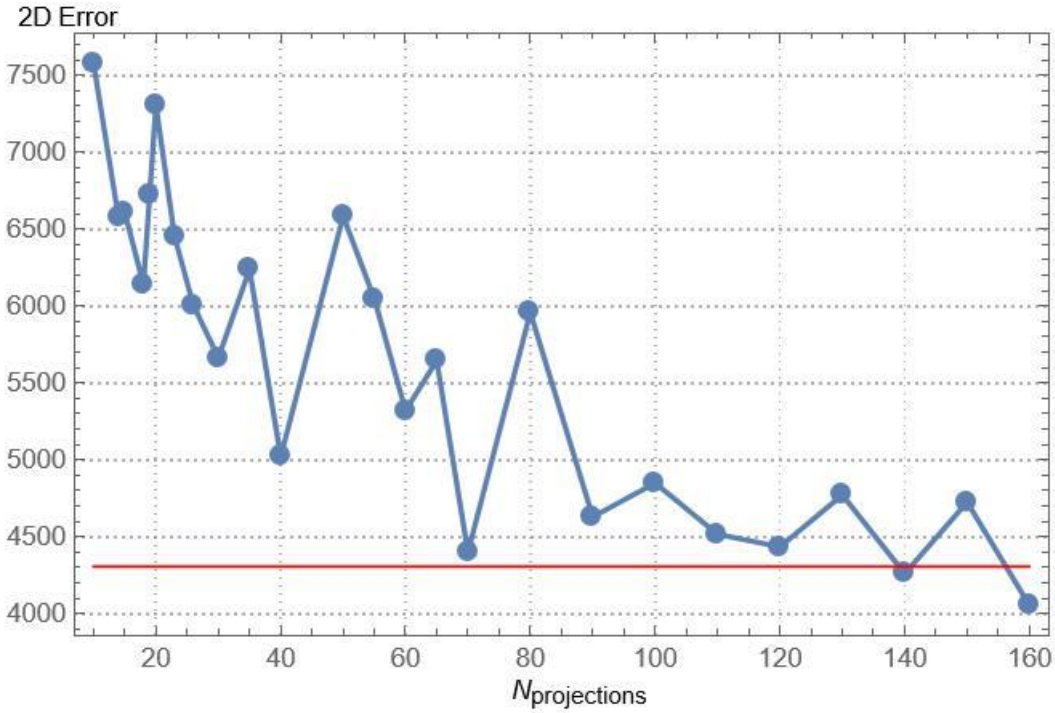

(a)

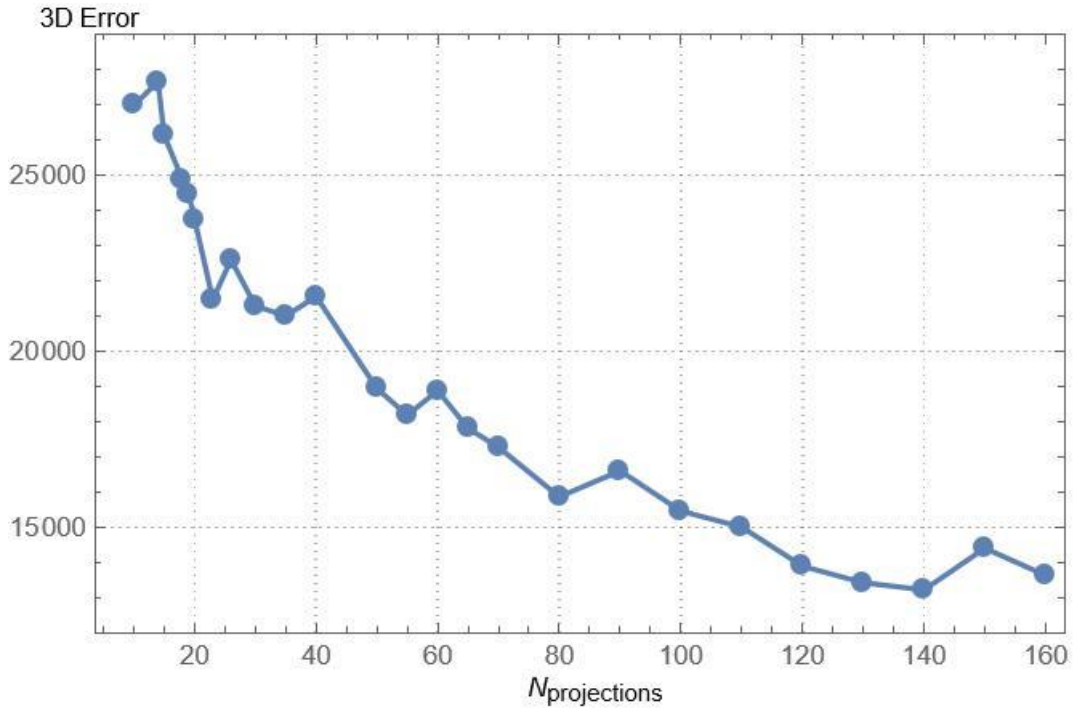

(b)

Figure 3.3.11 (a) Plot of 2D errors at 5% noise with respect to the number of projections where the red line represents the POP error for the z=0 slice: 4305.28 with the use of a mask. (b)Plot of 3D errors with respect to the number of projections.

The 2D errors at 1% noise (Figure 3.3.10a) generally fluctuate throughout the plot but decrease as the number of projections increases. In contrast, the 3D error plot at 1% noise (Figure 3.3.10b), follows a smoother line with fewer fluctuations. In Figure 3.3.11(a) at 5% noise level the 2D error plot is highly oscillatory for all projection numbers, while showing a decrease in value with the number of projections. At least 140 projections are needed for tomography to match the POP error. There is a significant discrepancy between the plot for 5% noise shown in this figure and Figure 3.3.7(b). This indicates a high sensitivity of the tomographic method to elevated background noise levels.

An attempt to reduce the oscillations caused by background noise involves lowering the cutoff frequency to smaller values. This leads to fewer fluctuations and smaller error values for both noise levels. However, the drawback is that the reconstructed images will display blurriness and a loss of detail (see Theory).

It is worth noting that lowering the cutoff frequency in the noiseless case does not reduce fluctuations in the 2D error plot but does lower the error values. However, the 3D error plot shows both a reduction in overall oscillations and a decrease in values.

Lastly, comparing the plots in Figures 3.3.9, 3.3.11 and 3.3.10 it is evident that the 2D and 3D errors are higher at 5% noise compared to 1% noise and the noiseless case, indicating that tomography produces more accurate results with lower background noise. This is further emphasized

by the increased number and intensity of fluctuations in 5% noise case compared to the 1% noise case.

3.4. Tomographic PAD Reconstruction: Elliptical light polarization – Symmetric Case

For elliptical polarization [43] the parameters in the general polarization vector are chosen to be $f = 1$, η=2 and $\delta = \frac{\pi}{2}$. Under these parameter values the 3D PAD (Equation A30) is analytically determined and is shown in Figure 3.4.1(a). It is evident the 3D PAD is no longer cylindrically symmetric around the x-axis. However, since it is a symmetric distribution, it will be tested to determine if the POP method can be applied for its reconstruction.

First, the distribution is integrated along the y-axis, with integration limits $[-y_{max}, y_{max}]$, resulting in its projection, as shown in Figure 3.4.2(b). Next, we apply the POP method to this projection image, producing the result shown in Figure 3.4.2(c). The POP method allows us to retrieve the y=0 slice of the original distribution, so we compare the output of the POP method with the y=0 slice of the PAD, shown in Figure 3.4.2(a). Comparing these two images shows that the POP inverted does not match the initial slice. This proves that the POP method is incompatible with elliptical light polarization and cannot reconstruct a distribution that does not to meet its requirements, even if the distribution is symmetric.

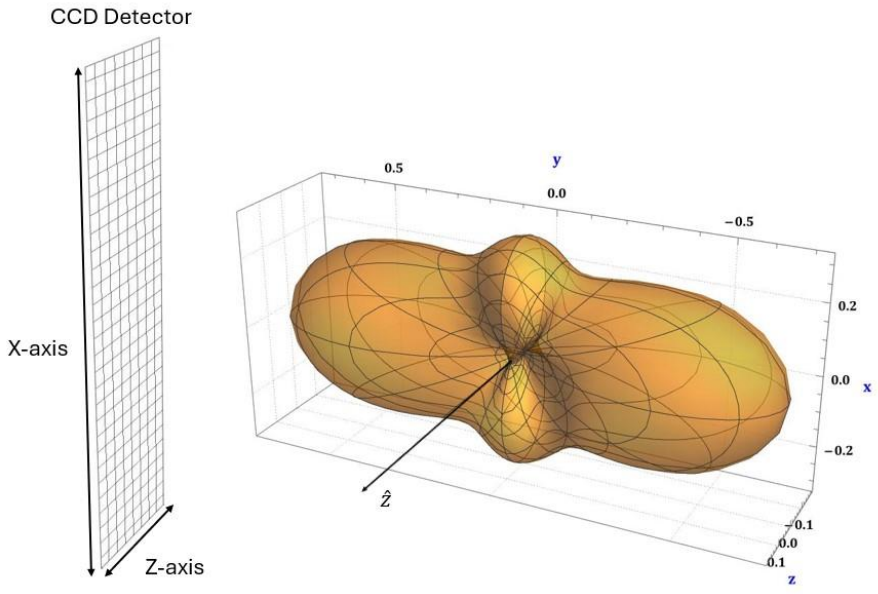

(a)

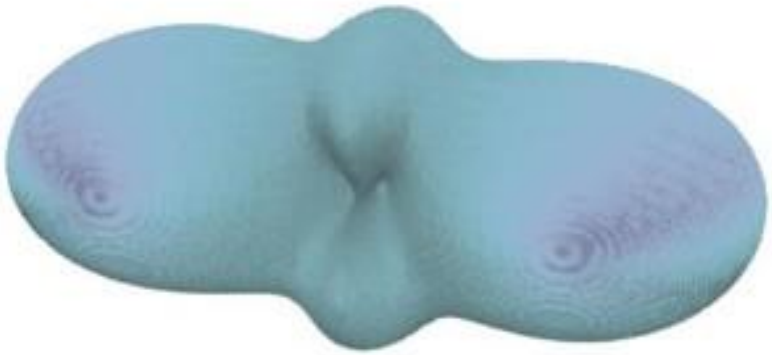

(b)

Figure 3.4.19.(a) Plot of the 3D PAD for elliptical polarization in polar coordinates from the analytical expression and (b) the tomographic reconstruction of the PAD.

Now that POP failed to reconstruct this PAD for elliptical light polarization it is time to employ the tomographic method. The assessment of the reconstructed images will be performed using the 3D error volume function. In Figure 3.4.3(a) the reconstruction of a z-slice of the PAD is shown for 70 projections and no background noise and in Figure 3.4.3(b) the same slice is reconstructed for 70 projections and 1% noise level. For both images a mask was applied. In Figure 3.4.1(b) the full 3D reconstruction is shown for 70 projections and 100 z-slices.

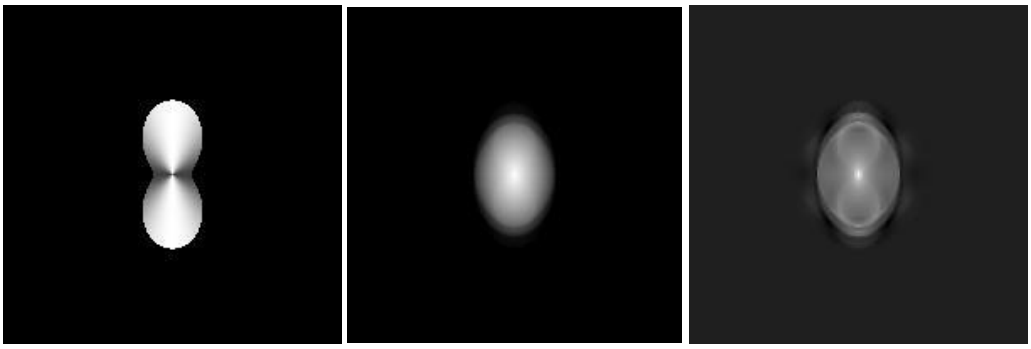

(a) (b) (c)

Figure 3.4.20. Shown (a) the initial slice y=0 slice of the PAD, (b) the projected image (c) the reconstructed y=0 slice

In Figure 3.4.4 the 3D error is plotted against the number of projections for noiseless data, while Figure 3.4.5 shows the 3D error plots at 1% (a) and 5% (b) noise levels. A disk mask is applied in all the reconstructed images both noisy and noiseless.

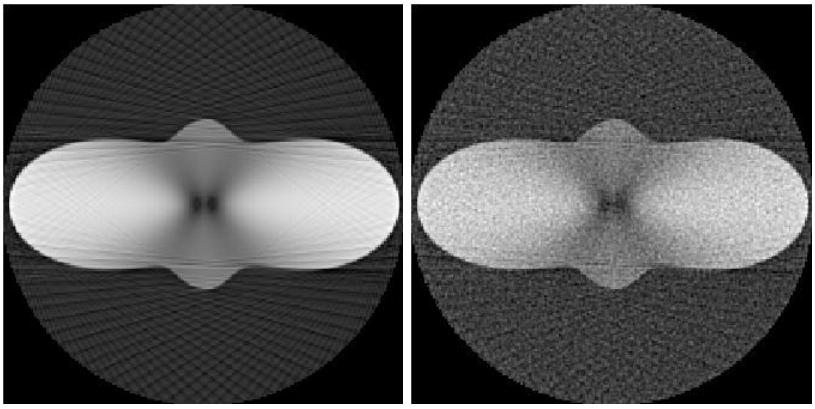

(a) (b)

Figure 3.4.3 Reconstruction of a z-slice of the PAD for 70 projections at (a) no background noise and (b) at 1% background noise.

The plot in Figure 3.4.4 generally follows a smooth trajectory with a few fluctuations that persist across all projections. The 3D error decreases rapidly with the number of projections, but it appears to stabilize at a constant value.

The 3D error plot for the 1% noise level shows similar characteristics as the noiseless case with a generally smooth curve that almost stabilizes at the final projections. In contrast, the 3D error plot at the 5% noise level is highly oscillatory across all projections.

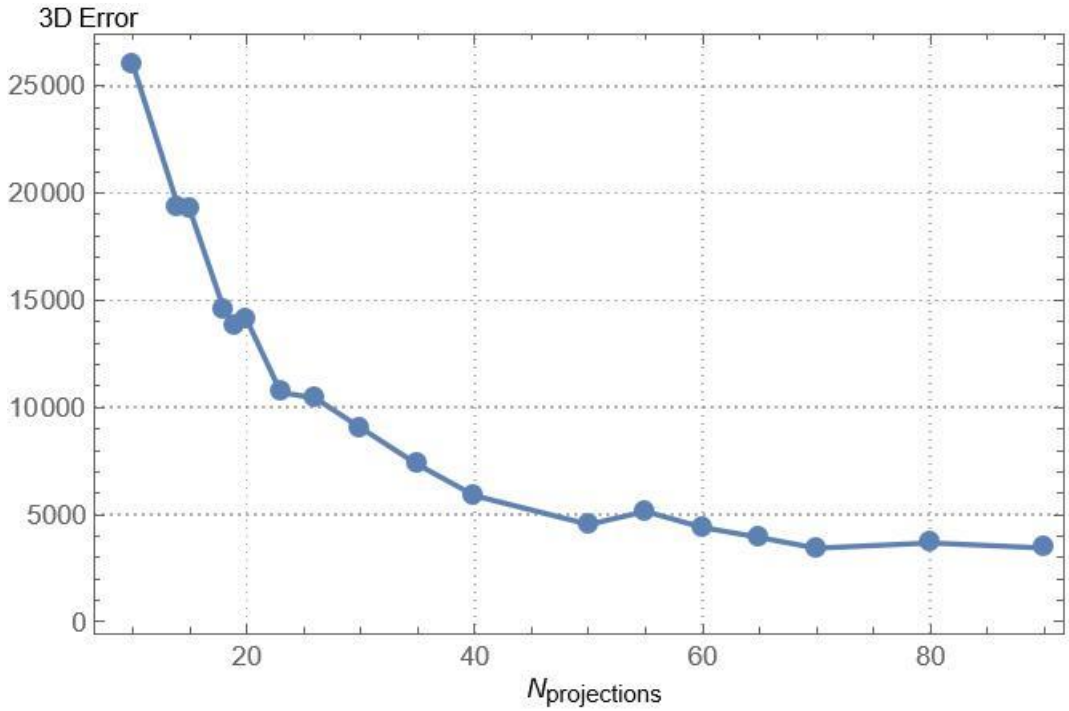

Figure 3.4.4. 3D error plot against the projection numbers for noiseless data in the elliptical case for symmetric distribution.

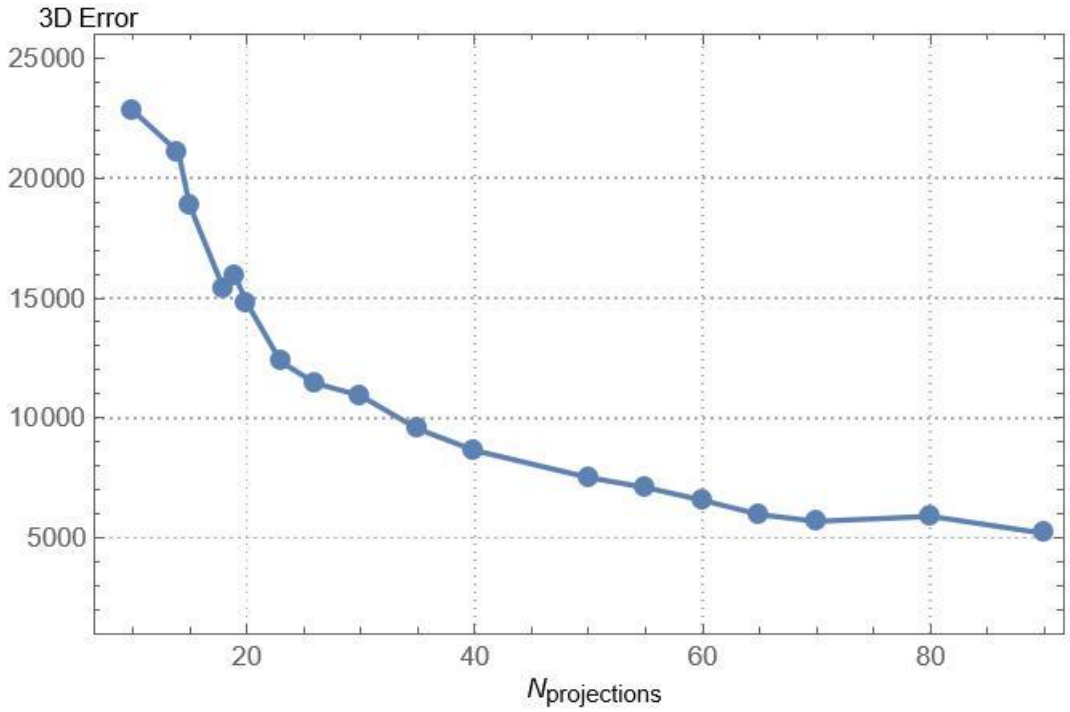

(a)

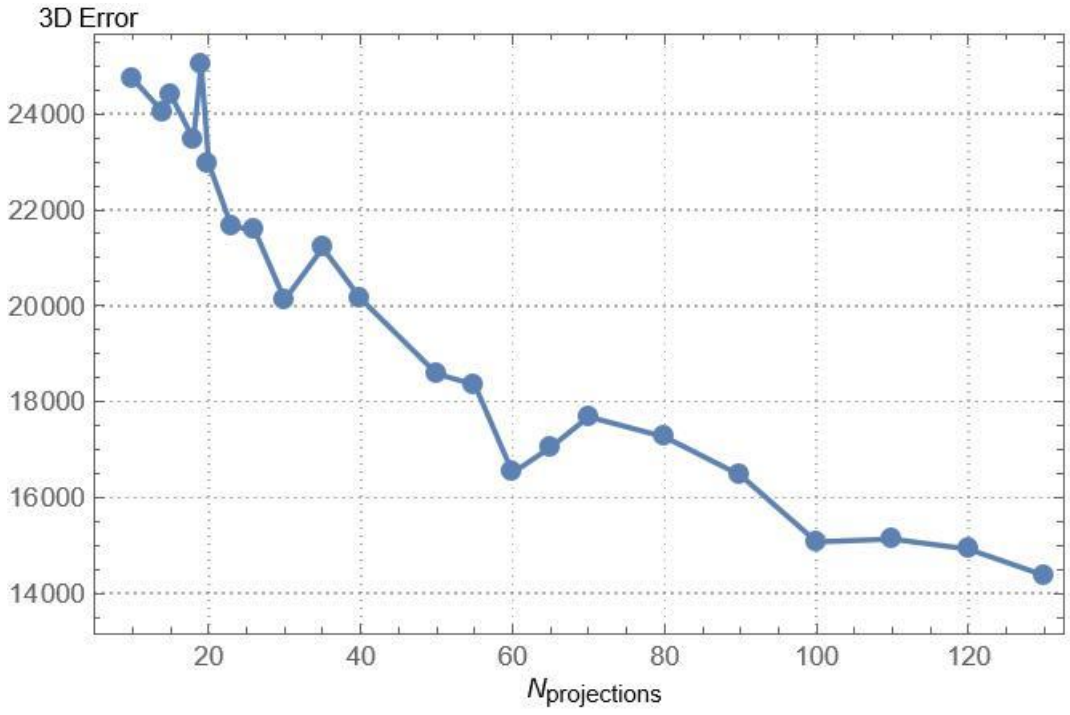

(b)

Figure 3.4.5 3D error plot against the projection numbers for (a) 1% noise level, (b) 5% noise level, in the elliptical case for symmetric distribution.

When comparing the 3D error values across all three noise levels it appears that they all start at approximately the same value. However, both the noiseless and 1% noise cases decrease to a similar value at 90 projections while the 5% noise case consistently shows higher values. Even at 130 projections the 3D error for the 5% case is three times greater than the other two cases. This indicates

that tomography is susceptible to high levels of noise but remains sufficiently accurate for lower background noise levels.

For both noisy and noiseless data, lowering the cutoff frequency of the filter reduces the fluctuations and lowers the error values, but the reconstructed images appear blurrier with less sharp edges.

A special case of elliptical polarization is circular polarization. A light is circularly polarized when it is composed of two plane waves of equal amplitude but with a phase difference of 90 degrees [43]. Therefore, the parameters of the polarization vector will be, $f = 1$, $\eta = 1$, and $\delta = \frac{\pi}{2}$. The 3D PAD distribution for circular polarization is shown in Figure 3.4.6.

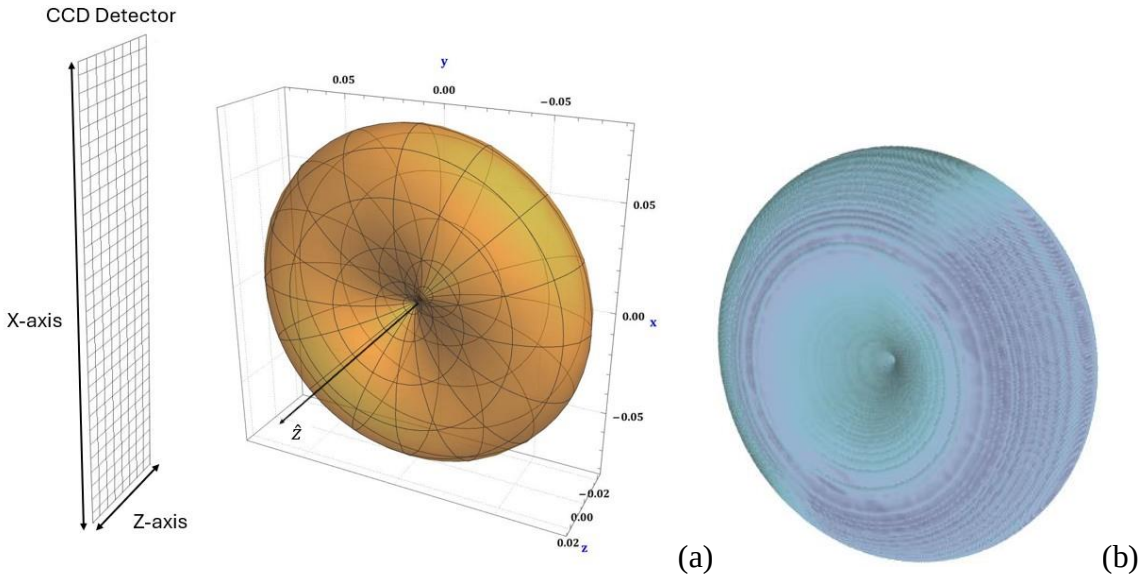

Figure 3.4.6 3D PAD distribution for circular polarization (a) from analytical expression and (b) from tomographic reconstruction.

Due to the relative simplicity of the distribution tomography yields results that outperform all other distributions examined in this project, indicating that the tomographic method is particularly effective when dealing with simpler distributions.

3.5 Tomographic PAD Reconstruction: Elliptical light polarization – Asymmetric Case

In this section we are dealing with a non-symmetric distribution produced by elliptical polarization with the same polarization parameters as in Section 3.4. This distribution is produced by

assigning a value of 1 to the Λ −parameter (Equation A28), resulting in the contribution of the term $Y_{00}(\theta, \varphi)$ in the distribution, Equation A27. An extra state is included to the expression of the distribution, $Y_{2-1}(\theta, \varphi)$, which is related to electric quadrupole transitions [44]. This distribution does not correspond to a realistic physical process and is included to assess the ability of tomography to reconstruct non-symmetric distributions. The PAD is shown in polar coordinates in Figure 3.5.1 (a). The tomographic reconstruction of this PAD is shown in Figure 3.5.1 (b) for 100 z-slices and 70 projections.

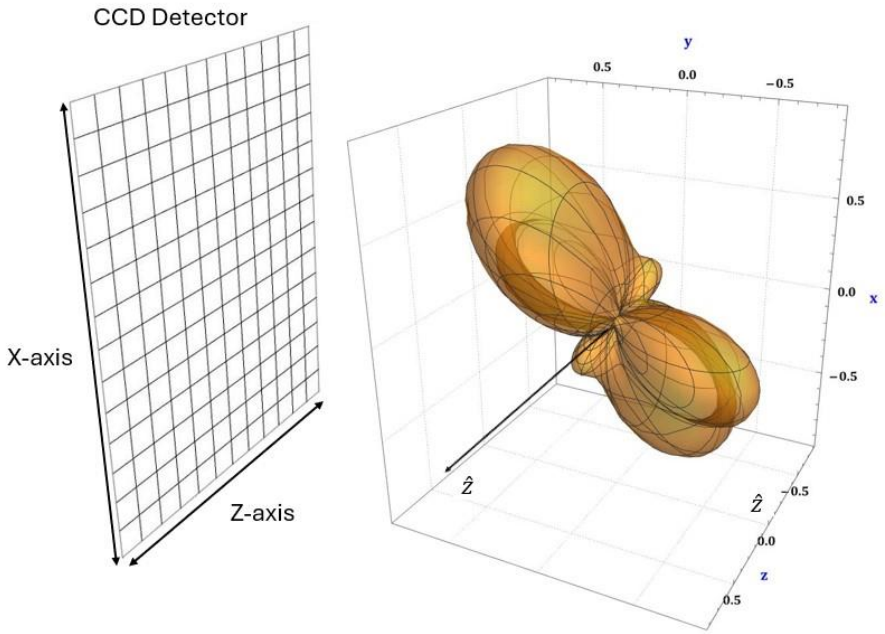

(a)

(b)

Figure 3.5.1 PAD of non-symmetric distribution for elliptical polarization (a) from the analytical expression and (b) from tomographic reconstruction.

We will use the tomographic method to reconstruct this distribution. The assessment of the reconstructed images will be performed using the 3D error function as the distribution lacks symmetry and has no central slice to examine. Consequently, the z-slices that will be reconstructed will span

the entire z-region starting from the maximum z-point on the negative axis and ending at the maximum z-point on the positive axis.

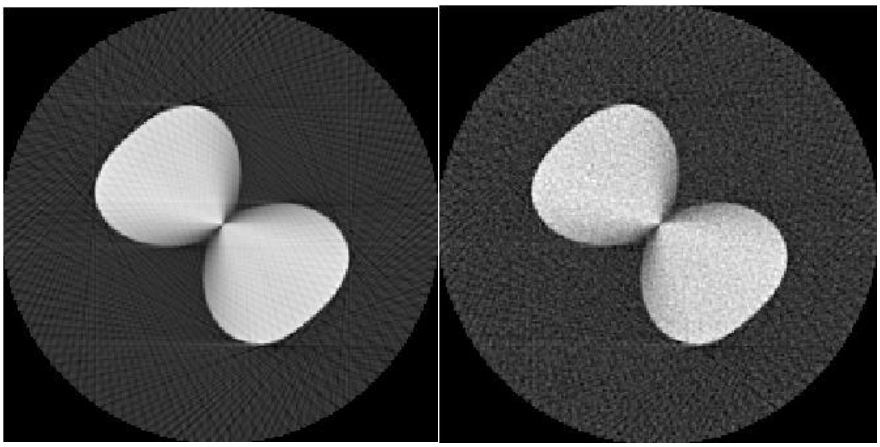

(a) (b)

Figure 3.5.2 Reconstructed z-slice for 70 projections at (a) zero background noise, (b) 1% background noise

In Figure 3.5.2 a reconstructed z-slice of the PAD is shown for 70 projections with no background noise (a) and at a 5% noise level (b).

In Figure 3.5.3 the 3D error values are plotted against the projection numbers for noiseless data. Figure 3.5.4 shows the 3D error plots for a 1% noise level (a) and a 5% noise level (b). A mask was applied to the generation of all the following plots.

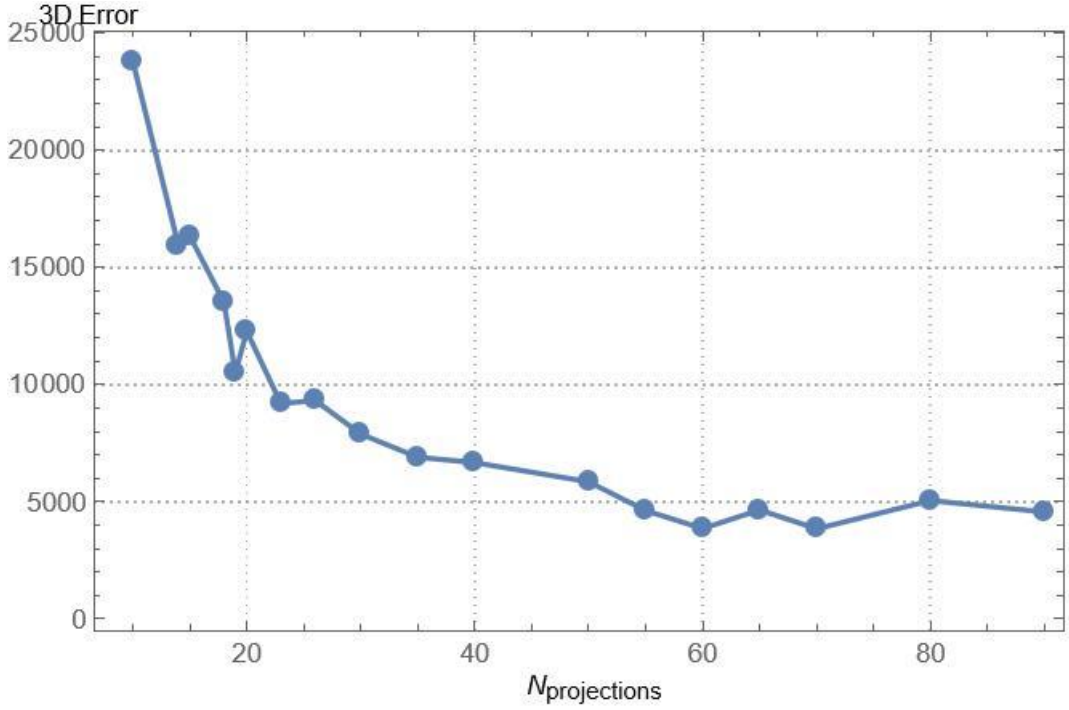

Figure 3.5.3 Plot of the 3D errors values for noiseless data in relation to the projection numbers for non-symmetric PAD.

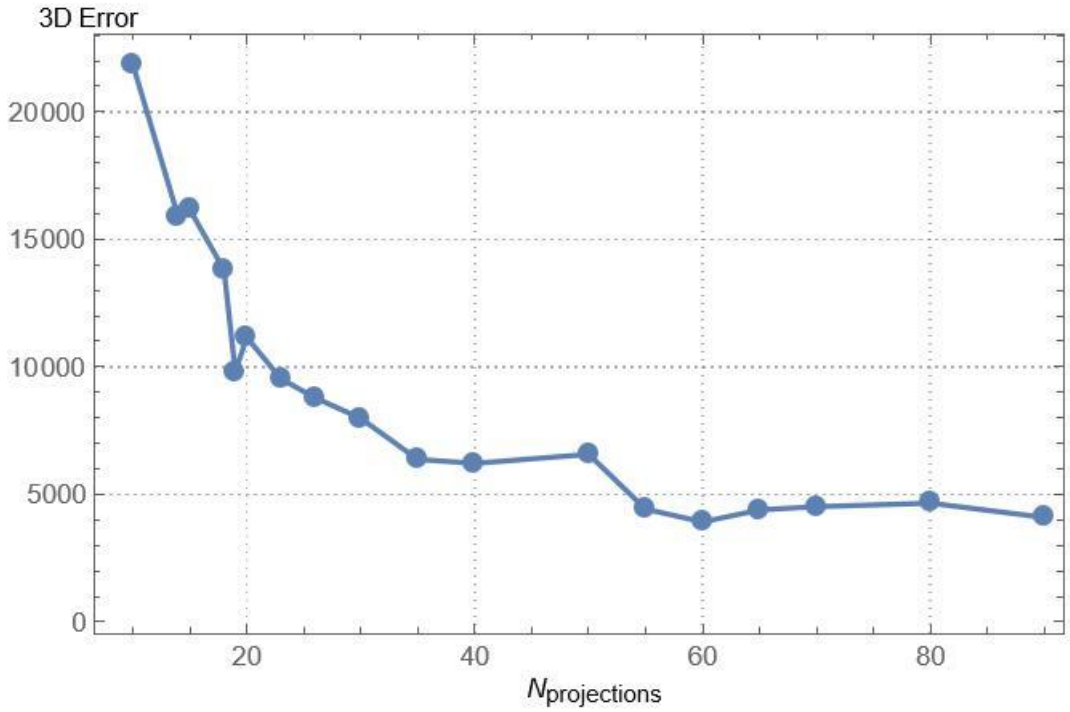

(a)

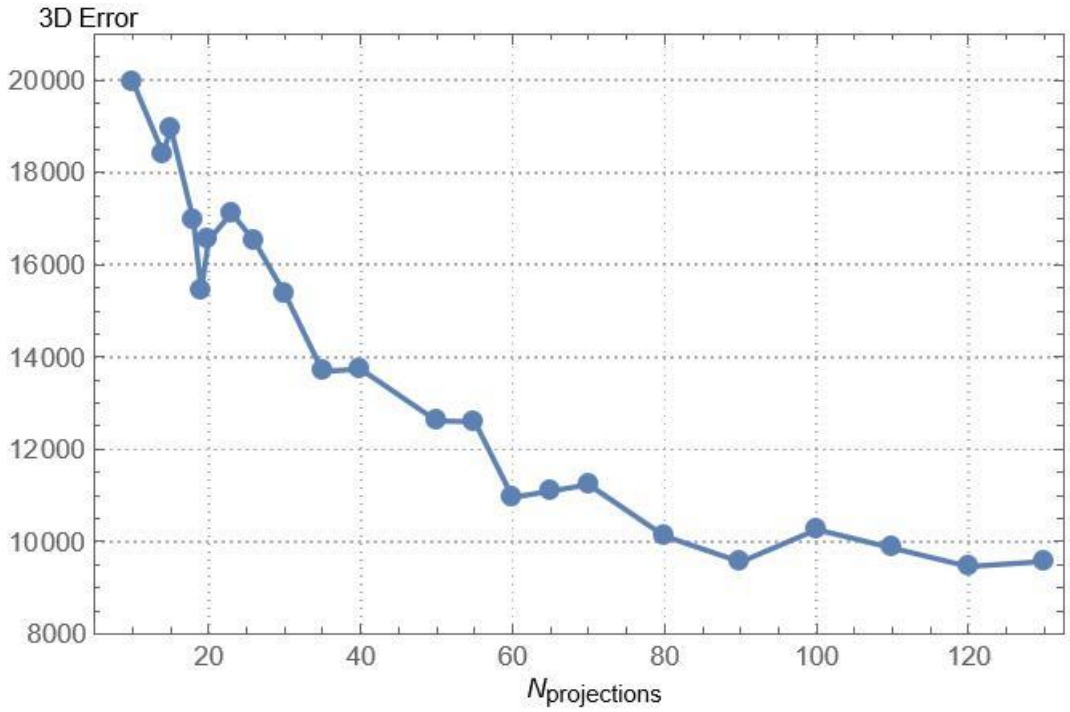

(b)

Figure 3.5.4 Plot of the 3D errors in relation to the projection numbers for (a) 1% noise level and (b) 5% noise level, for non-symmetric PAD.

The plot of the 3D errors for the noiseless case resembles the plot for the symmetric elliptical case, showing fluctuations across all projections and seeming to stabilize at an almost constant value at the later projections. The 3D errors decrease rapidly with the number of projections.

The plots for the noise cases both exhibit fluctuations that are particularly pronounced at the 5% noise level. Both plots display a rapid decrease in error. Additionally, similar to the symmetric case the 3D error values for the noiseless and 1% noise case are generally smaller than those for the 5% noise level.

4. Conclusions

The present work aimed to develop a computer program that employs the tomographic method to reconstruct 3D PADs produced from light-matter interactions. Specifically, these distributions were produced by a two-photon ionization of a Hydrogen atom by laser light with various polarizations. By simulating a VMI spectrometer the 3D PADs were projected onto a plane to generate 2D images. These projected images were analyzed both with and without the presence of noise to more accurately assess the program's performance under realistic conditions.

In the case of linear polarization tomography was compared to the POP method for reconstructing the 3D PAD from the projected images. Our findings indicate that applying an appropriate mask to the reconstructed images less than 20 projections are required for tomography to achieve the same accuracy as the POP method for noiseless data. By removing the mask, around 20 projections are needed to achieve the same accuracy as POP for both noiseless data and data with minimal noise level. However, as background noise increases more than 140 projections are required for tomography to match the accuracy of the POP method. This result, though, is unreliable due to the high sensitivity of tomography to elevated noise levels. This phenomenon is observed in all the following PADs generated at these noise levels, specifically, in both symmetric and non-symmetric distributions produced by elliptical polarization. A straightforward solution was to further bandlimit the filter used in the reconstruction process. This approach, though, can lead to blurry images with reduced detail.

Overall, our code successfully reconstructed the 3D PADs in all cases with the potential to surpass the existing Abel inversion method. Nonetheless, there is room for improvement. First, further investigation of tomography with noisy data is needed to assess its ability to produce accurate and stable results, particularly at higher noise levels. One possible approach is a more in-depth examination of the filtering process, using a specialized filtering function that better suppresses high noise signal. Another potential improvement is refining the masking process, where the concealment of the background noise precisely fits the outline of the reconstructed distribution, maximizing the data signal contribution. Second, to better address these challenges and achieve superior results, the utilization of modern and sophisticated data processing methods, such as artificial neural networks [45], is required. Lastly, since the tested images were simulations of experimental data, it is essential to validate our findings with real data to determine if the results hold in practice.

Although tomography has some setbacks, such as sensitivity to high noise levels, is established as a powerful method capable of accurately reconstructing 3D objects. In atomic physics tomography is especially valuable because it enables the retrieval of 3D distributions produced by

complex light-matter interactions, without limitations on the polarization of light, the symmetry of the distribution or the nature of the physical process. Therefore, developing this program was essential as it expands the range of physical phenomena that can be examined.

Appendix A: Derivation of 3D photoelectron momentum distributions from two-photon ionization out of an s-state.

The physical system consists of a gas of hydrogenic atoms interacting with a laser field of specified polarization in the presence of a uniform electric field. This interaction results in a three-dimensional flux of electrons ejected during photoionization which are then imaged by a position sensitive detector, revealing a particular spatial distribution. The 3D photoelectron angular distribution (PAD) is determined by considering a two-photon ionization of the atom, where the atom initially in the ground state ionizes to an unbound state via an intermediate virtual state, as illustrated in Figure A.1. The 3D PAD is calculated by employing a two-state model approximation of the ionization process along with first order time dependent perturbation theory, while ignoring the electron spin contribution. All equations are written in atomic units ($\hbar$=e=m_e=1).

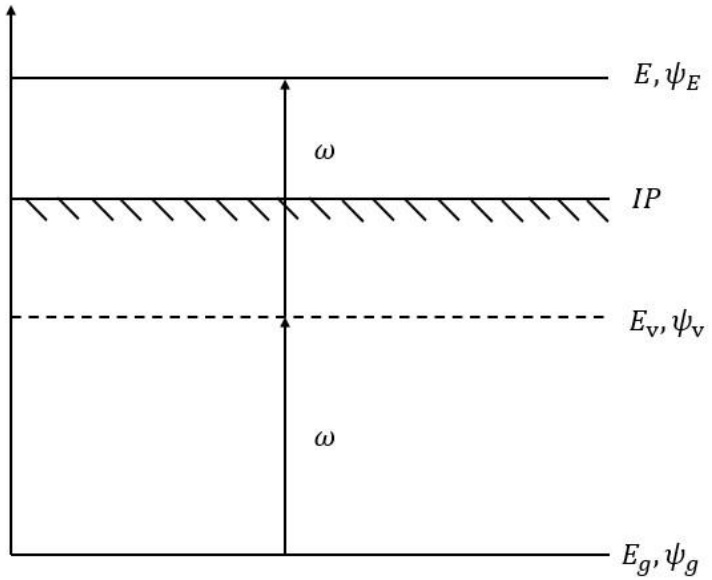

Figure A.1. The two-photon transition model, out of the ground state to a virtual state and from the virtual state to the final continuum state.

A1. Time Dependent Schrödinger Equation and "Schrödinger equation with a source": Spinless case

Consider either the Hydrogen atom or a single valence electron atom outside closed (sub)shells (as for example the Alkali atoms). In either case the interaction of the valence electron with the ionic core may be described by a spherically symmetric potential $U(r)$. Then, the Hamiltonian writes,

$$H(\mathbf{r}) = -\frac{1}{2}\nabla^2 + U(r). \tag{A1}$$

Let us now examine the simpler case of single-photon ionization out of an initial state ψ_i of energy E_i to a continuum state ψ_E of energy E, both solutions of the Schrödinger equation $H(\mathbf{r})\psi = E\psi$. The outgoing flux of photoelectrons is described by the electron Probability Current Density. The latter depends on an outgoing wave ψ_{out} (which is complex and should not be confused with the real wavefunction ψ_E, but they both refer to the same energy E). The relevant differential equation satisfied by ψ_{out} is derived from the Time Dependent Schrodinger Equation (TDSE):

$$i\frac{\partial \Psi}{\partial t} = \mathcal{H}\Psi \tag{A2}$$

where the total Hamiltonian $\mathcal{H}$

$$\mathcal{H} = H(\mathbf{r}) + V(\mathbf{r}, t) \tag{A3}$$

consists of the time independent part of Eq. (A1), and the time dependent part, which describes the dipole light-matter interaction term [46],

$$\begin{aligned} V(\mathbf{r}, t) &= -\mathbf{d}\cdot\mathbf{E} = \\ &= \boldsymbol{\varepsilon}\cdot\mathbf{r}\, E_0 \mathcal{F}(t)(\boldsymbol{e^{i\omega t}} + \boldsymbol{e^{-i\omega t}}) \end{aligned} \tag{A4}$$

where $\mathbf{d}$ is the dipole moment operator, $\mathbf{E}$ the electric filed of the laser, $\boldsymbol{\varepsilon}$ the light polarization vector, E_0 the real field amplitude, $\mathcal{F}(t)$ the time envelope of the pulse and ω the laser field circular frequency. We now adopt a two-state model for the atom [47,48,49] where the wavefunction Ψ of the system is decomposed in two terms, one referring to the initial state ψ_i and one to the final outgoing wave state ψ_{out}, i.e.

$$\Psi(\mathbf{r}, \mathrm{t}) = c_i(t)\psi_i(\mathbf{r})e^{-E_i t} + c_{out}(t)\psi_{out}(\mathbf{r})e^{-iEt} \tag{A5}$$

As mentioned above, we assume that ψ_i is an eigenstate of the time-independent Hamiltonian H,

$$H(\mathbf{r})\psi_i = E_i\psi_i \tag{A6}$$

and the resonant excitation implies

$$\omega = E - E_i. \tag{A7}$$

Inserting Equations A1 and A3-A7 into Equation A2, using first order time dependent perturbation theory [50] to obtain approximate expressions for the coefficients c_i (≈ 1) and c_{out} ($\approx E_0 {c_{out}}^{(1)}(t)$), and keeping terms up to linear with respect to E_0 we get

$$\left(i\frac{\partial {c_{out}}^{(1)}}{\partial t} + {c_{out}}^{(1)}E\right)\psi_{out} = {c_{out}}^{(1)}H\psi_{out} + \boldsymbol{\varepsilon}\cdot\mathbf{r}\,\mathcal{F}(t)(e^{2i\omega t} + 1)\psi_i \tag{A8}$$

Introducing the "rotating wave approximation" [49] into Equation A17, the term $e^{2i\omega t}$ is dropped because it rapidly oscillates with time and its net effect is negligible. Then we arrive at,

$$\left(-i\frac{\partial}{\partial t}+H(\mathbf{r})-E\right)c_{out}{}^{(1)}\psi_{out}=-\boldsymbol{\varepsilon}\cdot\mathbf{r}\,\mathcal{F}(t)\psi_i \tag{A9}$$

If we further assume the Electric Field has constant amplitude, i.e. $\mathcal{F}(t)=1$, $c_{out}{}^{(1)}$ becomes independent of time, its time derivative is zero, and the coefficient can be absorbed into the outgoing wavefunction ψ_{out}. Therefore, Equation A9 can be written as,

$$(H(\mathbf{r})-E)\psi_{out}=-\boldsymbol{\varepsilon}\cdot\mathbf{r}\ \psi_i \tag{A10}$$

which is known as "Schrödinger equation with a source" [49]. For solving this equation, we express ψ_{out} in the form,

$$\psi_{out}=r^{-1}\sum_{l\prime,m\prime}P^{out}_{l\prime,m\prime}Y^{l\prime}_{m\prime}. \tag{A11}$$

where Y^l_m denotes spherical harmonics and the functions $P^{out}_{l\prime,m\prime}$ need to be determined. It turns out [51] that in the $r\to\infty$ lmit these functions are written as,

$$\underset{r\to\infty}{P^{out}_{l,m}}(r)=-\frac{2}{C_r}d_{lm}\frac{1}{[k(r)]^{1/2}}e^{i(\theta_l(r)+\phi_l)} \tag{A12}$$

with d_{lm} the dipole transition matrix elements connecting states $\psi_i=r^{-1}P_iY^{l_i}_{m_i}$ and $\psi_E=r^{-1}P_{El}Y^l_m$,

$$d_{lm}=\int r^{-2}P_{El}Y^l_m\ \boldsymbol{\varepsilon}\cdot\ \mathbf{r}\,P_iY^{l_i}_{m_i}\,dV, \tag{A13}$$

and where the continuum wavefunction P_E at large distances and in it semiclassical (WKB) form is written as [51],

$$P_{El}(r)=\frac{C_r}{[k(r)]^{1/2}}\sin[\theta_l(r)+\phi_l] \tag{A20}$$

with C_r a normalization constant and $k(r)$ the wavenumber function,

$$k(r)=\left[2\left(E-U(r)-\frac{(l+1/2)^2}{r^2}\right)\right]^{1/2} \tag{A15}$$

Finally, the function $\theta_l(r)$ is given by,

$$\theta_l(r)\ =\int_{r_o}^{r}k(r\prime)dr\prime \tag{A16}$$

and ϕ_l is a constant phase depending on r_o. It is important to note that the matrix elements (A44) incorporate dipole transition selection rules.

A2. Electron Probability Current Density

Once the outgoing wave ψ_{out} is known the probability current density can be calculated from the definition [44],

$$\mathbf{J} = -\frac{2\pi\alpha\omega}{2i}[\psi_{out}\nabla(\psi_{out})^* - (\psi_{out})^*\nabla\psi_{out}] \tag{A17}$$

Since ionization proceeds solely via the r-coordinate, we need the projection of **J** in the r-direction,

$$J_r = \mathbf{J}\cdot\mathbf{e_r} = -\frac{2\pi\alpha\omega}{2i}\left[\psi_{out}\frac{\partial(\psi_{out})^*}{\partial r} - (\psi_{out})^*\frac{\partial\psi_{out}}{\partial r}\right] \tag{A18}$$

where $\mathbf{e_r}$ is the relevant unit vector. Inserting Equations A11-A16 in Equation A18, we obtain,

$$J_{r\,r\to\infty} = \frac{4\pi\alpha\omega}{r^2 C_r{}^2}\left|\sum_{l,m} d_{lm}e^{i(\theta_l(r)+\phi_l)}Y_{l,m}\right|^2 \tag{A21}$$

which encompasses the angular distribution of the 3D photoelectron flux. Finally, by integrating over the whole sphere we get the total cross section σ_{tot},

$$\int J_r dS = 4\pi^2\alpha\omega\sum_{l,m}|d_{lm}|^2 = \sigma_{tot} \tag{A22}$$

where $dS = r^2 sin\theta\, d\theta\, d\varphi = r^2 d\Omega$ is the sphere's surface element.

A3 Two-photon ionization PADs with arbitrary light polarization

Two-photon ionization may be perturbatively described as a single-photon ionization process out of a virtual initial state $\psi_i = \psi_v$ entering in the Schrödinger equation with a source, Eq. (10). In turn, the virtual state obeys itself the following Dalgarno-Lewis equation [52],53],

$$(H(\mathbf{r}) - E_v)\psi_v = -\boldsymbol{\varepsilon}\cdot\mathbf{r}\,\psi_g \tag{A21}$$

with $\psi_g = r^{-1}P_g Y_0^0$ denoting the ground (truly initial) s-state (of Hydrogen or an Alkali atom) of energy E_g. $E_v = \left(E + E_g\right)/2$ is the virtual state energy. To find all possible solutions of Eq. 21, we expand the virtual state as,

$$\psi_v = r^{-1}\sum_{l',m'} P_{v,l',m'}Y_{m'}^{l'}. \tag{A22}$$

The harmonics $Y_{m'}^{l'}$ are referenced to the quantization axis z that here we choose to be the propagation axis of the ionizing laser beam (perpendicular to the VMI spectrometer axis and parallel to the charged particle detector). We allow for arbitrary light polarization by writing the dipole operator as,

$$\boldsymbol{\varepsilon}\cdot\mathbf{r} = fx + \eta e^{i\delta}y. \tag{A23}$$

Thus, the dipole operator is decomposed into two linear polarization terms of amplitudes f and η along the x- and y-axes, respectively, and a relative phase δ between them. In practice the amplitude

f is set equal to either 0 or 1, while the amplitude η can take any real value. In terms of the spherical harmonics the dipole operator writes,

$$\boldsymbol{\varepsilon}\cdot\mathbf{r} = r\sqrt{\frac{2\pi}{3}}\left[f\,(Y_{-1}^{1} - Y_{1}^{1}) + \eta e^{i\delta}(Y_{-1}^{1} + Y_{1}^{1})\right] \tag{A24}$$

and it evidently leads to the selection rules

$$\Delta l = \pm 1 \text{ and } \Delta m = \pm 1 \tag{A25}$$

for each transition, $\psi_g \to \psi_v$ and $\psi_v \to \psi_E$. Indeed, the virtual state is finally written as,

$$\psi_v = r^{-1}\tilde{P}_{v,1}\frac{1}{6^{1/2}}\left[\left(f + \eta e^{i\delta}\right)Y_1^{-1} - \left(f - \eta e^{i\delta}\right)Y_1^{1}\right] \tag{A26}$$

where the radial part $\tilde{P}_{v,1}$ exhibits no angular dependence, and where angular factors are explicitly calculated.

We now need to compute the matrix elements $d_{lm} = \langle\psi_E|\boldsymbol{\varepsilon}\cdot\mathbf{r}|\psi_v\rangle$ entering the current probability density Eq. A19. After some manipulations we finally arrive at the following PAD expression:

$$\begin{aligned} J_{r\,r\to\infty} \propto \frac{1}{r^2}\Bigg| & \left(f^2 + \eta^2 e^{2i\delta}\right)Y_0^0 \\ & + \frac{\Lambda e^{i\Delta\theta_{20}^{*}}}{5^{1/2}}\Bigg\{-\left(f^2 + \eta^2 e^{2i\delta}\right)Y_2^0 \\ & + \left(\frac{3}{2}\right)^{1/2}\left[\left(f^2 - \eta^2 e^{2i\delta}\right)(Y_2^2 + Y_2^{-2}) - 2f\eta i e^{i\delta}(Y_2^2 + Y_2^{-2})\right]\Bigg\}\Bigg|^2 \end{aligned} \tag{A27}$$

where,

$$\Lambda \equiv \frac{\int dr\; r\; P_{E2}\tilde{P}_{v,1}}{\int dr\; r\; P_{E0}\tilde{P}_{v,1}} \tag{A28}$$

is the relative strength of the radial integrals connecting the radial wavefunction $\tilde{P}_{v,1}$ of the virtual state and the l=2 (P_{E2}) and l=0 (P_{E0}) continuum wavefunctions, while,

$$\Delta\theta_{20}^{*} = \theta_2 - \theta_0 + \phi_2 - \phi_0. \tag{A29}$$

The excitation and ionization pathways described by Eq. A25 are shown schematically in Figure A.2. Parameters Λ and $\Delta\theta_{20}^{*}$ depend on the specific atom that a calculation refers and need to be computed separately. As a propensity rule Λ>1 [54], while there are cases, depending on the photon energy ω, where either $\Lambda \approx 0$ or $\Lambda \gg 1$ [54,55]. In this latter case that we are about to use more frequently in the present work, the spherically symmetric term proportional to Y_0^0 can be neglected and the probability current density simplifies to the below expression, which is independent of both Λ and $\Delta\theta_{20}^{*}$.

$$J_{r_{\Lambda\gg}} \propto \frac{1}{r^2}\left|-\left(f^2+\eta^2 e^{2i\delta}\right)Y_2^0 + \left(\frac{3}{2}\right)^{1/2}\left[\left(f^2-\eta^2 e^{2i\delta}\right)\left(Y_2^2+Y_2^{-2}\right)-2f\eta i e^{i\delta}\left(Y_2^2+Y_2^{-2}\right)\right]\right|^2 \quad \text{(A30)}$$

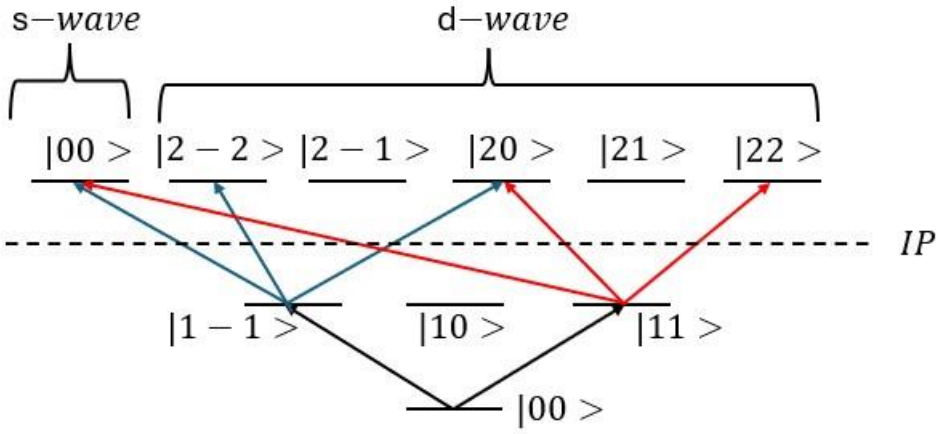

Figure A.2. Transition pathways of a two-photon excitation and ionization of a Hydrogen atom out of its s-ground state via a virtual state obeying the selection rules $\Delta l = 1\ and\ \Delta m = \pm 1$. The virtual state is a linear combination of $|lm>= |1-1>$ and $|11>$ states. The final state can be expressed as a sum of an s-wave and a d-wave. The s-wave is represented by the $|00>$ state, while the d-wave is represented by the $|2-2>$, $|20>$ and $|22>$ states.

The total cross section σ_{tot} is equal to the sum of the partial cross sections σ_l from the s and d state contributions. This is expressed as

$$\sigma_{tot} = \sigma_s + \sigma_d \quad \text{(A31)}$$

However, based on Equation A20 for linear polarization, the total cross section σ_{tot} is given by,

$$\sigma_{tot} = 4\pi^2\alpha\omega\left(\frac{\left(\int dr\ r\ P_{E0}\tilde{P}_{v,1}\right)^2}{9} + \frac{\left(\int dr\ r\ P_{E2}\tilde{P}_{v,1}\right)^2}{45}\right) \quad \text{(A32)}$$

Comparing the Equations A31 and A32 we get, $\sigma_s = 4\pi^2\alpha\omega\frac{\left(\int dr\ r\ P_{E0}\tilde{P}_{v,1}\right)^2}{9}$ and $\sigma_d = 4\pi^2\alpha\omega\frac{\left(\int dr\ r\ P_{E2}\tilde{P}_{v,1}\right)^2}{45}$.

For a two-photon ionization process below the threshold, a Hydrogen atom at energy of $\omega \approx 9eV$ exhibits an anti-resonance for the $l = 0$ state [54]. Consequently, the partial cross sections are $\sigma_s \approx 10^{-3}$ and $\sigma_d \approx 10^2$,respectively, with units of $10^{-52}\ cm^4 s$

From the ratio of the partial cross sections, we get an order of magnitude for the $\Lambda-$parameter (Equation A28), $\Lambda \approx 400$, which satisfies the $\Lambda \gg 1$ condition and therefore the use of Equation A30

at this energy level is valid. The $\Lambda-$parameter depends solely on integrals of radial wavefunctions, therefore it the calculated value applies to all polarizations.

Appendix B: Polar Onion Peeling

In experiments using linearly polarized light, the produced momentum distribution is cylindrically symmetric about the polarization axis. The Abel transform exploits this symmetry and allows the extraction of the 3D distribution from one single measurement of its projection on the detector [10-12].

Suppose a momentum distribution $f(z,r)$ in cylindrical coordinates with cylindrical symmetry about the *z*-axis. The lab frame of reference is (x,y,z) and in relation to this the linearly polarized light is along the *z*-axis while the projection of the distribution is carried out along the *y*-axis. The image on the detector is therefore,

$$P(x,z) = \int_{-\infty}^{+\infty} f(z,r)d\,y = 2\int_{|z|}^{\infty} f(z,r)\frac{r\,dr}{\sqrt{r^2-x^2}} \tag{B23}$$

using a simple change of variables with $r=\sqrt{x^2+y^2}$.This is the Abel transform [56] of the $f(z,r)$ function. The quantity of interest in Equation B1 is the 3D distribution $f(z,r)$ which can be obtained by evaluating the inverse Abel transform [56]

$$f(z,r) = -\frac{1}{\pi}\int_{r}^{\infty}\frac{dP(x,z)}{d\,x}\frac{d\,x}{\sqrt{x^2-r^2}} \tag{B24}$$

The direct numerical estimation of this equation is generally avoided primarily due to the singularity and sensitivity to noise in realistic data. A few methods have been proposed to circumvent these challenges and accurately approximate the 3D distribution. One such method is the pBasex approach [57] which uses a set of basis functions that are analytical solution to Equation B1. The data are then fitted to the basis set using a least squares method. Another method is the Vrakking approach [10], which is an iterative process to determine the solution to Equation B2. Both methods yield accurate results and handle noisy data effectively by accumulating the noise at the center of the reconstructed image. Comparable to these methods is the Polar Onion Peeling (POP) [22,58] method, an improvement to the Onion Peeling method [8], which will be presented below.

B1. Basic idea

The basic premise of the Onion Peeling method is that each point on the detector has a contribution from the φ-dependence of the original 3D PAD, as shown in Figure B1. Using Cartesian coordinates this dependence can be calculated and removed by starting from the outermost pixel on each row of the detector image and moving along the *x*-axis towards the central *z*-axis. This method

is fast and particularly effective when the kinetic energy of the photoproducts is much less than the energy gained from the electric field in the detection [8]. However, the main drawback is noise accumulation to the central *z*-axis. The solution of this problem is onion peeling in polar coordinates [22,58] in which the error is reduced at large radii and accumulated to a spot at the center of the inverted image. The basics of the method will be presented below.

Suppose a 3D radial distribution $F(r,\theta,\varphi)$ that has cylindrical symmetry around the *z*-axis, as shown in Figure B.1. The z-axis corresponds to the polarization vector which is linear for an inverse Abel transform to apply. In a VMI spectrometer the 3D momentum distribution is projected along an axis (*y*-axis) onto the 2D plane parallel to the (x, z) plane,

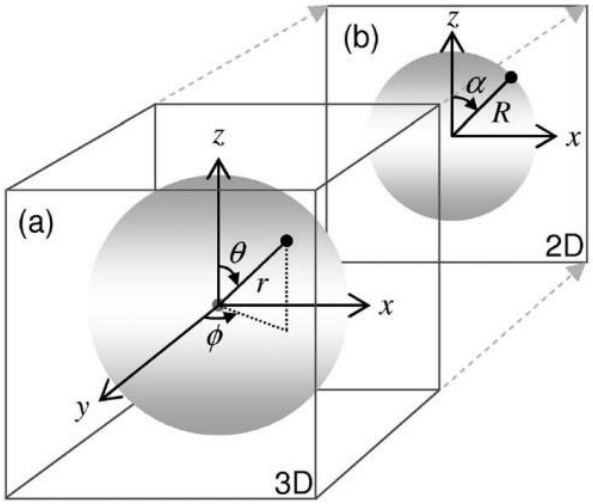

Figure B.1. 3D distribution with cylindrical symmetry about the laser polarization axis and its projection on the detector plane, original image taken from [22]

producing the measured 2D distribution $G(R,a)$. This distribution is also in polar coordinates where R is the radius and α the angle in relation to the z-axis of the detector.

If we consider $F(r,\theta,\varphi)$ a cylindrically symmetric distribution of constant $r = R_0$, then due to its φ-dependence the measured distribution $G(R,a)$ will have signal at radii $R < R_0$. This signal can be calculated and subtracted away from $G(R,a)$ for all $R < R_0$ resulting in a distribution that is equivalent to a slice though the original distribution: $F(r,\theta,\varphi = 0)$. The full distribution can be recovered by rotation of $F(r,\theta,\varphi = 0)$. about the polarization axis.

This process can be generalized for a PAD with varying r. In this case, each r of the PAD corresponds to a projection $g(r;R,a)$ that has signal due to the φ-dependence at all radii $R \leq r$. Consequently, the measured projection, $G(R,a)$, can be expressed as the sum of the individual projections, $g(r;R,a)$, for all r values of the PAD,

$$G(R,a) = \int_0^{r_{max}} g(r;R,a)dr \tag{B3}$$

where, as mentioned, $R \leq r$ and the semicolon in $g(r;R,a)$ indicates that the projections correspond to specific radii r. The POP method exploits the principle described by Equation B3, which indicates that for each radial distance r, the slice of the 3D PAD,$F(r,\theta,\varphi=0)$, corresponds to a circle of radius $R=r$ in the projected distribution. Beginning with the outermost radius of the PAD $r=r_{max}$ its projection $g(r=r_{max};R,a)$ is subtracted for all radii $R<r_{max}$.leaving only the circle with $R=r_{max}$. This process removes the φ-dependence from the 2D measured distribution for all $R<r_{max}$ at this specific r_{max}.

By repeating this process for incrementally decreasing steps of dr down to $r=0$,the projection $g(r;R,a)$ is subtracted from $G(R,a)$at each radius r. This effectively "peels away" the φ-dependence from the projection at each r, resulting in a slice though the polarization plane of the 3D PAD.

This process was described using polar coordinates [22] for both the 3D PAD and the 2D measured projection but can also be employed in Cartesian coordinates [58].

B2. Computation

The extraction of the deconvoluted image from the 2D measured projection is achieved by determining the 2D projection $g(r;R,a)$ at each radius r. One approach to calculation this is by simulating the 3D PAD at each radial increment [58]. However, this approach is computationally demanding. Therefore, an alternative faster yet equivalent method is presented in which basis functions are used to fit the experimental 2D projections [22].

As mentioned in section B1 the outermost circle of the 2D projection contains no φ-dependence, thus at $r=R$ it can be expressed as

$$g(r;R,a) = h(r,\theta) \tag{B4}$$

By substituting $r=r_{max}$, $h(r_{max},\theta)$can be fitted to the angular distribution [46]:

$$I(\theta) = N(r)\sum_n \beta_n(r)\, P_n[cos(\theta)] \tag{B5}$$

where $P_n[cos(\theta)]$ is the n^{th} order Legendre polynomial, $N(r)$ is an intensity factor and $\beta_n(r)$ the anisotropy parameters. The fitting is performed by standard linear least-squares method. The integer n is even [59] and depends on the physics, where in our case of-a two-photon process an order of n=2 is sufficient [22].

The fit provides the $N(r)$ and $\beta_n(r)$ from which the distribution $g_{fit}(r_{max}; R, a)$ may be calculated. This distribution is then subtracted from the image $G(R, a)$ for all $R \leq r_{max}$:

$$G_s(R, a) = G(R, a) - g_{fit}(r; R, a) \quad \text{(B6)}$$

$G_s(R, a)$ is a modified detector image containing no φ-dependence from the r_{max} radius projection of the 3D distribution. This process is repeated for $r = r_{max} - dr$ down to $r = 0$. At the end, $G_s(R, a)$ represents the 2D slice $F(r, \theta, \varphi = 0)$ of the 3D PAD, which can also be provided by retaining $h(r, \theta)$ in Equation B4 at each increment.

The distribution $g_{fit}(r; R, a)$ is generated using basis functions. These basis functions are radial distribution functions $b_r(R)$ obtained by angular integration of isotropic images at all possible radii r. Importantly, the basis set is computed only once and then utilized throughout the reconstruction process. The overall size of the basis set is determined by the number of pixels on the CCD.

An idealized isotropic projection image $g_{ideal}(r; R, a)$ is constructed from the basis function $b_r(R)$ using:

$$g_{ideal}(r; R, a) = \rho(r, R)\, b_r(R) \quad \text{(B7)}$$

where the factor $\rho(r, R)$ indicates the number of pixels with their associated intensities. The image $g_{fit}(r; R, a)$ is then generated through:

$$g_{fit}(r; R, a) = g_{ideal}(r; R, a) N(r) \sum_n \beta_n(r)\, P_n[\tfrac{R}{r}\cos(a)] \quad \text{(B8)}$$

The factors $N(r)$ and $\beta_n(r)$ were obtained from the fitting of the outer ring $h(r, \theta)$ at each r to Equation B5. The factor R/r accounts for the transformation between the coordinate system (r, θ, φ) and the (R, a) ,as shown in Figure B1.

Bibliography

1 J Radon. On the determination of functions from their integral values along certain manifolds. IEEE Trans. Med. Imag, 5(4):170, 1986.

2] A C Kak and M Slaney. Principles of Computerized Tomographic Imaging. Society for Ind. Appl. Math, 200.

3 Mahesh M. The Essential Physics of Medical Imaging, Third Edition. Med Phys. 2013 Jul;40(7)

4 A. Einstein, Annalen der Physik (Jan. 1905).

5 M. Eklund, H. Hultgren, I. Kiyan, H. Helm, and D. Hanstorp. Phys. Rev. A **102**, 023114 ,19 August 2020.

6. H. Helm, N. Bjerre, M. J. Dyer, D. L. Huestis, and M. Saeed, Phys. Rev. Lett. 70, 3221 (1993).

7 A. T. J. B. Eppink and D. H. Parker, Rev. Sci. Instrum. 68, 3477 (1997).

8 C. Bordas, F. Paulig, H. Helm, July 1996.The Review of scientific instruments.

9 C Smeenk et al 2009 J. Phys. B: At. Mol. Opt. Phys.**42**185402.

10 M. Vrakking, Rev. Sci. Instrum. 72, 4084 (2001).

11 V. Dribinski, A. Ossadtchi, V. Mandelshtam, H. Reisler, Rev. Sci. Instrum. 73, 2634 (2002)

12 G. Garcia, L. Nahon, I. Powis, Rev. Sci. Instrum. 75, 4989 (2004).

13 Smith L, Keefer D and Sudharsanan S 1988 J. Quantum. Spectrosc. Radiat. Trans. 39 367–73.

14 S. Kim and A. K. Khambampati, "Mathematical concepts for image reconstruction in tomography, in Industrial Tomography", edited by M. Wang, Woodhead Publishing Series in Electronic and Optical Materials (Woodhead Publishing, Sawston, UK, 2015), pp. 305–346.

15 R.M. L. Wagner, Atoms and Molecules in Strong Laser Fields, Hamburg 2022.

16 M. Wollenhaupt, M. Krug, J. Köhler, T. Bayer, C. Sarpe-Tudoran, T. Baumert, Appl Phys B (2009) 95: 647–651.

17 J. Maurer, Tomographic reconstruction of 3-dimensional photoelectron momentum distributions using aligned molecules, PHD thesis,2012.

18 R. C. Gonzalez, R. E. Woods, "Digital Image Processing", Pearson Education,2018.

19 M. Wollenhaupt, C. Lux, M. Krug, and T. Baumert, ChemPhysChem 14, 1341 (2013).

20] P. Hockett, M. Staniforth, and K. L. Reid, Mol. Phys. 108, 1045 (2010).

21 P. Hockett, C. Lux, M. Wollenhaupt, and T. Baumert, Phys. Rev. A 92, 013412 (2015).

22 G. M. Roberts; J. L. Nixon; J. Lecointre; E. Wrede; J. R. R. Verlet, *Rev. Sci. Instrum.* 80, 053104 (2009).

23 Beatty, Jen, "The Radon Transform and the Mathematics of Medical Imaging" (2012). Honors Theses. Paper 646.

24 C. L. Epstein, "Introduction to mathematics of Medical Imaging", Society for Industrial and Applied Mathematics; 2nd edition (November 29, 2007).

25 G. B. Arfken., H. J. Weber. (2000), *Mathematical Methods for Physicists* (5^{th} ed.), Boston, Massachusetts.

26 A. C. Kak, "Computerized tomography with x-ray emission and ultrasound sources," Proc. IEEE, vol. 67, pp. 1245-1272, 1979.
27 A. Rosenfeld and A. C. Kak, Digital Picture Processing, 2nd ed. New York, NY: Academic Press, 1982.
28 G. Arfken, (1985), *"Mathematical Methods for Physicists"* (3rd ed.), Academic Press.
29 L. A. Shepp and B. F. Logan, IEEE Trans. Nucl. Sci., vol. NS-21, pp. 21-43, 1974.
30 A. C. Kak, "Tomographic imaging with diffracting and non-diffracting sources," in Array Signal Processing, S. Haykin, Ed. Englewood Cliffs, NJ: Prentice-Hall, 1985.
31 S. X. Pan and A. C. Kak, "A computational study of reconstruction algorithms for diffraction tomography: Interpolation vs. filtered backpropagation," IEEE Trans. Acoust. Speech Signal Processing, vol. ASSP-31, pp. 1262-1275, Oct. 1983.
32 H. Stark, J. W. Woods, I. Paul, and R. Hingorani, "Direct Fourier reconstruction in computer tomography," IEEE Trans. Acoust. Speech Signal Processing, vol. ASSP-29, pp. 237-244, 1981.
33 G.N. Ramachandran, A. V. Lakshminarayanan [1971]. "Three Dimensional Reconstructions from Radiographs and Electron Micrographs: Application of Convolution Instead of Fourier Transforms,", Proc. Nat. Acad. Sci., vol. 68, pp. 2236–2240, 1971.
34 R. W. Hamming, Digital Filters. Englewood Cliffs, NJ: Prentice-Hall, 1977.
35 L. Tan, "Digital Signal Processing Fundamentals and Applications", 2008, Elsevier Inc.
36 S. A. Qureshi1, S. M. Mirza, M. Arif, Science International 18(3):181-186, September 2020.
37 C. R. Crawford and A. C. Kak, "Aliasing artifacts in computerized tomography," Appl. Opt., vol. 18, pp. 3704-3711, 1979.
38 A. Rosenfeld and A. C. Kak, Digital Picture Processing, 2nd ed. New York, NY: Academic Press, 1982.
39 A. C. Kak, "Image reconstruction from projections," in Digital Image Processing Techniques, M. P. Ekstrom, Ed. New York, NY: Academic Press, 1984.
40 C. Sparling, D. Rajak, V. Blanchet, Y. Mairesse, D. Townsend, Rev. Sci. Instrum.95, 053301 (2024).
41 P. Kalaitzis, S. Danakas, C. Bordas, and S. Cohen, Physical Review A 108, 013106 (2023).
42 C. Sparling and D. Townsend, J. Chem. Phys. 157 114201 (2022).
43 D.J. Griffiths, "Introduction to Electrodynamics",4th Edition, Cambridge University Press, 2017.
44 H. Friedrich, "Theoretical Atomic Physics", 4th edition: Springer International Publishing AG 2017.
45 C. Sparling, A. Ruget, N. Kotsina, J. Leach, and D. Townsend, ChemPhysChem, Volume 22, Issue 1, 2021, pages 76-82.
46 F. Jensen. "Introduction to computational chemistry" (2nd ed.). Chichester, England: John Wiley & Sons, (2007).
47 P. Kalaitzis, D. Spasopoulos, and S. Cohen, Phys. Rev. A 100, 043409 (2019).
48 T. Topçu and F. Robicheaux, J. Phys. B 40, 1925 (2007).
49 H. Haken, H.C. Wolf, "The Physics of Atoms and Quanta, Introduction to Experiments and Theory",7th Edition, Springer-Verlag Berlin Heidelberg, 2005
50 L.D. Landau, L.M Lifshitz," Quantum Mechanics: Non-Relativistic Theory",3rd Edition, Pergamon Press.
51 S. Cohen, "Lecture Notes in Atomic Physics", Ioannina 2004.

52 H.A. Mavromatis, American Journal of Physics 59, 738 (1991).

53 A. Dalgarno and J. T. Lewis, Proc. R. Soc. London, Ser. A 233, 70 (1955).

54 A. Mihelič and M. Horvat, Phys. Rev. A**103**, 043108 (2021).

55 E Karule 1978 J. Phys. B: Atom. Mol. Phys. 11 441.

56 Whitaker, "Imaging in Molecular Dynamics", Cambridge University Press, Cambridge, 2003.

57 G. A. Garcia, L. Nahon, I. Powis, *Rev. Sci. Instrum.*75, 4989–4996 (2004).

58 K. Zhao, T. Colvin, W. T. Hill, and G. Zhang, Rev. Sci. Instrum. 73, 3044 (2002).

59 K. L. Reid, Annu. Rev. Phys. Chem. 54, 397 (2003).